INTEGRATED PLASMONIC WAVEGUIDES AND DEVICES

A THESIS
Submitted to the Delhi Technological University
for the award of the degree of

DOCTOR OF PHILOSOPHY
in

APPLIED PHYSICS

By

VENUS DILLU

DEPARTMENT OF APPLIED PHYSICS
DELHI TECHNOLOGICAL UNIVERSITY
DELHI- 110042 (INDIA)
NOVEMBER 2015

INTEGRATED PLASMONIC WAVEGUIDES AND DEVICES

By

VENUS DILLU

DEPARTMENT OF APPLIED PHYSICS

Submitted

in fulfilment of the requirements of the degree of

DOCTOR OF PHILOSOPHY

to the

DELHI TECHNOLOGICAL UNIVERSITY

DELHI - 110042 (INDIA)

NOVEMBER 2015

Dedicated to the Lord my God, creator of heaven and earth, who in His mercies created me to be an instrument of serving mankind

To my husband Bhagirath whose love has made me feel special all the time

To my son John who makes me feel I am on a rainbow

To my parents whose love and affection has brought me thus far

To my parents-in-law for their immense support

DECLARATION

This is to certify that the thesis entitled "**Integrated Plasmonic Waveguides and Devices**", being submitted for the award of the degree of Doctor of Philosophy to the Delhi Technological University, India, embodies the original research work carried out by me under the guidance of Prof R K Sinha, Department of Applied Physics, Delhi Technological University, India. The results obtained in this thesis have not been submitted in part or full to any other University or Institute for the award of any degree or diploma.

Venus Dillu

(Venus Dillu)

Candidate

Place: Delhi

Date: 23/11/16

23/11/2016

Prof Ravindra Kumar Sinha
(Supervisor)
Director,
Central Scientific Instruments Organisation
Chandigarh, India
On lien from the regular post of
Professor, Applied Physics
Delhi Technological University, Delhi, India

DELHI TECHNOLOGICAL UNIVERSITY

CERTIFICATE

This is to certify that the Ph.D. thesis entitled **"Integrated plasmonic waveguides and devices"** submitted to the Delhi Technological University, Delhi for the award of Doctor of Philosophy is based on the original research work carried out by me under the supervision of Prof. Ravindra Kumar Sinha, Department of Applied Physics, Delhi Technological University, Delhi, India. It is further certified that the work embodied in this thesis has neither partially nor fully submitted to any other university or institution for the award of any degree or diploma.

Venus Dillu

(Enrolment No.: 2k09/PhD/AP/16)

This is to certify that the above statement made by the candidate is correct to the best of our knowledge.

23/11/2016

Prof Ravindra Kumar Sinha
(Supervisor)
Director,
Central Scientific Instruments Organisation
Chandigarh, India
On lien from the regular post of
Professor, Applied Physics
Delhi Technological University, Delhi, India

23.11.2016

Prof Suresh C. Sharma
Head of the Department,
Applied Physics
Delhi Technological University
Delhi, India

Acknowledgements

It is matter of great privilege for me to have this blessed opportunity to express my sincere appreciation and deepest gratitude to everyone who have contributed and supported my PhD work.

First and foremost, I would like to express my greatest gratitude to my supervisor Prof. R. K. Sinha for his proficient guidance, ceaseless mentoring and continued encouragement for the fulfilment of this research work. With great pleasure I express my heartfelt gratitude for his advice, fruitful discussions, numerous insightful suggestions, patient listening, constructive criticisms and constant support throughout the period of my research. I could not have imagined having a better advisor and mentor for my PhD study.

Besides my advisor, I would like to thank Dr R K Bhattacharyya for his guidance and suggestions. I would also take this opportunity to thank Dr Yogita Kalra for insightful academic discussions. I am grateful to James Sir for making available all laboratory facilities throughout the PhD work.

I gratefully acknowledge the initiatives and support towards establishment of TIFAC Centre of Relevance and Excellence in Fiber Optics and Optical Communication at Delhi Technological University, Delhi through "Mission REACH" program of Technology Vision-2020, Government of India.

I would like to thank SPIE (International Society of Optics and Photonics) and OSA (Optical Society of America) for supporting and recognition of my research work.

I am grateful to my PhD colleagues and friends at Delhi Technological University for their continual support and encouragement throughout the PhD work. I am specially thankful to Dr Shruti for her friendship, encouragement and sharing commendable knowledge and insight in the subject of this research work. I am also thankful to Neelam Maikhuri, Ayushi Barthwal, Lucky Krishnia and Pooja Arora for their friendship, well-wishes and help extended time to time. I am

also greatly thankful to Preeti Rani, Kamal Kishor, Reena Dayal, Rachna Sharma, Thansingh Saini and Nishant for being wonderful research colleagues with ever-helping nature in academic and personal fronts. I have also been greatly enriched by meaningful academic discussions with Dr Triranjita Srivastava for which I am highly thankful.

I am greatly indebted to constant prayers, encouragement and emotional support of all my family members. I would specially like to thank my husband, Bhagirath Kumar Lader, for always being on my side throughout the journey of my PhD research work. I am also greatly thankful to my parents who believed in my abilities and always encouraged me to achieve excellence in life while never compromising on godly standards that they set before me. I am grateful to my parents-in-law for their blessings, encouragement and immense support during my PhD work. I am also thankful to my sister Rebecca Dillu for her words of cheer, prayers and well-wishes. I am also thankful to my brother-in-law Shivnath Lader and sister-in-law Soniya for their thoughtful well-wishes. I also feel greatly blessed to thank Lord Almighty for my son John Bhagirath Lader who brought joy and cheer as I worked through the final sections of my PhD work.

I thank all those whose names are not explicitly mentioned but who helped and supported me in this research work.

Finally, I would like to thank Lord Almighty, the Creator of heavens and earth, Giver of life and light, who is ultimate source of all knowledge and wisdom, and who empowered great minds before me to discover scientific facts and phenomena on which my work is based. To quote Sir Issac Newton, "If I have seen further than others, it is by standing on the shoulders of giants."

Date: (**Venus Dillu)**

Place: Delhi

Abstract

In this thesis metal nanoparticles of different shapes and sizes have been used to manipulate the properties of different plasmonic devices with enhanced transmission and high performance. Array of metal nanoparticles embedded in dielectrics exhibit plasmonic band gap that allows plasmon propagation with larger propagation length and low losses. We consider silver metal nanorods embedded on silicon on insulator (SOI) substrate for devising ultra-compact plasmonic waveguides like straight waveguide, y-splitter and bend design. Proposed waveguide exhibit low loss propagation, larger propagation length and strong confinement of the traversing plasmonic mode. These components can be used for high density plasmonic circuitry.

Low loss performance of such waveguides is further used to design highly sensitive plasmonic sensor used in sorting and classification of cancer cells. Plasmonic Mach-Zehnder interferometer (PMZI) is proposed for refractive index sensing assessed in terms of wavelength and phase shift. Proposed PMZI comprises of array of silver nanorods embedded upright into silicon on insulator thus exhibiting surface plasmon polariton band gap (SPPBG) effect. This arrayed system triggers local field enhancement promoting sensing proficiency of the device.

As, metal nanoparticles exhibit very high local field therefore, ellipsoidal plasmonic crystal is proposed which flaunts Fano resonance with applications in switching and lasing. The geometry of metal nanoparticles controls the plasmon resonance. Scattering models for ellipsoidal and cylindrical nano particles are compared and it is found that the spectral interference between the cavity mode and the background scattering mode results in sharp asymmetric peak, which is the defining characteristic of Fano resonance. Enhancement in the asymmetric

line shape of Fano resonance is observed and extensively examined for cavities in plasmonic crystals of ellipsoidal silver nanoparticles with hexagonal arrangement.

When the size of metal nanoparticles is less than 10nm and interparticle distance is in sub-nanometer dimensions, the system exhibit astounding behaviour. Skin depth dependence of metal nanoparticles system showing resonant plasmon tunnelling is studied. Gradient potential dependent skin-depth theory (GPST) is introduced to study resonant plasmon tunnelling in silver nanodisk dimer system. The region between adjacent silver nanodisks at sub-nanometer spacing, exhibit gradient potential due to the property of its geometry leading to the formation of tunnelling zone and is substantiated by finite difference time domain (FDTD) computational method. The proposed GPST can be used to predict the performance of plasmon tunnel diode, plasmon tunnelled field-effect transistors, plasmonic Josephson junction assisted superconductivity etc.

Further, incorporating metal nanoparticles with semiconductors give rise to plasmon-exciton coupling and hence have been used in plexcitonic interaction for devising composites. Plexcitonic systems formed by multi-layered silver-gallium arsenide-silver (Ag-GaAs-Ag) quantum nano-lenses are proposed and various optical properties are studied. Cavity defect support strongly confined mode. As the cavity mode resonates in ultra-violet regime, it can be an alternative for excimer lasers.

Plasmonics offer ultrafast, ultra-small and highly efficient devices. With metal nanoparticles tailoring and manipulation of light has become interesting thus the technology offers excellent applications with desired properties. Nano scale planar waveguides, faster chip and important role in cancer therapy are just a few examples of the unique applications it acclaims.

List of Publications

Papers in peer reviewed journals

1. **Dillu, V**. and Sinha, R. K. (2014) 'Surface plasmon polariton band gap enabled plasmonic Mach Zehnder interferometer: Design analysis and application', ***Plasmonics***, 9 (3) pp. 527-535. http://dx.doi.org/10.1007/s11468-013-9652-5

2. **Dillu, V.** and Sinha, R. K. (2013) 'Enhanced Fano resonance in silver ellipsoidal plasmonic crystal cavity', ***Journal of Applied Physics***, 114, pp. 234305. http://dx.doi.org/10.1063/1.4851775

3. **Dillu, V**., Shruti, Srivastava, T. and Sinha, R. K. (2013) 'Propagation characteristics of silver nanorods based compact waveguides for plasmonic circuitry', ***Physica E*** 48, pp.75-79. http://dx.doi.org/10.1016/j.physe.2012.11.025

4. **Dillu, V.** and R. K. Sinha, 'Resonant plasmon tunnelling in silver nanodisk dimer', Communicated.

Patent application

1. **Dillu, V**. and Sinha, R. K. (2013) 'A sensing system and a sensing device for detection of biological materials and method thereof', ***Indian Patent Application*** *No.: 1168/DEL/2013*

Papers in peer reviewed conference proceedings

1. **Dillu, V**. and Sinha, R. K. (2014, December) 'Ag-GaAs-Ag quantum nano-lenses system for plexcitonic interaction,' In ***Photonics 2014:*** *12th International Conference on Fiber Optics and Photonics, December 13-16, 2014,* **© OSA 2014** (T3A.42). http://dx.doi.org/10.1364/PHOTONICS.2014.T3A.42

2. **Dillu, V**., Rani, P., and Sinha, R. K. (2014, September) 'Field enhanced plexcitonic coupling between InAs quantum dot and silver film: highly sensitive plasmonic composite,' In ***SPIE*** *NanoScience+ Engineering, August 17-21, 2014* (pp. 91630W-91630W). International Society for Optics and Photonics.
http://dx. doi:10.1117/12.2061914

3. Rani, P., Kalra, Y., **Dillu, V**., and Sinha, R. K. (2014, September) 'Photonic crystal based nano-displacement sensor,' In ***SPIE*** *Optical Engineering+ Applications, August 17-21, 2014*, (pp. 92000Q-92000Q). International Society for Optics and Photonics.
http://dx. doi:10.1117/12.2061627

4. **Dillu, V.**, and Sinha, R. K. (2014, March) 'Quantum size effects on plasmonic band gap of silver nanodisk heptamer,' in ***ICOL-2014***, *International Conference on Optics and Optoelectronics, March 5-8, 2014, XXXVIII Symposium of Optical Society of India, IRDE, Dehradun, India. Received OSI '****Excellent Paper Presentation****'.*

5. **Dillu, V.,** and Sinha, R. K. (2013, December) Surface enhanced plasmonic coupling via localized silver nanoparticles between silicon slabs. In ***WRAP*** *Workshop on Recent Advances in Photonics, December 17-18, 2013* (pp. 1-2). **IEEE**
http://dx.doi:10.1109/WRAP.2013.6917636

6. **Dillu, V**., and Sinha, R. K. (2013, October) 'Tuning Fano resonance in plasmonic nanocavity for enhanced transmission' in Kang, I., Reitze, D., Alic, N. and Hagan, D (eds) ***Frontiers in Optics*** *2013, October 6-10, 2013, Orlando, Florida, United States, OSA Technical Digest, Optical Society of America,* pp. FTh3E-5.
Received ***'OSA Foundation Award'***
http://dx.doi.org/10.1364/FIO.2013.FTh3E.5

7. **Dillu, V.**, Shruti, S., and Sinha, R. K. (2013, September) 'Fano resonance in silver nanoparticles in SOI structure: design of plasmonic nano switch', in Stockman, M. I. (eds) ***SPIE*** *Optics +Photonics (NanoScience+ Engineering) August 25-29, 2013, San Diego, California, United States, International Society for Optics and Photonics,* Proc. of SPIE Vol. 8809, pp. 88091U.
http://dx.doi.org/10.1117/12.2023931

8. **Dillu, V.**, Singh, S., and Sinha, R. K. (2012, October) 'Subwavelength plasmonic metallic nanopillar based coupler', in Stockman, M. I. (eds) ***SPIE*** *Optics +Photonics (NanoScience+ Engineering), August 19-23, 2012, San Diego, California, United States, International Society for Optics and Photonics* Proc. of SPIE Vol. 8457, pp. 845726.
http://dx.doi.org/10.1117/12.929910

9. Singh, S., **Dillu, V.**, and Sinha, R. K. (2012, October) 'Hybrid metal-photonic crystal waveguide and cavities', in Stockman, M. I. (eds) ***SPIE*** *Optics +Photonics (NanoScience+ Engineering), August 19-23, 2012, San Diego, California, United States, International Society for Optics and Photonics,* Proc. of SPIE Vol. 8457, pp. 84573J.
http://dx.doi.org/10.1117/12.929794

10. **Dillu, V.**, and Sinha, R. K. (2012, September) 'Arrayed silver nanopillarsbased plasmonic nano-cavity for telecom wavelength', in IONS-ASIA-3, September 14-16, 2012, CIOMP, Changchun, China, International OSA Network of Students.
Received **'Second Prize for Poster presentation'**

11. **Dillu, V.**, and Sinha, R. K. (2012, December) 'Design and analysis of slow trapped plasmons through silver nanorods based Mach-Zehnder interferometer', in IONS-ASIA-4, December 7-8, 2012, Chennai, India, International OSA Network of Students.

12. **Dillu, V.**, Singh, S., and Sinha, R. K. (2011, September) 'Design and analysis of subwavelength plasmonic waveguide array', in Stockman, M. I. (eds) ***SPIE*** *Optics +Photonics (Photonic Devices+Applications), August 21-25, 2011, San Diego, California, United States, International Society for Optics and Photonics,* Proc. of SPIE Vol. 8096, pp. 80962F.
http://dx.doi.org/10.1117/12.892906

13. Singh, S., **Dillu, V.**, and Sinha, R. K. (2011, September) 'Infiltrated plasmonic photonic crystal cavity for sensing', in Yin, S. and Guo, R. (eds) ***SPIE*** *Optics +Photonics (Photonic Devices+ Applications), August 21-25, 2011, San Diego, California, United States, International Society for Optics and Photonics,* Proc. of SPIE Vol. 8120, pp. 81201F
http://dx.doi.org/10.1117/12.893754

14. Singh, S., **Dillu, V.**, Sinha, R. K. and Bhattacharyya, R. (2011, September) 'Terahertz wave propagation in surface plasmon photonic crystal', in Yin, S. and Guo, R. (eds) **SPIE** *Optics +Photonics (Photonic Devices+ Applications), August 21-25, 2011, San Diego, California, United States, International Society for Optics and Photonics,* Proc. of SPIE Vol. 8120, pp. 81200S.
http://dx.doi.org/10.1117/12.892903

15. **Dillu, V.** (2011, December) **'**Nanopillars based plasmonic waveguides and devices' in ***IONS-ASIA-2*** *December 1-2, 2011 at IIT Delhi, Delhi, India*, International OSA Network of Students,
Students' Invited Talk

16. **Dillu, V.**, Shruti., Srivastava, T., and Sinha, R. K. (2011, December) 'Plasmonic nanopillars based Y-splitter for visible regime' in ***IONS-ASIA-2*** *December 1-2, 2011 at IIT Delhi, Delhi, India*, International OSA Network of Students.

17. **Dillu, V.**, Shruti., Srivastava, T., and Sinha, R. K. (2011, December) 'Design and analysis of plasmonic bend waveguide', *in* ***Frontiers in Optics and Photonics-2011****, December 3-5, 2011 at IIT Delhi, India.*

18. Singh, S., **Dillu, V.**, Bhattacharyya, R., and Sinha, R. K. (2010, December) 'One-dimensional tunable surface plasmonic photonic crystal cavity', in Khijwania, S. K., Gupta, B. D., Pal, B. P., and Sharma, A. (eds) ***Photonics 2010****: Tenth International Conference on Fiber Optics and Photonics, December 11-15, 2010, IIT Guwahati, India, International Society for Optics and Photonics,* Proc. of **SPIE** Vol. 8173, pp. 81731J.
http://dx.doi.org/10.1117/12.899932

Contents

Declaration…… **i**

Certificate…….... **ii**

Acknowledgement…….. **iii**

Abstract……... **v**

List of Publications…… **viii**

Contents…….. **xi**

List of Figures…… **xv**

List of Tables…….. **xxii**

List of Acronyms…… **xxiii**

1. Introduction 1

1.1 Introduction…..…….. 1

1.1.1 Literature review.....…….....……... 1

1.2 Properties of plasmonic devices……..…….. 7

1.3 Applications of plasmonics...…… 9

1.4 Thesis scope and outline…...…… 11

1.4.1 Computational methods use..…… 12

1.4.1.1 Finite difference time domain……... 12

1.4.1.2 Plane wave expansion……... 12

1.4.2 Outline of the thesis....…….. 12

2. Plasmonic waveguides: Silver nanorods embedded on silicon-on-insulator 16

2.1 Introduction……..…… 16

2.1.1 Plasmonic band gap.....…… 16

2.1.1.1 Silver: preferred metal for plasmonic waveguides…... 17

2.1.1.2 Vertical orientation of nanorods over horizontal…….. 18

2.2 Basis structure offering plasmonic band gap and strong confinement to the plasmons……... 18

2.2.1 Optimized design parameters…… 20

2.2.2 Simulation parameters…….. 20
2.2.3 Band gap for the basis structure…… 21
2.2.4 Defect in basis structure: Waveguide……... 22
2.3 Realization of plasmonic waveguides: Straight, bend and Y-splitter 23
2.3.1 Straight waveguide…… 23
2.3.2 Bend design……... 24
2.3.3 Y-splitter……... 25
2.3.4 Propagation characteristics of the waveguides…… 25
2.3.4.1 Normalized power transmittance…….. 26
2.3.4.2 Quality factor…… 26
2.3.4.3 Fractional confinement factor…….. 26
2.3.4.4 Tolerance…….. 27
2.3.4.5 Propagation losses……. 27
2.4 Summary…… 27

3. Plasmonic Mach-Zehnder Interferometer 28
3.1 Introduction…… 28
3.1.1 Plasmonic Mach-Zehnder Interferometer……. 29
3.1.2 Surface plasmon polariton band gap……. 30
3.2 PMZI sensor design and structural parameters…….. 31
3.2.1 Working principle……. 32
3.2.2 Advantages of the proposed structure……... 32
3.2.3 Plasmon propagation through PMZI: SPPBG assistance……. 33
3.3 Results…… 34
3.3.1 Working wavelength for the device…….. 34
3.3.2 Analyte: cancer cells……. 36
3.3.3 Refractive index sensing……... 38
3.3.4 Spectral analysis…… 38
3.3.5 Sensitivity……. 40
3.3.6 Figure of merit…….. 42
3.3.7 Volumetric analysis…….. 42
3.3.8 Phase shift……. 43

3.4 Summary…… 45

4. Enhanced Fano resonance in silver ellipsoidal plasmonic crystal cavity 46

4.1 Introduction..……. 46

4.1.1 Resonance……. 46

4.1.2 Fano resonance…….. 47

4.1.3 Applications…….. 50

4.1.4 Fano resonance in metal nanoparticles……. 50

4.2 Silver ellipsoidal and cylindrical plasmonic crystal cavity…… 51

4.3 Scattering model for silver ellipsoidal and cylindrical plasmonic crystal……...…… 52

4.4 Results……. 58

4.4.1 Ultra high transmission in ellipsoidal silver nanorods cavity... 58

4.4.2 Higher harmonic generation……. 64

4.4.3 Power dependence and switching application…….. 65

4.4.4 Polarization dependence……... 67

4.5 Summary...……. 69

5. Resonant plasmon tunneling in silver nanodisk dimer 70

5.1 Introduction…….. 70

5.1.1 Resonant plasmon tunneling…… 70

5.1.2 Gradient potential dependent skin depth theory…… 72

5.1.3 Skin depth effect……... 73

5.2 Silver nanodisk dimer……..……. 75

5.3 Results…….……. 75

5.4 Summary..……. 82

6. Plexcitonic interaction 84

6.1 Introduction…… 84

6.1.1 Importance of plexcitonic interaction……... 85

6.2 Plexcitonic structures……. 85

6.2.1 Metal/semiconductor/metal nanodisk system……... 85

6.2.2 Semiconductor/metal/semiconductor/metal/semiconductor System…… 85
6.3 Silver-Galium Arsenide-Silver nanodisk system…….. 86
6.3.1 Structure and results……. 86
6.4 Indium Arsenide-Silver-Silicon-Silver-Indium Arsenide……. 89
6.4.1 Structure and result...…… 89
6.5 Summary…… 93

7. Summary and future scope 94
7.1 Summary…… 94
7.2 Scope for future work…… 96
References 98
Brief bio-data of the author 112

List of Figures

Figure 1.1	Plasma oscillations diagrammatically representing plasmons with respect to fixed positive ions in metals.	2
Figure 1.2	Types of plasmons volume or surface depending on the location of their existence.	3
Figure 1.3	SPPs have maximum field at the surface and decays exponentially away from the interface.	4
Figure 1.4	Length scales of surface plasmon polariton spans over seven orders of magnitude	5
Figure 1.5	Basic surface plasmon resonance instrument set up.	5
Figure 1.6	Types of plasmons depending upon the geometry of the metal structure used.	6
Figure 1.7	Operating speed and critical dimensions of various chip scale technologies highlighting the strengths of the different technologies.	8
Figure 1.8	Confinement of light in (a) photonic and (b) plasmonic waveguide.	8
Figure 2.1	Schematic of the basis waveguide cross-section (x-y plane) and top view in inset (x-z plane) of proposed basis waveguide comprising of silver nanorods on silicon on insulator (SOI) substrate.	19
Figure 2.2	Schematic of the plasmonic waveguide designed by introducing defect through the basis structure showing lateral and transverse view and also the mode profile through the defect.	21
Figure 2.3	Normalized transmission for the basis structure showing bandgap within 400-800nm and the inset shows electric field profile Ey depicting the light is forbidden from	22

propagation.

Figure 2.4 Normalized transmission for the proposed straight waveguide showing peak at λ=633nm, schematic of the structure and the Ey field profile in X-Z and X-Y planes are given in the inset. 23

Figure 2.5 Bend waveguide exhibiting the resonating peak at 633nm and the insets show the structure and the Ey field profile depicting how the energy is routing through the bend in the waveguide. 24

Figure 2.6 Normalized transmission for the proposed Y-splitter with resonating peak at λ=633nm. Schematic and the Ey field profile showing energy splitting into the two arms is given in the inset of (a). 25

Figure 3.1 Plasmonic Mach-Zehnder interferometer (PMZI) has the synergy of both the plasmonics and interferometry. 30

Figure 3.2 Schematic of the proposed PMZI sensor having Ag nanorods array vertically embedded into SOI in square lattice arrangement, inset shows the fortified core formed by Ag rods encompassing high refractive index Si for plasmon propagation. 32

Figure 3.3 Demonstration of plasmon propagation through the plasmonic Mach-Zehnder interferometer showing constructive interference at the output ensuring excellent performance of the device. 33

Figure 3.4 Transverse magnetic gap map (400nm-800nm) obtained for the base structure. 34

Figure 3.5 Electric field profile obtained for the device demonstrating plasmon propagation for the PMZI indicating perfect propagation for λ= 633nm. 35

Figure 3.6 (a), (b) and (c) Three dimensional (3D) contour plot of the field distribution of plasmon propagation through the device demonstrating its functioning for inputs λ= 200nm, 633nm and 900nm exhibiting constructive plasmon interference at λ=633 obtained for the optimized parameters of PMZI. 36

Figure 3.7 (a), (b) and (c) Normalized transmission obtained for different carcinoma cell lines representing blue shift with increasing RI for operational wavelength λ_1, λ_2 and λ_3 respectively 38

Figure 3.8 Logarithmic variation of sensitivity of the device with respect to the change in refractive index of the cancer cells. 39

Figure 3.9 Logarithmic variation of sensitivity of the device with respect to the change in refractive index of the cancer cells. 41

Figure 3.10 (a) and (b): Cancer cell line micrographs of breast and blood cells representing dense cell constituents causing augmentation of refractive index 41

Figure 3.11 Electric field profile of propagating mode through the PMZI with no analyte in the sensing arm i.e. similar environmental condition in the two arms of the PMZI showing the centrally located field profile at the output end. (b), (c) and (d) Represent the effect of increasing analyte volume as V_1, V_2 and V_3 respectively, on the field profile at the output, showing plasmon-analyte interaction. 43

Figure 3.12 (a) Variation of power at the output through the span of time. Inset show expanded scale for measuring the shifts. (b) Plot of phase shift with refractive index showing 44

	significant change yielding easy detection of carcinoma cell lines.	
Figure 4.1	Simple representation of resonance phenomenon where the system exhibits resonance at frequency *Fb* having greater amplitude at point B, unlike frequency at point A and C.	47
Figure 4.2	Asymmetric resonance shape is the defining characteristic of Fano resonance.	48
Figure 4.3	Fano resonance shape depending upon the asymmetry parameter q.	49
Figure 4.4	Variation of real and imaginary part of dielectric constant of silver with wavelength.	51
Figure 4.5	Hexagonal arrangement of silver (a) ellipsoidal and (b) cylindrical plasmonic crystal cavity.	52
Figure 4.6	Cavity response of hexagonally arranged ellipsoidal silver nanoparticles, the zoomed out illustration shows the asymmetry in the output response. Inset (i) displays the symmetric input source profile, inset (ii) presents the semi-axes ‘a’, ‘b’ and ‘c’ of the ellipsoid and inset (iii) presents cavity in the hexagonal arrangement of the silver ellipsoids.	59
Figure 4.7	Cavity response of hexagonally arranged cylindrical silver nanorods with inset (i) presenting the arrangement of the cylindrical nanorods.	60
Figure 4.8	3D contour plot of the field distribution in the cavity formed in ESN and CSN.	61
Figure 4.9	(a) and (b) Transmission characteristics (1-Extinction; for normalized output) of the ESN cavity for different input wavelength presenting the variation in Fano lineshapes.	62
Figure 4.10	Spectral variation of peak amplitude for the ESN cavity	64

highlighting switching application.

Figure 4.11 (a), (b) and (c) Power dependence of Fano lineshapes showing the adaptation of resonance profile with varying input power. TM polarization establish strong mutual coupling resulting in distinct Fano profile. 66

Figure 4.12 (a), (b) and (c) Effect of TE polarization on the Fano lineshapes validating weak mutual coupling. 68

Figure 5.1 Schematic representations of closely spaced silver nanodisks revealing formation of tunnelling zone between the nanodisks. (a) Closely spaced silver nanodisks with subnanometer interparticle distance. (b) Variation of potential between the nanodisks. (c) and (d)The region of high potential overlaps as the disks come closer forming a tunnelling zone which assists resonant plasmon tunnelling. (e) Array of closely spaced nanodisks with tunnelling zone forming a periodic arrangement. 73

Figure 5.2 Plot showing skin depth dependence on incident wavelength and the corresponding frequency. 74

Figure 5.3 Normalized tranimission spectra for a silver nanodisk revealing allowed energy bands for the system. The inset highlights the wavelength of 1.1μm gains the most due to skin depth effect. 76

Figure 5.4 (a) System of silver nanodisk dimer with subnanometer interparticle spacing with 'L' as the launch and monitors M_1, M_2 and M_3 to record the transmission spectra. (b) Electric field profile for the nanodisk dimer with significant field intensity between the disks edifying the tunnelling zone. (c) to (j) Diagrammatic representation of variation of distance between the dimers from d_1 to d_8 (k) and (l) Illustration depicting formation of node and 77

antinode between the nanodisk consequently contributing to the total tunnelled efficiency.

Figure 5.5 (a), (b) and (c) Show transmission spectra obtained on monitors M_1, M_2 and M_3 respectively with wavelength and energy eigen values in (b) and (c) after tunnelling through the first and second nanodisk. 80

Figure 5.6 (a) to (h) Transmission spectra obtained on monitors M_1 M_2 and M_3 with distance varying from d_1 to d_8 between the nanodisks showing variation of tunnelling efficiency with varying interparticle distance. 81

Figure 5.7 (a) to (h) Electric field profile of the silver nanodisks quantum system with varying distance demonstrating formation of tunnelling zone when the distance between the nanodisks decreases from d_1 to d_8. 82

Figure 6.1 Three layered system of Ag-GaAs-Ag nano-disks in hexagonal arrangement. 86

Figure 6.2 Hybrid band structure of the proposed plexcitonic system with odd parity for TE gap and even parity for TM gap. 87

Figure 6.3 Transmission characteristics of the Ag-GaAs-Ag nano-lenses plexcitonic system for TM waves (Monitor value represents transmission). 87

Figure 6.4 Transmission characteristics of the Ag-GaAs-Ag nano-lenses plexcitonic system for TE waves (Monitor value represents transmission). 88

Figure 6.5 Strongly resonating peak is obtained for the input of 193nm with enhanced signal with respect to the input. 88

Figure 6.6 3D contour for electric field Ey, for the cavity defect showing strongly confined intense cavity resonance 89

Figure 6.7 Schematic of the proposed structure for plexcitonic waveguide system. 90

Figure 6.8	Propagation of plasmons through silver-silicon-silver waveguide.	90
Figure 6.9	Propagation of resultant plexcitons through silver-silicon-silver waveguide with InAs quantum dots on one surface of the proposed system.	91
Figure 6.10	Propagation characteristics of the plexcitons through InAs-Ag-Si-Ag-InAs waveguide.	91
Figure 6.11	(a) and (b) The propagation length of the resultant wave also depends on the thickness of silver film and decreases with decreasing thickness from 167nm to 55nm as given in (a) and (b) respectively.	92
Figure 6.12	(a) and (b) Field enhancement arising due to the coupling of plexcitons between InAs QD with silver film passing through the silicon waveguide depending upon the depth to which QDs are etched into silver. (a) QDs on the surface of silver and (b)QDs etched into silver.	92

List of Tables

Table 3.1 Calculated values of wavelength shifts $\Delta\lambda$, sensitivity S, FWHM $\delta\lambda$ and figure of merit FOM obtained for various cancer cell lines.

Table 3.2 Volumetric analysis of the sensor.

Table 3.3 Path difference and phase difference obtained for different cancer cell lines.

Table 4.1 Peak amplitude values obtained for peak 1 and 2.

Table 4.2 Ratio of peak amplitudes Peak 2/Peak 1 for different input power P_1, P_2, P_3 and P_4.

List of Acronyms

ATR	Attenuated total reflection
CSN	Cylindrical silver nanorods
EBL	Electron beam lithography
EM	Electromagnetic
EOT	Extraordinary optical transmission
ESN	Ellipsoidal silver nanorods
FDTD	Finite difference time domain
FIB	Focused ion beam
GPST	Gradient potential dependent skin depth theory
HHG	Higher Harmonic Generation
IMI	Insulator-metal-insulator
LSP	Localized surface plasmon
LSPR	Localized surface plasmon resonance
MIM	Metal-insulator-metal
MNPs	Metal nanoparticles
PML	Perfectly matched layer
PMZI	Plasmonic Mach-Zehnder interferometer
PWE	Plane wave expansion
QD	Quantum Dot
RI	Refractive index
SERS	Surface enhanced Raman spectroscopy
SOI	Silicon on insulator
SP	Surface plasmon
SPP	Surface plasmon polariton
SPPBG	Surface plasmon polariton band gap
SPR	Surface plasmon resonance

Chapter 1
Introduction

1.1 Introduction

Plasmonics is the study and application of interaction of electromagnetic (EM) field oscillations with free electrons in a metal. These free electrons present in the metal can be excited by the electric component of incident light to render collective oscillations. The subsequent collective oscillations of free electrons are called plasmons. Plasmons are quanta of electron oscillations in metal and when it interacts with photon (quanta of light) it results in polariton which is quanta of EM wave travelling at the metal-dielectric interface. The development of the subject and how it has convincingly become the platform of the present day technology has been briefly discussed below.

1.1.1 Literature review

Plasmons were first observed by R W Woods [1, 2] in 1902 when he illuminated polarized light onto a metal-backed diffraction grating and found a pattern of unusual dark and light bands in the reflected light. These anomalies were theoretically treated by Lord Rayleigh in 1907 [3] where he used expansion of scattered electromagnetic field in terms of outgoing waves only. He reported that scattered field was singular at wavelengths (Rayleigh wavelengths) when spectral orders emerged from the grating at the grazing angle. These Rayleigh wavelengths correspond to the Wood's anomalies.

Further, in fifties more experiments were done on electron energy losses in gases and on thin foil. According to Pines and Bohm these energy losses were due to the excitation of conducting electrons creating plasma oscillations or plasmons [4-7]. The existence of surface plasmon was first predicted by Ritchie in his highly cited work where he studied plasma losses by fast electron in thin

films [8]. The energy loss resulted from excitation of surface plasmon (SP) oscillations where a part restoring electric field extended beyond the system boundaries. Hence presence of analyte or any film on the interface will shift the surface plasmon oscillations. This forms the platform for electromagnetic evanescent waves at the surface of metal. Later, Kretschmann and Otto demonstrated optical excitation of surface plasmons by means of attenuated total reflection (ATR) [9, 10].

There are two major approaches to excite surface plasmons, namely attenuated total reflection in prism coupler based structures [11] and by using diffraction grating [12-14]. ATR based method is widely used due to its simplicity for characterization of thin films and bio-chemical sensing [15-18] but diffraction grating based surface plasmon resonance (SPR) sensors has been researched as a substitute over cumbersome prism based technique.

Plasmon is defined as a quantum of plasma oscillation. Plasma oscillations are rapid oscillations of electron density in conducting media for example metal. They are described as collective oscillation of free electron gas density with respect to the fixed positive ions in metals (Figure 1.1).

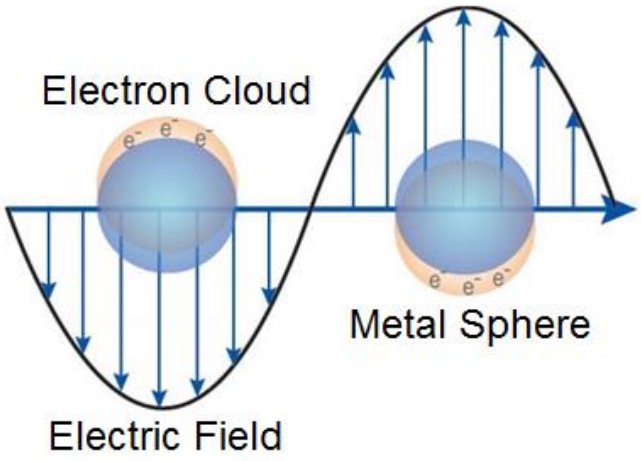

[1]

Figure 1.1 Plasma oscillations diagrammatically representing plasmons with respect to fixed positive ions in metals.

[1] Image credit: http://www.livenano.org/technologies/how-plasmons-work/attachment/plasmon/

The frequency of these plasma oscillations can be described in terms of the free electron density and effective mass of the electrons and is given below:

$$\omega_p^2 = \frac{ne^2}{m^*\varepsilon_0} \tag{1.1}$$

where m^* is the effective mass of electrons and n is the free electron density [19].

Plasmons can be described as volume plasmons and surface plasmons [19, 20]. The longitudinal free electrons density oscillations can propagate through the volume that is the bulk of the metal and the quanta of such oscillations are called 'volume plasmons' whereas those that can propagate along a metallic surface are called surface plasmons see Figure 1.2. Surface plasmons show evident response to the changes made in the environment and hence can be utilized for sensing.

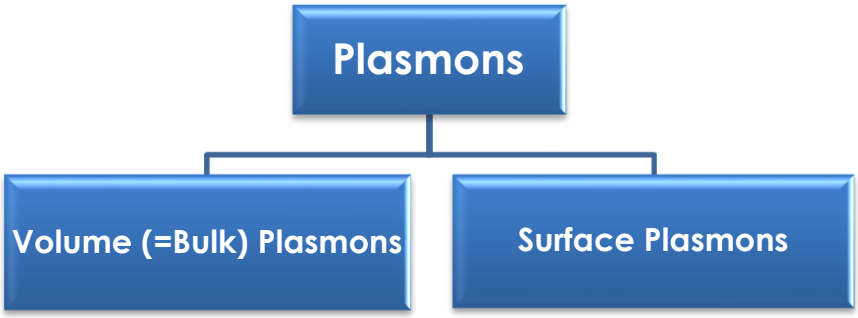

Figure 1.2 Types of plasmons as volume or surface depending on the location of their existence.

Surface plasmons can couple with photon to create polariton to be specific surface plasmon polariton (SPP). These are transverse magnetic waves resulting from interaction between photons and plasmons and propagate along the metal-dielectric interface having dielectric constants ε_m and ε_d of opposite sign. SPP have field that decays exponentially with distance from the interface thus resulting in bound modes. Diagrammatic representation of propagating SPP at a metal-dielectric interface is shown in Figure 1.3

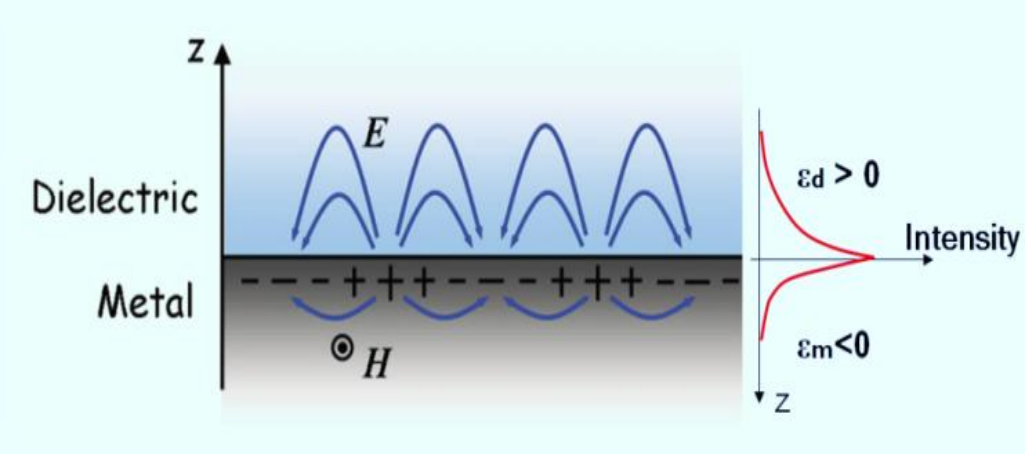

[2]

Figure 1.3 SPPs have maximum field at the surface and decays exponentially away from the interface.

There are few characteristic length scales associated with SPPs as displayed in Figure 1.4. To begin with there is penetration depth of the SP electromagnetic field into the metal surface δ_m which is on the order of 10nm [21]. This length δ_m provides a minimum feature size to the SP based devices.

Next length to be mentioned is the penetration depth of the SP field into the dielectric medium δ_d and is on the order of hundreds of nanometer and provides the upper limit on the size of the device.

Third characteristic length is the SPP propagation length δ_{SPP} along the metal dielectric interface which governs how far the plasmons can travel and is defined as length propagated by plasmons by losing 1/e times of the initial intensity. This length can reach millimeter depending upon low loss propagation.

Another important length parameter is λ_{SPP} which is the wavelength of the propagating SPP. Metals have complex dielectric constant having a real and an imaginary part. The real part of the complex dielectric constant relates to the $\lambda_{SPP.}$ The SPP wavelength λ_{SPP} is smaller than the free space wavelength λ_0 and thus reflects the bound nature of SPP modes on a planar surface [22]

[2] Image credit: http://www.sciencedirect.com/science/article/pii/S1369702106715723

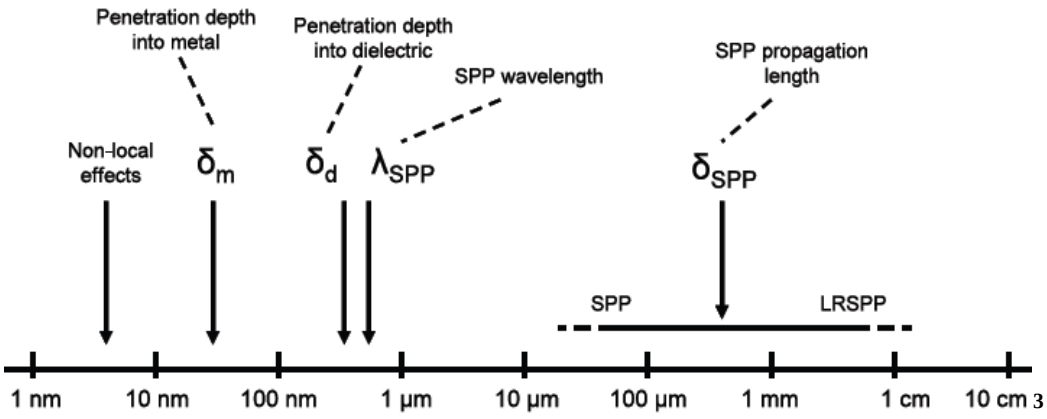

[3]

Figure 1.4 Length scales of surface plasmon polariton spans over seven orders of magnitude.

Surface plasmon resonance (SPR) is the resonant oscillation condition of conduction electrons at the metal-dielectric interface when the frequency of incident photons matches with the natural frequency of surface electrons. SPR is a non-destructive technique to analyze analytes such as thin layer of molecules. Basic instrument set up for SPR is given in Figure 1.5. Using SPR one can detect changes in refractive index occurring near the metal surface.

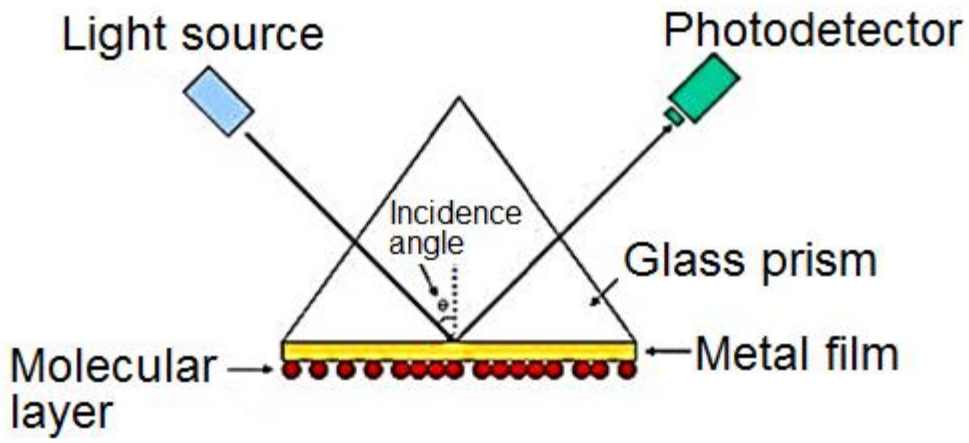

[4]

Figure 1.5 Basic surface plasmon resonance instrument set up.

[3] Image credit: http://iopscience.iop.org/article/10.1088/1464-4258/8/4/S06/meta;jsessionid=A9D69B504045024C35A11CAAAB54D517.c1

[4] Image credit: http://www.uweb.engr.washington.edu/research/tutorials/plasmon.html

Plasmons can further be classified as propagating and non-propagating plasmons depending upon the geometry of the metal structure used (see Figure 1.6). Surface plasmons are propagating plasmons or delocalized plasmons present at the interface of thin metal films whereas plasmons present at the metal nanoparticles are called localized surface plasmons (LSP). LSP can be described as confinement of surface plasmon in a nanoparticle of size comparable to or smaller than the wavelength of incident light.

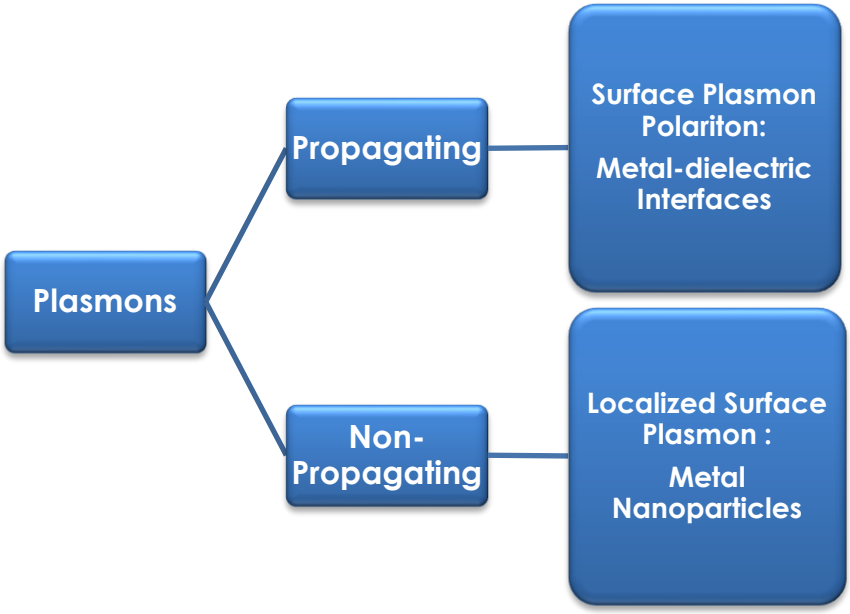

Figure 1.6 Types of plasmons depending upon the geometry of the metal structure used.

LSP show two extremely important effects: (i) local field enhancement and (ii) nanoparticle's optical absorption yields maxima at plasmon resonant frequency. The plasmon resonance at the metal nanoparticles is termed as localized surface plasmon resonance (LSPR).

Whether it is surface plasmon polaritons or localized surface plasmons, their properties are incredible establishing it as the cutting-edge technology. Hence, some of the important properties of plasmonics that has made it state-of-art-technology are glanced in the next section.

1.2 Properties of plasmonic devices

Plasmonics offers exceptional properties to the device technology today. It has imparted revolutionary influence to fundamental physics as well as to the practical applications in multiple disciplines [23]. It is a technology that squeezes electromagnetic waves into miniscule structures [24-27]; can yield a new generation of superfast computers [24, 27-29], can perform ultrasensitive molecular detection [30, 31]; plasmonic materials can even alter the electromagnetic field around an object so as to make them invisible [32-34] and hence its significance is evident.

Plasmonics has paved the way for realizing nanoscale optical devices by allowing flow of electromagnetic energy below the diffraction limit of light [25, 35, 36] leading to miniaturization of photonic circuits with length scales smaller than those currently achieved [37-39].

This technology has improved data storage [40], light generation [41], microscopy [42] etc. and by using metal nanoparticles (MNPs) which exhibits enhanced local field plasmonics grants astounding applications in optical transmission [43], switching [44], resonant light scattering [45], bio-chemical sensors [46, 47] etc. Ultrafast, ultra-small and highly efficient devices are the need of time and plasmonics can cater these demands. With metal nanoparticles, tailoring and manipulation of light has become interesting thus the technology offers excellent applications with desired properties.

Plasmonics has potential to enhance the processing speed of the integrated circuits [48]. Figure 1.7 illustrates the operating speed and the critical dimension of various chip scale device technology and it is observed that plasmonics offers what electronics and photonics cannot handle individually, that is: plasmonic devices can operate on the size of electronics and the speed of photonics.

Electronic interconnects are limited by thermal and signal delay issues thereby decreasing processor speed. On the other hand optical interconnects have

large data carrying capacity but are limited in size by fundamental laws of diffraction. Therefore present device technology faces a major challenge due to the size mismatch between electronic and photonic components. Thus plasmonics lays a platform merging photonics and electronics at nanoscale dimension [49] and has the synergy of both the technologies.

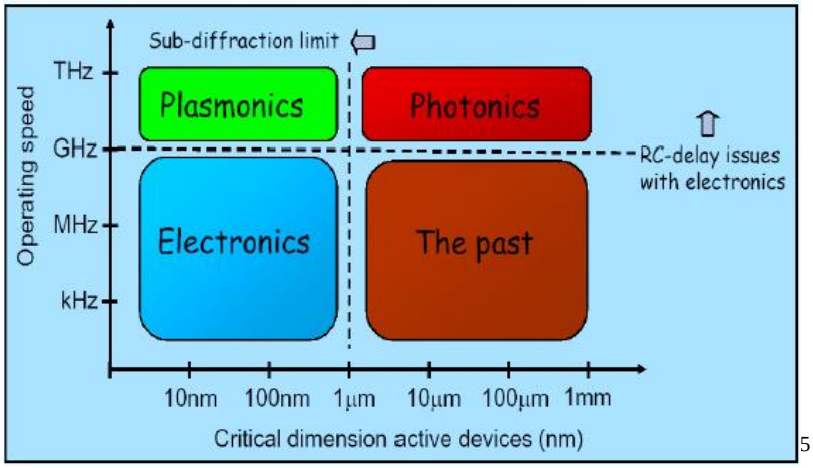

[5]

Figure 1.7 Operating speed and critical dimensions of various chip scale technologies highlighting the strengths of the different technologies.

Plasmonics can achieve subwavelength confinement of light below diffraction limit [21]. Figure 1.8 gives the glimpse to understand light confinement in photonic and plasmonic waveguide.

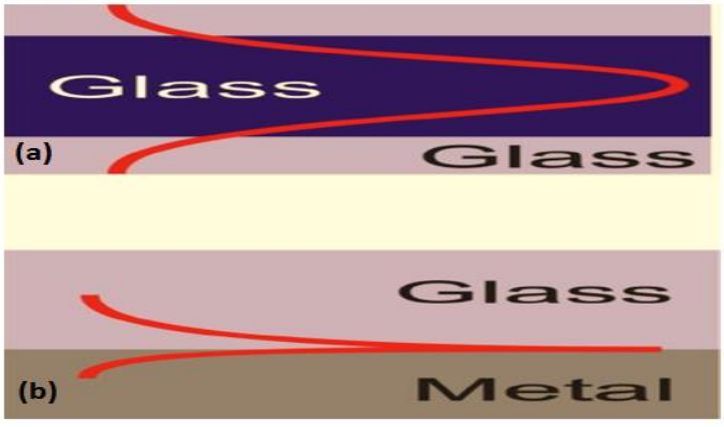

Figure 1.8 Confinement of light in (a) photonic and (b) plasmonic waveguide.

[5] Image credit: http://www.sciencedirect.com/science/article/pii/S1369702106715723

Plasmonics allows extreme light concentration [25] and hence achieve field enhancement giving rise to extraordinary optical transmission (EOT) [50]. EOT is highly enhanced transmission of light through a subwavelength aperture in an otherwise opaque metallic film which has been patterned with a regularly repeating periodic structure [51].

Metal nanostructures exhibit plasmonic coupling [52]. MNPs can also act as antennae and allow coupling of light to propagating plasmons on metal nanowires [53]. Plasmonic nanostructures facilitate efficient coupling of light into solar cells [54].

Embellished with all these unique properties mentioned above, plasmonics have extensive applications as conferred in the following.

1.3 Applications of plasmonics

An important application of plasmonics is bio-sensing. Plasmonic bio-sensors mostly occupy metal nanoparticles exhibiting localized surface plasmon resonance or plasmonic band gap for bio-sensing [55-58]. This application is based on the property of tunability of plasmon resonance.

Surface enhanced Raman spectroscopy (SERS) is a surface sensitive technique that enhances Raman scattering by molecules adsorbed on rough metal surfaces or by plasmonic nanostructures [59, 60]. It helps in probing single molecules [61], can detect the presence of low abundance biomolecules, and can therefore detect proteins in body fluids [62]. This application depends on near field enhancement of plasmons.

Plasmonic laser nano-antennae generate enhanced and spatially confined optical near fields and hence depend on near field enhancement of plasmons. It involves interaction of light with MNPs thereby exhibiting LSPR. LSPR at metal nanoparticle can couple to the EM fields emitted by nearby present molecules, atoms, or quantum dots, leading in turn to a strong modification of the radiative and nonradiative properties of the emitter. As LSPR enable an efficient transfer of

EM energy from the near to the far-field of metal NPs these plasmonic nanostructures act as nanoantennae [63].

Metallic probe can be used to trap small particles. It is observed that strong field enhancement due to the scattered light from gold probe tip can generate trapping potential to capture nanoparticles [64]. This application makes use of near and far-field enhancement of plasmons.

Optical superlenses, far-field optical hyperlenses comprising of thin silver film or periodic stack of silver nanoparticles promise sub-diffraction limit imaging. Superlens allows the recovery of evanescent waves in an image via the excitation of surface plasmons. Scattered TM evanescent waves from the object are coupled into the surface plasmon resonance of the silver film, and they become a primary component for restoring a sub–diffraction-limited image [65]. Hyperlens magnifies the object by transforming the scattered evanescent waves into propagating waves in the anisotropic medium, projecting a high-resolution image into the far field [66].

Once again MNPs provide a powerful tool for innovative light based cancer therapy due to their strongly resonant light absorbing and scattering properties. By manipulating the size and shape of MNPs their optical resonance can be tuned any specific wavelength. Blood cells and tissue transmit maximum in near infrared region and MNPs resonance can be tuned to this region. When these MNPS are illuminated they act as nanoscale heat source causing photothermal cell death and reducing tumor [67].

It is an exceptional property of metallic nanostructures to enable routing and manipulation of light at nanoscale dimensions, to concentrate light to subwavelength volume that has paved the way for nanophotonics [25, 48]. Metal nanoparticles array serve the role nanoscale guiding showing high confinement of electromagnetic energy with possibility of highly variable geometry and switching [68].

These applications that are immense and touch many aspects of science and technology have made plasmonics forerunner in research. It is the ever increasing demand for ultrafast, power efficient, lossless transfer of energy, data processing capabilities that highly efficient ultra-compact plasmonic waveguides are required. Also for improved medical facilities there is need of highly sensitive devices. These demands can be achieve by exploring more on this subject and hence it provides the motivation to the work done in this thesis which is briefly outlined below.

1.4 Thesis scope and outline

There is an ever increasing need for strong confinement of light with larger propagation lengths and low losses. Biggest challenge plasmonic circuits face is the short propagation length of surface plasmons. As the confinement increases in the plasmonic devices, the resistive damping increases thereby decreasing propagation length.

In this thesis we propose a novel method to yield strong confinement of light with low losses for plasmon propagation intended for plasmonic waveguides and devices with high efficiency and compact design.

The foremost idea is to employ metal nanoparticles to form plasmonic crystals which exhibits plasmonic band gap which can be exploited for desired applications such as waveguidance, sensing etc.

Closely spaced periodic array of silver nanoparticles embedded on silicon-on-insulator substrate is used to model plasmonic waveguides. Periodic arrangement of MNPs give rise to surface plasmon polariton band gap (SPPBG) effect. The SPPBG effect allows lossless plasmon propagation; SOI substrate renders transverse confinement and use of MNPs results in local field enhancement that assist plasmon amplification. Following are the computational methods used in modelling the designs of the waveguides and devices.

1.4.1 Computational methods used

1.4.1.1 Finite difference time domain

Finite-difference time-domain (FDTD) is a numerical analysis technique used for modeling computational electrodynamics (finding approximate solutions to the associated system of differential equations). It is a time-domain method; therefore FDTD solutions can cover a wide frequency range with a single simulation run, and are ideal for treating complex plasmonic geometries.

1.4.1.2 Plane wave expansion

Plane wave expansion method (PWE) refers to a computational technique in electromagnetics to solve the Maxwell's equations by formulating an eigenvalue problem out of the equation. This method solves the band structure (dispersion relation) of specific periodic geometries. PWE is traceable to the analytical formulations, and is useful in calculating modal solutions of Maxwell's equations over an inhomogeneous or periodic geometry. It is specifically tuned to solve problems in a time-harmonic form. The method is used to approximate the plasmonic band gap exhibited by the arrayed plasmonic crystal.

These computational techniques are used in modelling of various waveguides and devices, in studying their propagation characteristics, obtaining the band gap for the estimation of allowed and forbidden wavelengths. The outline of the work carried out in this thesis is given below.

1.4.2 Outline of the thesis

The research work carried out in this thesis has been briefed in the following:

Chapter 1 starts with brief introduction to plasmonics and to the research work carried out in the thesis. The main objective is to exploit metal nanoparticles to obtain remarkable performance of the plasmonic devices.

Chapter 2 reports silver metal nanorods embedded on silicon on insulator substrate for devising different ultra-compact plasmonic waveguides that is to say

straight waveguide, y-splitter and bend design with applications in achieving compact plasmonic circuits. Silver nanorods array palisading silicon to form core of SOI waveguide is theoretically modelled. Proposed geometry serves as the basis waveguide for different devices. Propagation characteristics of the waveguide expose plasmonic bandgap in the visible regime. Basis waveguide exhibit low loss propagation, larger propagation length and strong confinement of the traversing plasmonic mode. Narrow transmission bandwidth of ~10nm with quality factor and confinement factor of 97.5 and 92% is achieved respectively, confirming strong confinement of the propagating mode at 633nm and the losses calculated in dB/μm for the waveguide is found to be 0.75dB/μm for straight waveguide. Further, Y-splitter and bend design are also implemented successfully, offering components for high density plasmonic circuitry.

Chapter 3 describes plasmonic Mach-Zehnder interferometer (PMZI) for refractive index sensing with applications in sorting and classification of different types of cancer cells. Surface plasmon polariton band gap enabled PMZI is proposed which comprises of array of silver nanorods embedded upright into SOI substrate and have analyzed its potential in sensing, intended for cancer therapy. Periodic arrangement of nanorods embedded into SOI substrate grants strong spatial confinement and assist waveguidance to the propagating plasmon mode due to the SPPBG effect. This arrayed system triggers local field enhancement promoting sensing proficiency of the device and is assessed in terms of wavelength and phase shift. The structural parameters of PMZI are optimized in compliance with the plasmonic band gap in the range of 400nm-800nm yielding exceptionally high sensitivity of 5678nm/RIU at 633 nm. Volumetric analysis of the analyte reveals that very small analyte volume of the order of 10-15 cc is sufficient to yield significant phase shift. Phase shift obtained for the breast adenocarcinoma and blood cancer cell lines are 1.2357radian and 0.3351radian respectively which read very high value of phase shifts to identify extremely small changes in refractive index of the analyte. Figure of merit calculated

thereby expose impressive device performance outdoing preceding plasmonic sensors leading to validation of proposed ultra-compact sensitive PMZI design.

Chapter 4 highlights that the geometry of metal nanoparticles control the plasmon resonance. Silver ellipsoidal plasmonic crystal cavity exhibit enhanced Fano resonance with applications in switching and lasing. Enhancement in the asymmetric line shape of Fano resonance is observed and extensively examined for cavities in plasmonic crystals of ellipsoidal silver nanoparticles with hexagonal arrangement. Scattering models for ellipsoidal and cylindrical nanoparticles are compared and it is found that the spectral interference between the cavity mode and the background scattering mode results in a sharp asymmetric peak, which is the defining characteristic of Fano resonance. The cavity in ellipsoidal nanoparticles yields high transmission. Higher harmonic generation is also observed, which confirms the ultrahigh cavity response in ellipsoidal nanoparticles. The effect of power variation on the Fano resonance profile is described, and its application in the field of switching is explored. In addition, the influence of mutual interparticle coupling on Fano line shapes for transverse electric and transverse magnetic polarization is reported. The extraordinary rise in asymmetric line shapes of the Fano resonance promises profound applications in the field of sensing, switching and lasing devices.

Chapter 5 describes gradient potential dependent skin-depth theory (GPST) to study quantum resonant plasmon tunnelling in silver nanodisk dimer system. The region between adjacent silver nanodisks at sub-nanometer spacing, exhibit gradient potential due to the property of its geometry leading to the formation of tunnelling zone and is substantiated by finite difference time domain computational method. Significantly, the energy eigen values and hence the wavelength eigen values are obtained for the quantum system of silver nanodisk dimer. Incident wavelength influences the skin depth, which along with local enhanced field around each nanoparticle assists quantum plasmonic resonant tunnelling. The proposed GPST can be used to predict the performance of

plasmon tunnel diode, plasmon tunnelled field-effect transistors, plasmonic Josephson junction assisted superconductivity etc.

Chapter 6 reports plexcitonic system formed by multi-layered silver-gallium arsenide-silver (Ag-GaAs-Ag) quantum nano-lenses and various optical properties using finite difference time domain method are studied. Interaction between plasmons and excitons from semiconductor quantum dots (QDs) give rise to plexcitons which results in enhanced emission, allows controlled energy transfer and can also modify spontaneous emission in QDs. Plane wave expansion method reveals hybrid band-structure in the ultraviolet regime of the electromagnetic spectrum. Proposed metal-semiconductor-metal system of quantum nano-lenses excite plexcitonic coupling and have important applications in lasing, nano-antennae, Fano devices etc. Cavity defect support strongly confined mode. As the cavity mode resonates in ultra-violet regime, it can be an alternative for excimer lasers.

Chapter 7 summarizes the research work done in the previous chapters and describes the future scope of the research work carried out in the thesis.

Chapter 2
Plasmonic waveguides: Silver nanorods embedded on silicon-on-insulator[1]

2.1 Introduction

As mentioned in the previous chapter, plasmonics deals with constricting electromagnetic radiation into subwavelength devices and offers extraordinary applications outdoing preceding technologies. Besides, the recent advancement in nanotechnology and nanophotonics has revolutionized the field of plasmonics promising miniaturization of circuitry to nanoscale dimensions and provides huge data transmission at the bandwidth of photonics [21, 36, and 69]. For devising components of plasmonic circuitry, metal nanostructures of different geometries with varied arrangements have been used such as metal-insulator-metal (MIM), insulator-metal-insulator (IMI), dielectric loaded surface plasmon polariton waveguides (DLSPPW), plasmonic ridge, rib and metal gap waveguides [70-73]. These geometries involve plane sheets of metal that offers higher losses thus, to overcome these losses metal nanoparticles based design is proposed which forms the plasmonic crystal exhibiting plasmonic band gap as discussed in the next section.

2.1.1 Plasmonic band gap

It is comprehended from the above section that MNPs are better substitute over planar sheet of metal. Now with the developments observed in nanotechnology it is now possible to incorporate metal nanoparticles (MNPs) as a substitute of

[1]A part of the results reported in this chapter has been published in the paper 'Propagation characteristics of silver nanorods based compact waveguides for plasmonic circuitry', *Physica E* 48, pp.75-79 (2013).*http://dx.doi.org/10.1016/j.physe.2012.11.025*

metal/insulator geometry [74]. Periodic arrangements of MNPs forms plasmonic crystal that give rise to plasmonic band gap thus allowing propagation of plasmons of desired wavelengths with low losses thus yielding larger propagation lengths yet strongly confining the light. Not only that, MNPs give rise to local field enhancement and nanoparticles based waveguides guide light via near field coupling. MNPs instigate local amplification of the signal which can be used for lasing or sensing and their resonance can be easily tailored by changing the shape and their size thereby allow controlled manipulation of light as desired. Therefore metal nanoparticles ameliorate plasmonic waveguides due to nanoscale - confinement, guiding via plasmonic band gap, imaging and show comparatively low propagation losses because of their unique optical properties. These plasmonic crystals exhibiting plasmonic band gap can be formed by patterning of metal nanoparticles and is discoursed in next few lines.

As nanotechnology and more importantly research advances they offer improved techniques for patterning of metal nanoparticles and hence a more ordered plasmonic crystal. Elelectron beam lithography (EBL), focused ion beam (FIB), nanosphere lithography and soft nanoimprint lithography can be employed for fabrication of uniformly sized sub nanometer metal nanoparticles having required density [75-79]. Mainly gold and silver are incorporated in devising plasmonic structures but for waveguidance where losses are to be minimized silver is preferred as it will be seen in the next section.

2.1.1.1 Silver: preferred metal for plasmonic waveguides

It is observed that among all the metallic elements, silver (Ag), has the smallest damping constant Γ and is the best-performing choice at optical frequencies i.e. 400-700nm [80]. Gold can be used as well but it has a larger Γ than silver and is often the metal of choice at lower near infrared frequencies. Also, gold has high interband losses in the visible spectrum. Similarly, copper, platinum, palladium are avoided due to large interband losses over most of the visible spectrum. Thus,

silver has predominately been the material of choice for plasmonic applications around the optical frequencies.

Another important observation is that Ag particles in air have plasmon resonances at 350nm-480nm but they can be red-shifted in a controlled way over the entire 500-1500nm spectral range by partially embedding them in SiO_2, Si_3N_4 or Si [81]. Further, it is the arrangement of nanoparticles, lattice structure, and their shapes and sizes that controls the plasmon resonance and can be manipulated by changing them. In this chapter vertical arrangement of silver nanorods has been used and the comprehension for using this arrangement is discussed in the next section.

2.1.1.2 Vertical orientation of nanorods over horizontal

Integrating horizontally lying nanorod structures with main circuitry is a challenge and hinders the efficient excitation of the surface plasmon polaritons (SPPs) which are excited using end fire excitation technique [82] or the prism coupling [83], these designs are often cumbersome to be used in chip integration.

To overcome this difficulty, silver (Ag) nanorods are embedded perpendicularly into semiconductor material. This orientation facilitates the option of making planar components for plasmonic circuitry as well as allow efficient coupling with parallel devices. Hence vertical orientation is used in the proposed basis structure and thereafter the plasmonic waveguides discussed in this chapter.

2.2 Basis structure offering plasmonic band gap and strong confinement to the plasmons

Analogous to photonic crystals, an array of metal nanoparticles offers plasmonic band gap and is engineered for different device application.

A new design for compact plasmonic waveguide is proposed. Silver nanorods are embedded in silicon on insulator substrate in a square lattice array

as shown in Figure 2.1 with the intention that waveguide exhibits stronger confinement having appreciable propagation length for 633nm wavelength and demonstrating substantial quality factor, thus can be efficiently implemented in high density chip integration.

Nanorods having negative dielectric constant are embedded into SOI which palisade high refractive index silicon (Si) core and have silica (SiO_2) base as substrate resulting in the proposed core for light propagation.

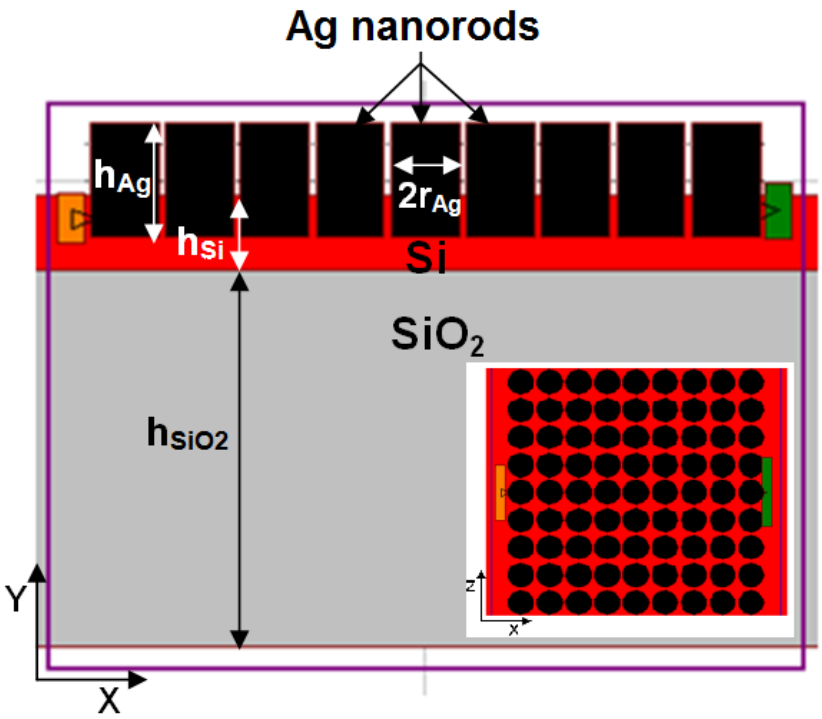

Figure 2.1 Schematic of the basis waveguide cross-section (x-y plane) and top view in inset (x-z plane) of proposed basis waveguide comprising of silver nanorods on silicon on insulator substrate.

Ag nanorods provide lateral confinement within the nano sized low loss Si core in contrast to lossy planar metal structure, arrayed structure offers plasmonic band-gap and the texturing due to base of metal rods yields the required momentum to the propagating plasmon through the waveguide.

SiO_2 as substrate offers vertical confinement also making it compatible for integrated circuitry. The high refractive index core of silicon retains the propagating mode and the plasmonic bandgap assists desired propagation.

Arrayed basis structure exhibits a bandgap in the visible region; and the introduced defect acts as a waveguide exhibiting strong field confinement to the propagating plasmons. Hence the basis geometry can be easily employed to devise various optical components such as couplers, splitters, multiplexers, demultiplexers etc., thereby, opening new possibilities in the ultra-compact plasmonic circuitry design.

The basis structure comprises of arrangement of silver nanorods (with dielectric constant, ε = -13.6089+ i0.995 at 633nm) perpendicularly embedded into silicon-on-insulator substrate to an optimized depth of 50nm in square lattice fashion. The schematic of the basis waveguide cross section(x-y plane) and top view (x-z plane) are shown in Figure 2.1 and its inset respectively. Optimized design parameters and simulation parameters are briefed in the following.

2.2.1 Optimized design parameters

Silver nanorods of radius (r_{Ag}) 45nm, height (h_{Ag}) 150nm and lattice constant a_{Ag}=110 nm are arranged in a square lattice arrangement into silicon layer of refractive index n_{Si} = 3.5 with thickness (h_{Si}) 100nm to a depth of 50nm into it. When depth to which Ag rods are inserted is increased further, it results in leaky mode. SiO_2 layer of refractive index n_{SiO2} = 1.45 with thickness (h_{SiO2}) 500nm is chosen as a substrate. The length of the waveguide is 1µm.

2.2.2 Simulation parameters

In order to obtain the propagation characteristics proposed waveguides, finite difference time domain method is employed. The simulation is performed using perfectly matched layer (PML) boundary conditions with PML width = 500nm along X, Y and Z directions and average grid size of 6.25nm was taken along X and Z- axes whereas, 10nm along the Y-axis. The light wave of wavelength

1550nm is launched into the device perpendicular to the longitudinal axis of the Ag nanorods.

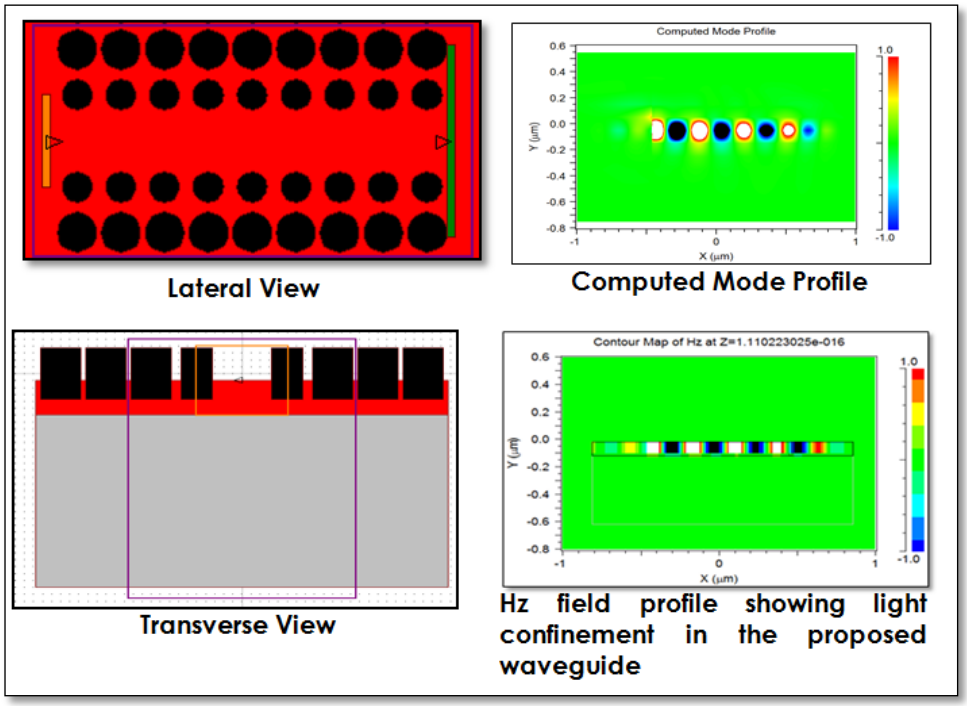

Figure 2.2 Schematic of the plasmonic waveguide designed by introducing defect through the basis structure showing lateral and transverse view and also the mode profile through the defect.

2.2.3 Band gap for the basis structure

Transmission characteristics for the basis structure reveal a bandgap in the visible regime for transverse magnetic polarization. Normalized transmission is obtained for the basis structure is shown in Figure 2.3 which depicts gap within the visible regime and the simulated Ey field profile is represented in the inset of Figure 2.3 indicating the gap offered by the periodic structure.

As the bandgap exhibited by the basis waveguide covers the visible region hence, the device is optimized for 633nm anticipating its vast grounded applications. Introducing defects in the basis forms the waveguides of desired function Thus, the properties of various waveguides and devices based on the

defects introduced in the basis waveguide are discussed below for the input at 633nm.

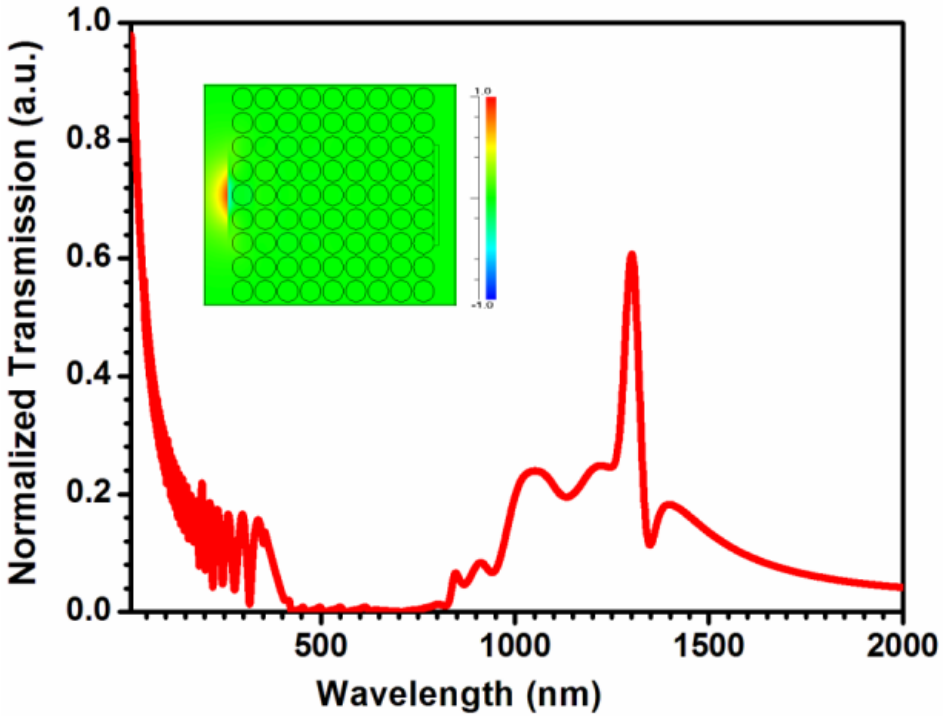

Figure 2.3 Normalized transmission for the basis structure showing bandgap within 400-800nm and the inset shows electric field profile Ey depicting the light is forbidden from propagation.

2.2.4 Defect in basis structure: Waveguide

Waveguides are designed when defects are introduced by breaking the periodicity of the structure as in Figure 2.2 showing lateral and transverse view of the waveguide along with the computed mode profile. It is possible to design plasmonic circuits with silver nanorods embedded into SOI which can carry the em energy through the defect that is the region of silicon fenced by metal rods and having SiO_2 beneath Si. The narrow defect forms the core of the waveguide where the energy propagates. Different types of waveguides derived from the basis are summarized below with important results.

2.3 Realization of plasmonic waveguides: Straight, bend and Y-splitter

2.3.1 Straight waveguide

The basis waveguide is engineered by introducing linear defect, resulting in a straight waveguide, as shown in the inset i_1 of Figure 2.4. Electromagnetic energy traverses through the defect via plasmonic bandgap propagation and the presence of metal nanorods leads to the confinement of this energy within the subwavelength defect.

The textured interface at the base of the nanorods and Si slab leads to the generation of the localized plasmons hence enhancing the input signal.

Further, the inset i_2 in Figure 2.4 illustrates the top view and lateral view of the contour mode profile of electric field (E_y) respectively which depicts that the mode stays within the desired subwavelength linear defect waveguide.

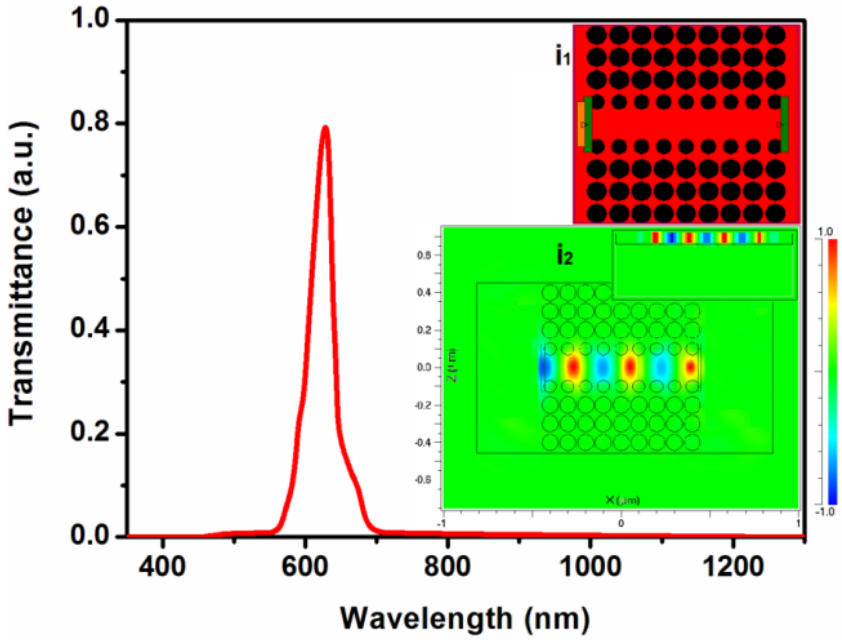

Figure 2.4 Normalized transmission for the proposed straight waveguide showing peak at λ=633nm, schematic of the structure and the Ey field profile in X-Z and X-Y planes are given in the inset.

2.3.2 Bend design

Basis waveguide is further utilized for making bend design through it. An efficient bend design is devised by centrally removing the silver nanorods at right angles. The curve plotted in the Figure 2.5 represents the normalized power transmission, which shows a major peak transmission at wavelength 633 nm along with few smaller peaks.

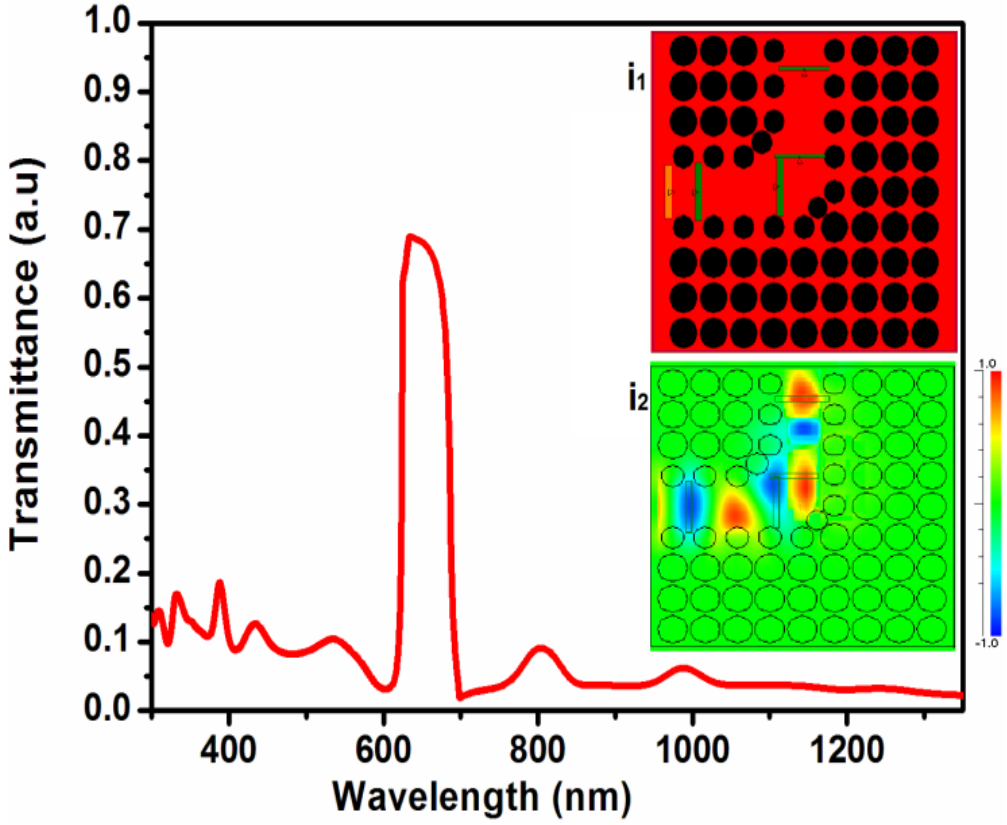

Figure 2.5 Bend waveguide exhibiting the resonating peak at 633nm and the insets show the structure and the Ey field profile depicting how the energy is routing through the bend in the waveguide

The propagating mode is able to take sharp bends with ease. The computed field (E_y) profile obtained on investigation of the bend design appears in inset (i_2) of Figure 2.5, exhibiting confinement of the modal power within the bend waveguide.

2.3.3 Y-splitter

The Y-splitter devised from the basis waveguide consists of y-shaped defect in the basis waveguide. Top view of the splitter is as shown in the inset (i_1) of Figure 2.6. It is found that the introduced defect and its optimization provide easy propagation for 633 nm wavelength. The output power obtained at the end of the individual arms is found to be equal and incident light reaches the monitor at the end of the two arms in same phase. Hence, it can work as 50-50 power splitter. Y-splitter shows confinement of modal power within the defect region of the waveguide. The contour map of the electric field E_y reveal propagating plasmon profile.

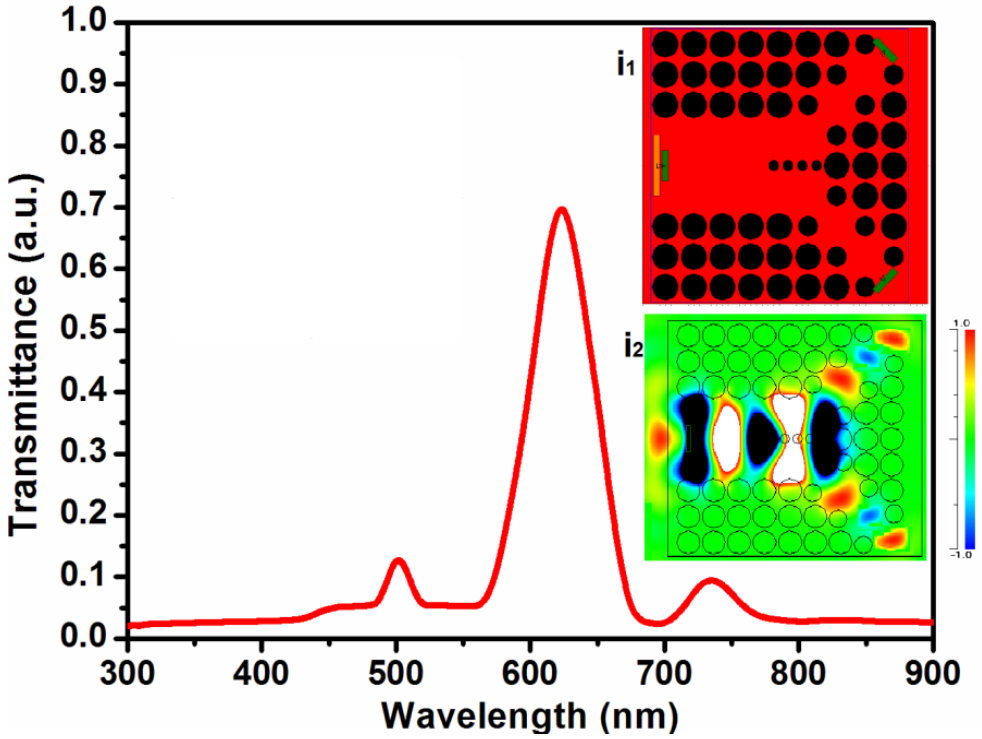

Figure 2.6 Normalized transmission for the proposed Y-splitter with resonating peak at λ=633nm. Schematic and the Ey field profile showing energy splitting into the two arms is given in the inset.

2.3.4 Propagation characteristics of the waveguides

Important results characterizing the proposed waveguides are given below.

2.3.4.1 Normalized power transmittance

The normalized power transmittance for the nano-sized straight waveguide, bend design and y-splitter indicates resonating peak at 633nm as shown in Figure 2.4, 2.5 and 2.6. Transmittance is defined as the fraction of power at output with respect to input.

$$Transmittance = \frac{Power_{output}}{Power_{input}} \quad (2.1)$$

2.3.4.2 Quality factor

The quality factor *Q*, determines the qualitative behaviour of the plasmon resonance through the proposed waveguide. The straight waveguide exhibits a quality factor of 97.5 for λ=633nm which is good in case of plasmonics. The quality factor is calculated using the following relation:

$$Q = \frac{\Delta\lambda}{\lambda} \quad (2.2)$$

where λ is the plasmon wavelength with respect to the resonant frequency at which maxima is obtained and Δλ is the full width at half of maxima. Narrow transmission band width of 10nm is obtained and propagation length of 1micron.

2.3.4.3 Fractional confinement factor

Fractional confinement factor is calculated which shows 92% confinement for the propagating wavelength is for 633nm of the input and is calculated to be less for the rest of the wavelengths validating that the device is tuned for 633nm wavelength. Confinement factor is defined as:

$$Fractional\ confinement\ factor = \frac{Power_{output\ @core}}{Power_{output\ @whole\ waveguide}} \quad (2.3)$$

2.3.4.4 Tolerance

Tolerance limit for various rod parameters are calculated, it comes out to be 5nm in case of rod radii whereas 10nm with respect to height of the rod which makes it to be a very sensitive device as well.

2.3.4.5 Propagation losses

Propagation losses are calculated as loss in dB/μm for all the considered structures and found it to be 0.75dB/μm, 0.89dB/μm and 0.77dB/μm for the straight waveguide, bend waveguide and y-splitter respectively.

2.4 Summary

Embedded design on SOI offers strongly confining geometry which can be utilized well as waveguides. Induced defects in the basis waveguide restricts the mode in nano sized defect and efficiently guide the propagating mode at 633nm with low losses, which can also be tuned for other wavelengths by altering the various waveguide parameters such as, periodicity or radii of rods or the width of the defect. Successful implementation of straight waveguide, bend design and y-splitter affirms possibility of high density plasmonic circuitry. The proposed planar geometry with strong lateral and vertical confinement of the modes renders easy integration with chip circuitry. The investigations provided here validate the use of nano structures for SPP propagation and hence, miniaturize the optical devices for specific applications.

Chapter 3
Plasmonic Mach-Zehnder Interferometer[1, 2]

3.1 Introduction

As discussed in the previous chapter, the periodic arrangement of metal nanoparticles gives rise to the plasmonic band gap allowing plasmonic band gap guidance, further this effect can be utilized in devising plasmonic band gap based sensors. Hence in this chapter a novel design for plasmonic Mach-Zehnder interferometer sensor is described.

It is well established now that plasmonics has gained supremacy over photonics and electronics, by overcoming the diffraction limit [84] and assisting light guidance with deep subwavelength confinement [85]. Therefore it has led to the miniaturization of nanophotonic devices and development of plasmonic sensors by integrating metallic structures with dielectric.

Advent of plasmonics has impressively manipulated the sensing technology up-surging next generation ultra-compact and highly sensitive devices. This is attributed to the intense field at metal-dielectric interface making them extremely sensitive to the local changes.

Sensors are required to detect minute environmental changes especially the ones designed for diagnosing diseases. So, to achieve proficient sensing,

[1] A part of the results reported in this chapter has been used in filing a patent: 'A sensing system and a sensing device for detection of biological materials and method thereof', ***Indian Patent Application*** *No.: 1168/DEL/2013* (2013)

[2] A part of the results reported in this chapter has been published in the paper ''Surface plasmon polariton band gap enabled plasmonic Mach Zehnder interferometer: Design analysis and application', ***Plasmonics***, 9 (3) pp. 527-535 (2014). *http://dx.doi.org/10.1007/s11468-013-9652-5*

combining plasmonics with interferometry like plasmonic Mach-Zehnder interferometer (PMZI) yields synergistic result extending sensitive and accurate method for detection of analyte.

3.1.1 Plasmonic Mach-Zehnder Interferometer

Interferometers allow fast and ultrasensitive detection. Interferometer sensors can specifically and sensitively detect at very low concentrations [86], can measure small displacements refractive index changes, surface irregularities etc.

Mach-Zehnder interferometer determines relative phase changes between two beams derived by splitting of light from a single source. They are suitable for precise measurements of small changes over a wide range of refractive indices [87] and have applications as chemical and biosensors.

To improvise sensing efficiency, interferometers are involved with Mach-Zehnder geometry (Figure 3.1) which offers profound method to inspect molecular response. Their response is further enhanced by employing plasmonics: in making sensors [88, 89], for determination of phase, to calculate electron density etc.

So, the synergy of plasmonics into interferometry extends accurate method for detection and enhances sensitivity by incorporation of metallic structures [90-92].

Metal nanostructures can be arranged to yield Mach-Zehnder interferometer and their periodic arrangement can allow easy wave-guidance through surface plasmon polariton (SPP) band gap effect [93]. Although thin metallic films can also be employed but films can lead to resistive losses [92, 94], therefore metallic nanostructures have specifically received considerable attention [95] especially for designing sensors. A rewarding application will be to design sensors for diagnosing and classifying different cancer cell lines.

Figure 3.1 Plasmonic Mach-Zehnder interferometer (PMZI) has the synergy of both the plasmonics and interferometry

3.1.2 Surface plasmon polariton band gap

To draw benefits from their plasmonic properties, metal structures of controlled size and shape at nanoscale are integrated with dielectric to get the desired results which enables tailoring the peak resonance, enhances electromagnetic field, improves sensitivity, transmission, imaging properties etc. When surface plasmon polaritons are excited at nanostructured metal-film structures it is observed that SPPs get reflected from the periodic arrangement where as they get guided along the introduced defect [93] thereby demonstrating surface plasmon polariton band gap (SPPBG) effect.

Plasmon propagation and waveguiding is not only restricted to the planar interfaces but can also be efficiently controlled by plasmonic band gap effect arising due to periodic arrangement of metallic nanostructures [93, 96]. Periodic arrangement of MNPs exhibits surface plasmon polariton band gap effect. The motivation for SPPBG structures arises from photonic band gap structures which allow lossless waveguiding even around sharp corners.

Thus an obvious employment is to realize SPPBG structures, leading to ultra-compact and highly sensitive devices which can be efficiently achieved by exploiting metallic array of nanorods. Defect in SPPBG structures can trap and guide plasmons having frequencies that fall within the gap region by SPPBG effect.

By tailoring the size of MNPs, the SPPBG effect yields control over plasmonic band gap region and consequently over plasmon propagation, to get

desired properties with promising applications in nanoscale signal routing, waveguiding, miniaturization of integrated circuitry, extraordinary light transmission, sensing etc. and out of these, sensing has unrivalled importance.

Cancer cells have higher refractive index (RI) than the normal cells [97-99]. Identifying this RI difference help in quantitative analysis of malignant cells, because increased RI points to cell anomaly. RI of living cells can be measured by various approaches [97-98, 100-101], but sensing RI difference accurately is important, mainly because numerous biological substances can be identified and detected through sensing the variation in RI.

Plasmonic sensors have effectively replaced traditional RI sensors due to extremely responsive interaction of SPP field with the analyte [102-103]. A novel design of SPPBG based plasmonic Mach-Zehnder interferometer sensor is discussed in the next section.

3.2 PMZI sensor design and structural parameters

Similar to the basis mentioned in chapter 2, section 2.2, the proposed design for PMZI (Figure 3.2) incorporates Ag nanorods embedded into silicon-on-insulator to a depth of 50nm deep inside the substrate. Ag nanorods encompass higher refractive indexed silicon, forming the fortified core (inset Figure 3.2) for plasmon mode propagation. PMZI is formed by introducing defects in the basis as shown below in Figure 3.2.

Structural parameters optimized for the Ag nanorods (dielectric constant, ε = -13.6089 + i0.9950 at 633nm) are: radius, R_{Ag}=45nm, height, h_{Ag}=150nm, embedded vertically into SOI (Si thickness, h_{Si}=100nm and SiO_2 thickness, h_{SiO2}=500nm) with lattice constant A=110nm. Optimized parameters for PMZI are: width W_0=330nm, length L_0 = 330nm, arm-length L=550nm, arm-width W=110nm, bend angle b=45° and bend length B=155nm. These parameters concede successful execution of plasmon interference in our PMZI sensor and facilitate its functioning for the input of 633nm.

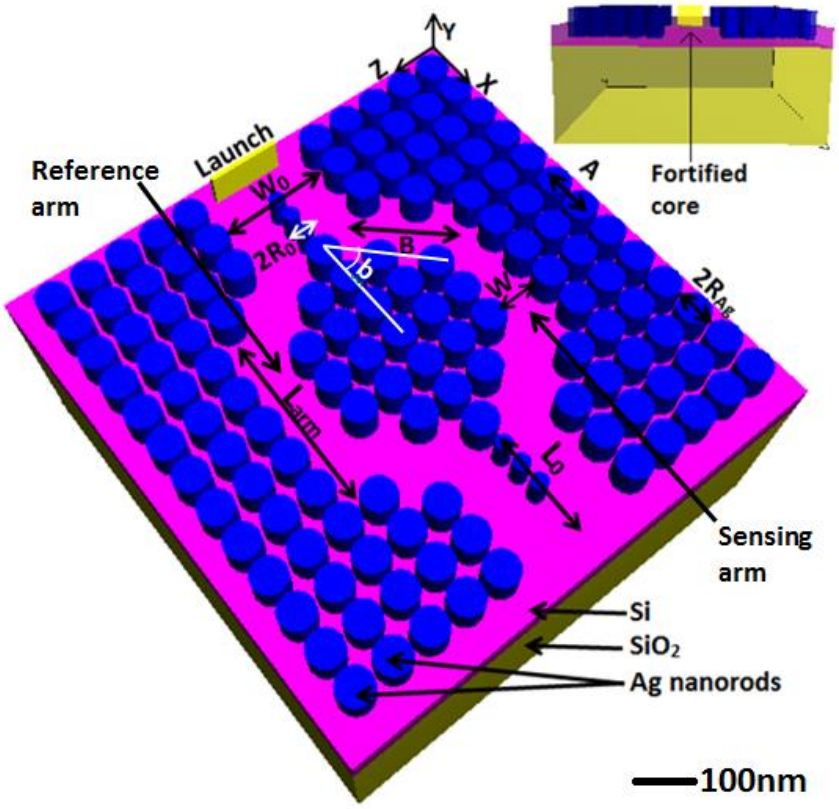

Figure 3.2 Schematic of the proposed PMZI sensor having Ag nanorods array vertically embedded into SOI in square lattice arrangement, inset shows the fortified core formed by Ag rods encompassing high refractive index Si for plasmon propagation

3.2.1 Working principle

The proposed plasmonic Mach-Zehnder interferometer detects refractive index changes at the sensing arm corresponding to the respective analyte refractive index used, with respect to the analyte-free reference arm via plasmon-analyte interaction.

3.2.2 Advantages of the proposed structure

1) Arrayed Ag nanorods grant local field enhancement readily available for interaction with the sample resulting in improved sensitivity and it also offers plasmonic band-gap, assisting plasmon guidance through the defect with minimal losses.

2) Use of nanorods renders strong lateral confinement to the resultant mode in the fortified core, whereas high contrasting refractive index substrate contributes transverse confinement.
3) Horizontal arrangement of nanorods adds complexity to sensing application, thus leveled platform (defect site) used in the proposed PMZI provides ease for placing analyte.
4) Also, the proposed geometry allows easy drawing of any defect shape required for waveguidance and can be uniformly fabricated using nanoimprint lithography based approach for the fabrication of large area, uniformly oriented plasmonic arrays [104-106].

3.2.3 Plasmon propagation through PMZI: SPPBG assistance

Proposed PMZI demonstrate plasmon propagation through it with the assistance of SPPBG effect. It is observed that the optimized parameters result in constructive interference at the output (see Figure 3.3) hence assuring excellent working of the PMZI.

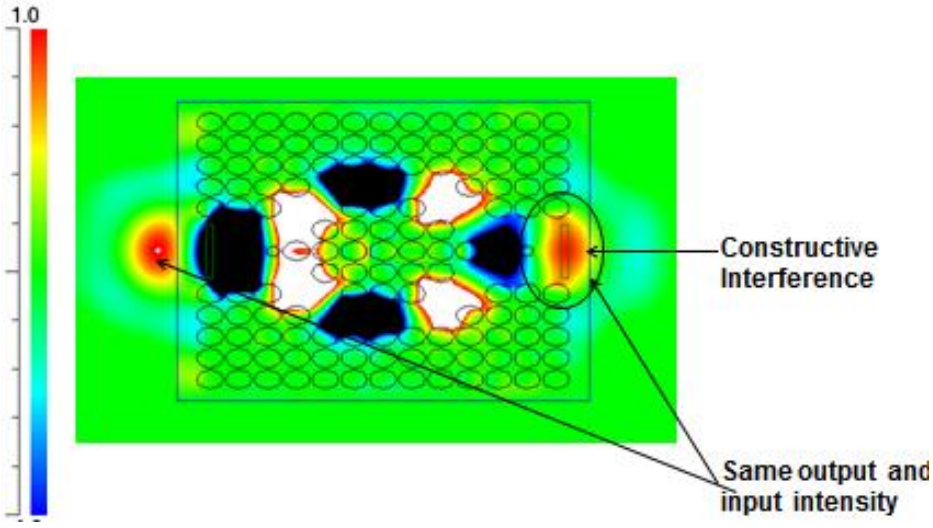

Figure 3.3 Demonstration of plasmon propagation through the plasmonic Mach-Zehnder interferometer showing constructive interference at the output ensuring excellent performance of the device.

The basis structure exhibits surface plasmon polariton band gap for the wavelength region of 400nm-800nm shown as Band 1 in Fig 3.4 for transverse magnetic (TM) plasmon mode, using plane wave expansion method.

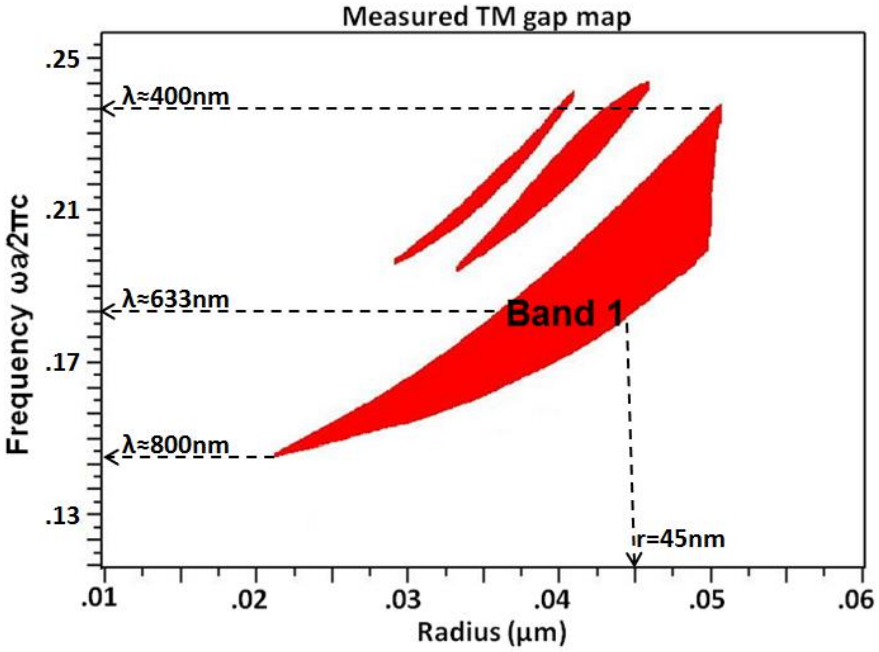

Figure 3.4 Transverse magnetic gap map (400nm-800nm) obtained for the base structure.

Measured TM gap map reveals the optimized value for the input frequency and the rod radius obtained from largest gap region and is marked in Fig 3.4. Gap ascertains the approximate input wavelength falling within the band gap regime (≈400nm-800nm) which can be used for our structure for the optimized parameter. Introducing a defect in the base structure allows light propagation for the wavelength which lies within the band gap region, obtained for the structure. The section below confers some important results obtained for the PMZI.

3.3 Results

3.3.1 Working wavelength for the device

Propagation characteristics for the proposed PMZI are obtained using FDTD (with PML width=500nm along the x, y and z directions) method by scanning the

device for the wavelength input ranging from 200nm-1000nm (Figure 3.5). Electric field Ey profile obtained for the device presented in Figure 3.5 demonstrate plasmon propagation for the PMZI indicating perfect propagation for λ= 633nm.

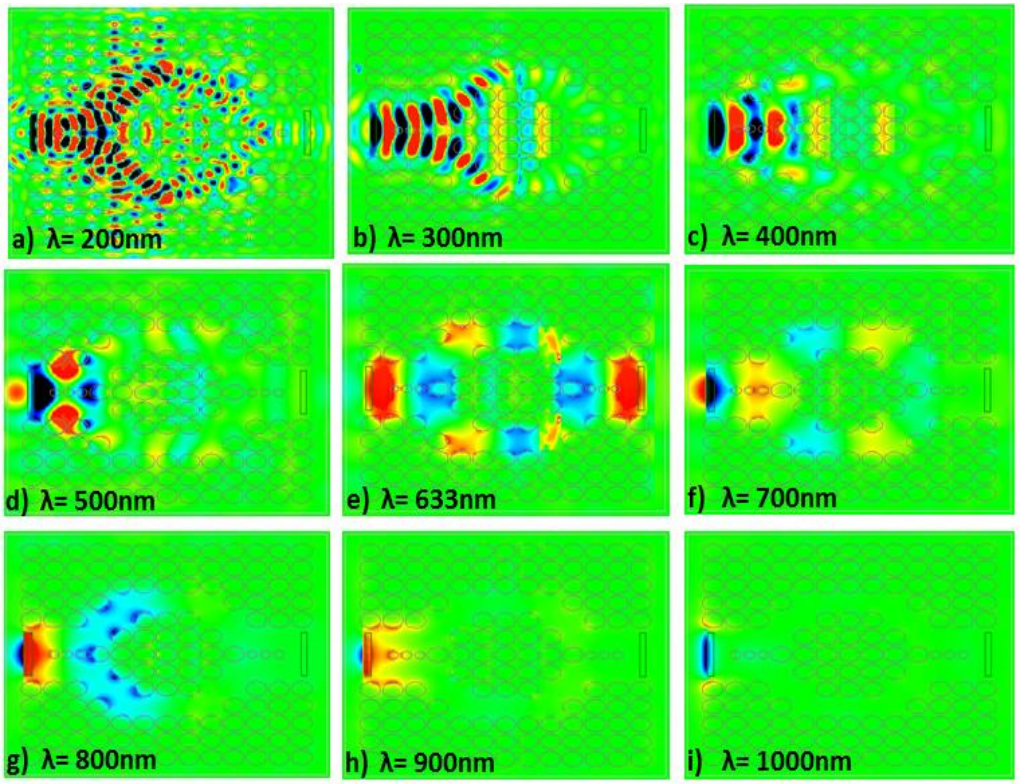

Figure 3.5 Electric field profile obtained for the device demonstrating plasmon propagation for the PMZI indicating perfect propagation for λ= 633nm

Three dimensional (3D) contour plot of the field distribution of plasmon propagation through the device is also obtained, distinctly representing the intensity of the traversing wavelength and is given in Fig 3.6 (a), (b) and (c). 3D plots in Fig 3.6 demonstrate the functioning of PMZI for input wavelengths: λ= 200nm, 633nm and 900nm exhibiting plasmon interference at λ=633. These observations verify the plasmonic band gap region, which assist the plasmon propagation through the defect, imparting strong spatial confinement.

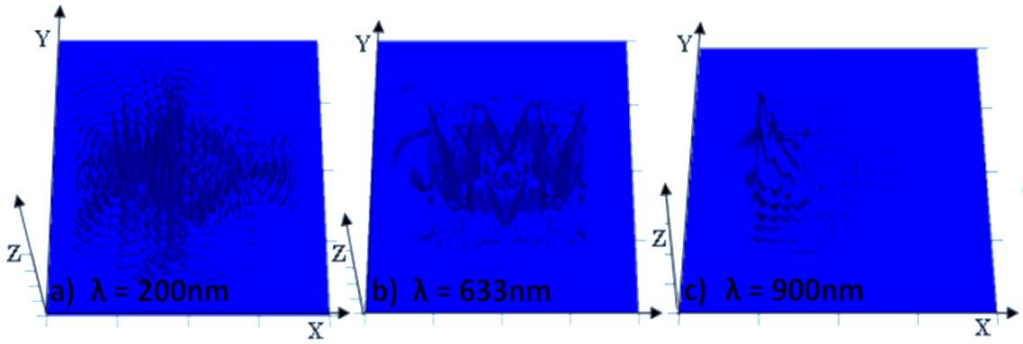

Figure 3.6 (a), (b) and (c) Three dimensional (3D) contour plot of the field distribution of plasmon propagation through the device demonstrating its functioning for inputs λ= 200nm, 633nm and 900nm exhibiting constructive plasmon interference at λ=633 obtained for the optimized parameters of PMZI.

For λ=633nm the proposed PMZI show a well-defined interference pattern, Fig 3.6(b), allowing accurate measurement of wave parameters unlike other inputs. The input plasmon field intensity split equally into the reference and sensing arms of the interferometer, the plasmons propagate therein the arms and then interfere again constructively at the output end, maintaining the resultant amplitude equal to as that at the input end.

3.3.2 Analyte: cancer cells

After optimizing the parameters of the device, it is employed for sensing. Five different cell lines considered for detection are Jurkat (blood/bone marrow cancer cell), HeLa (cervical cancer cell), PC 12 (adrenal gland cancer cell), MDA MB 231(breast cancer cell) and MCF 7 (human breast adenocarcinoma cell). Refractive indices of these malignant cells have been determined by Liang et al. [107]. The refractive index values of these cancer cell lines have been incorporated in the devised plasmonic Mach-Zehnder interferometer for detection as summarized in Table 3.1.

Table 3.1 Calculated values of wavelength shifts Δ λ, sensitivity S, FWHM δ λ and figure of merit FOM obtained for various cancer cell lines

Table 1: Calculated values of wavelength shifts Δ λ, sensitivity S, FWHM δ λ and figure of merit FOM obtained for various cancer cell lines													
Cancer cell line	n	$\Delta\lambda_1$ (nm)	$\Delta\lambda_2$ (nm)	$\Delta\lambda_3$ (nm)	S_1 (nm/RIU)	S_2 (nm/RIU)	S_3 (nm/RIU)	$\delta\lambda_1$ (nm)	$\delta\lambda_2$ (nm)	$\delta\lambda_3$ (nm)	FOM_1	FOM_2	FOM_3
Jurkat	1.390	4.142	6.796	2.462	2071	3398	1231	20	16	18	103.55	212.37	68.38
HeLa	1.392	5.730	8.300	3.900	2865	4150	1950	22	16	20	130.22	259.36	97.50
PC 12	1.395	10.146	14.010	7.560	3382	4670	2520	30	20	22	112.73	233.50	114.54
MDA	1.399	16.160	20.052	12.404	4040	5013	3101	22	12	22	183.63	417.75	140.95
MCF 7	1.401	10.022	11.356	8.242	5011	5678	4121	24	12	22	208.79	473.16	187.31

3.3.3 Refractive index sensing

From the electric field profile shown in Figure 3.7 it can be seen that the presence of analyte in sensing arm changes the refractive index of the environment and thus the output of the device noticeably unlike the output when there is no analyte in the sensing arm as shown in Figure 3.3.

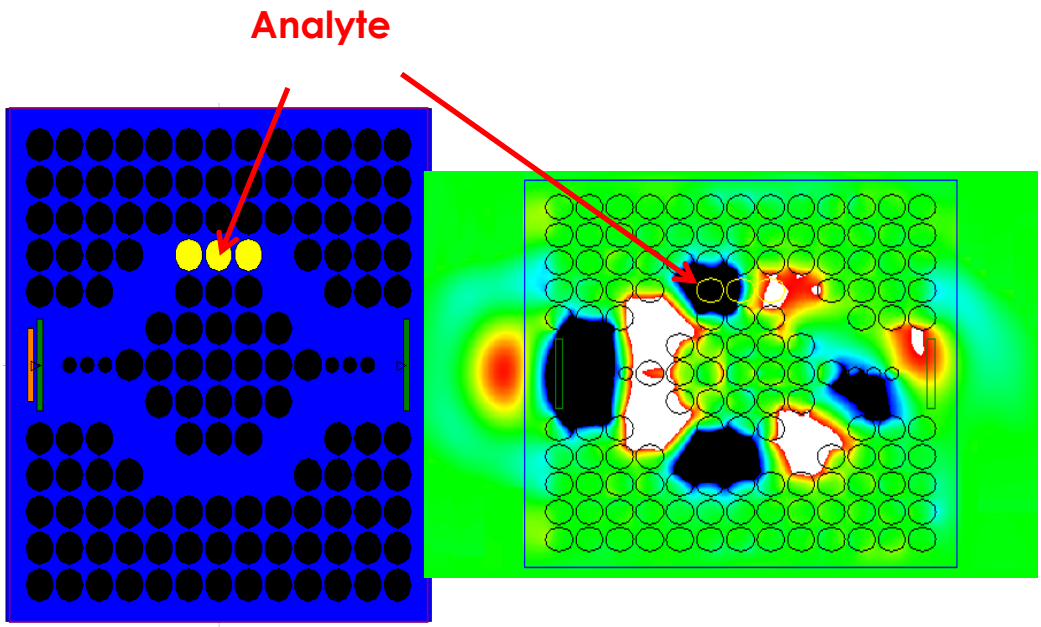

Figure 3.7 Presence of analyte in sensing arm significantly changes the output of the plasmonic Mach-Zehnder interferometer

3.3.4 Spectral analysis

Transmission characteristics are obtained for various cancer cells mentioned in the table above that is Jurkat, HeLa, PC 12, MDA MB 231 and MCF 7 with the input wavelength of λ_1 = 615nm, λ_2 = 633nm and λ_3 = 650nm [Table 3.1] of the visible regime that falls under the allowed frequencies that can traverse through the interferometer and is given in Fig. 3.8 (a), (b) and (c) respectively for the considered wavelengths.

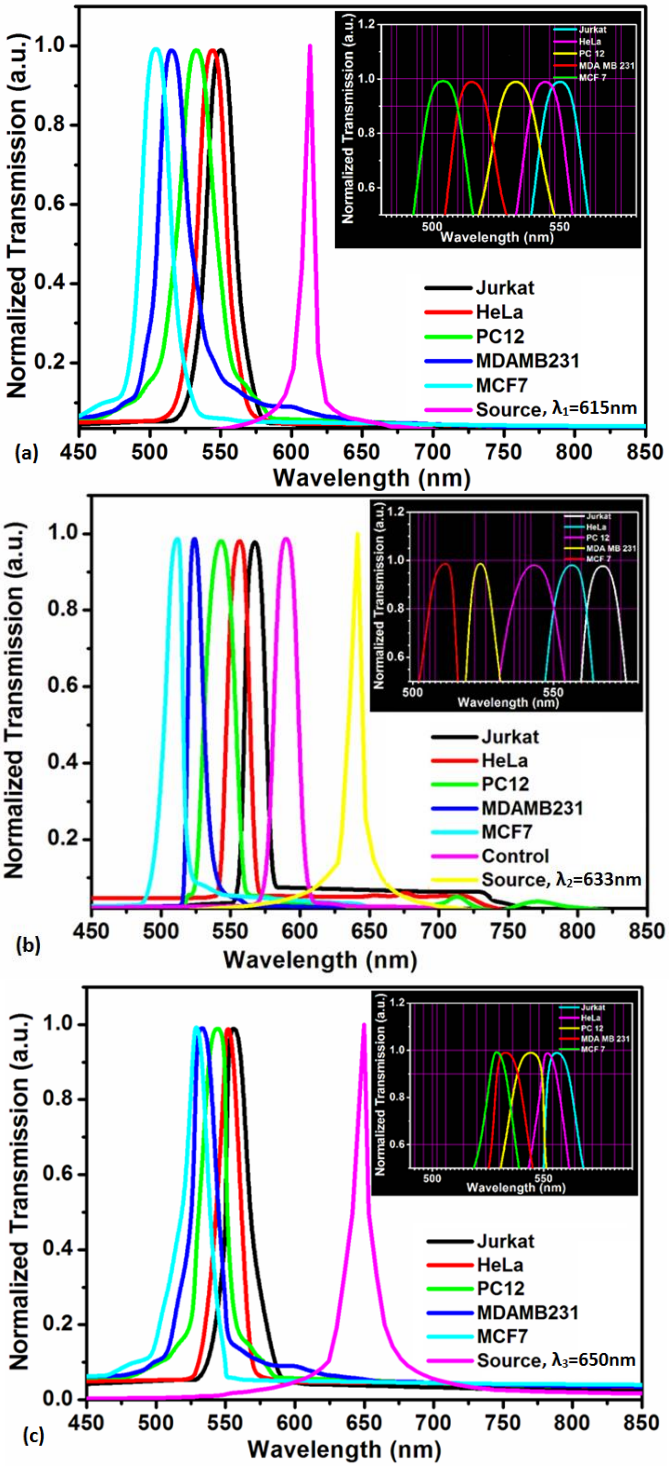

Figure 3.8 (a), (b) and (c) Normalized transmission obtained for different carcinoma cell lines representing blue shift with increasing RI for operational wavelength λ_1, λ_2 and λ_3 respectively.

Sharp distinct peaks are obtained for different kinds of cancerous cell lines. Increase in refractive index results in blue shift of the spectral lines in each case. The insets in each case in Fig. 3.8 (a), (b) and (c) show expanded scale for finer observations. Noticeable spectral shift is achieved and these important observations are tabulated in Table 3.1 under the columns mentioned as $\Delta\lambda_1$, $\Delta\lambda_2$ and $\Delta\lambda_3$ for the input wavelength of λ_1, λ_2 and λ_3 respectively.

3.3.5 Sensitivity

It is observed that remarkable shift is perceived in case of input wavelength λ_2 = 633nm, yielding maximum wavelength shift making it most suitable operational wavelength for sensing using this PMZI. Spectral sensitivity interrogation is done and determined by using equation 3.1:

$$S = \left|\frac{\Delta\lambda}{\Delta n}\right| \qquad (3.1)$$

where, $\Delta\lambda$ represent shift in wavelength and Δn is change in refractive index. The calculated sensitivities for λ_1, λ_2 and λ_3 are tabulated in Table 3.1.

Plot of sensitivity in logarithmic scale against refractive index is drawn and is given in Figure 3.9 which marks the maximum and minimum value of sensitivity obtained for each input wavelength illustrating that maximum sensitivity S_{max}= 5678nm/RIU, is obtained for breast cancer cell line MCF 7 and minimum sensitivity S_{min}=3398nm/RIU is acquired for blood cancer cell line Jurkat with input wavelength λ_2.

Their digital micrograph representing high density of cell content which causes augmentation of refractive index is given in Fig 3.10 (a) and (b) for breast and blood cancer cell lines respectively. The device efficiently senses the change in refractive index of the order of 10^{-3}.

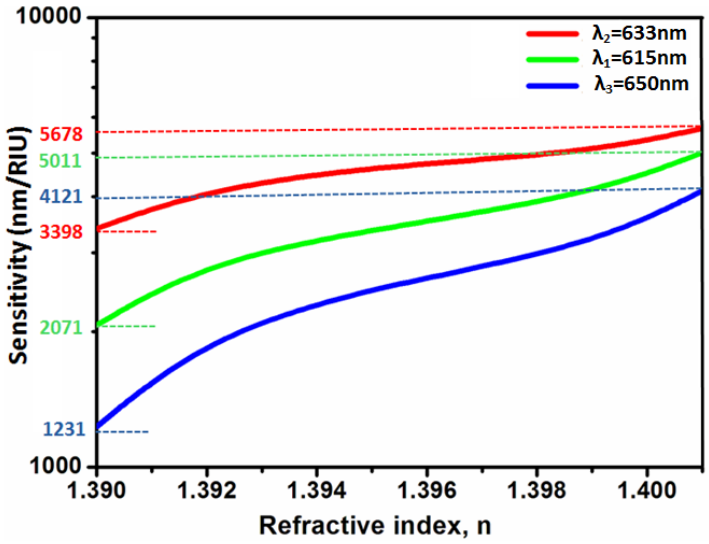

Figure 3.9 Logarithmic variation of sensitivity of the device with respect to the change in refractive index of the cancer cells.

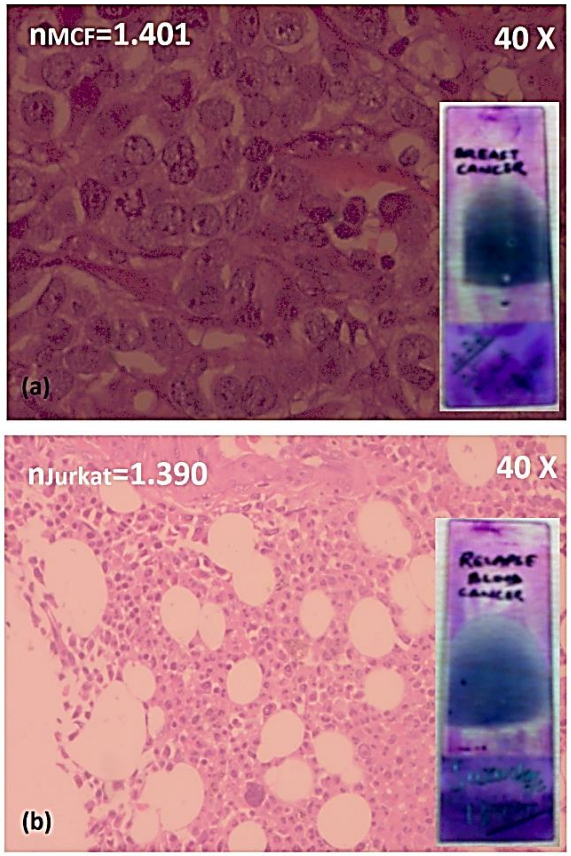

Figure 3.10 (a) and (b): Cancer cell line micrographs of breast and blood cells representing dense cell constituents causing augmentation of refractive index

3.3.6 Figure of merit

Figure of merit (FOM) is calculated to determine the device performance using equation 3.2 mentioned below:

$$FOM = \frac{S}{\delta\lambda} \tag{3.2}$$

where, S is the sensitivity and δλ is the full width at half-maximum (FWHM) of the respective sensing peak. The FWHM values for each cell line are measured from their spectral response and are stated in Table 3.1 as $\delta\lambda_1$, $\delta\lambda_2$ and $\delta\lambda_3$ for input wavelengths λ_1, λ_2 and λ_3 respectively. It is found that highest value of FOM obtained is 473 for operational wavelength λ_2.

3.3.7 Volumetric analysis

Volumetric analysis of the proposed PMZI is done to fix the analyte volume to examine the operation of the device with changing volume. Three different analyte volumes V_1, V_2 and V_3 are considered for MCF 7 as summarized in Table 3.2.

Table 3.2 Volumetric analysis of the sensor

Table 2: Volumetric analysis of the sensor			
	Analyte Volume 10^{-15}cc	Path Difference (μm)	Phase Difference (radian)
V_1	0.95	0.124	1.231
V_2	1.90	0.153	1.518
V_3	2.86	0.190	1.886

Electric field Ey profiles of the propagating mode through the PMZI are obtained for different environmental conditions and displayed in Figure 3.11. It represents Ey field profile with no analyte volume (V_0) in the sensing arm

validating that the similar environmental conditions in the two arms of the PMZI causes centrally located field profile at the output end. It is observed that as the presence of analyte volume increases from volumes V_1 ($0.95*10^{-15}$cc) to V_3 ($2.86*10^{-15}$cc) in the sensing arm, the output of the PMZI appears shifted and distorted (see Fig 3.11 (b), (c) and (d)) with maximum distortion in case of V_3 owing to the maximum plasmon-analyte interaction in the sensing arm of PMZI resulting in path difference acquired between the two arms. Path difference for each volume is calculated and is tabulated in Table 3.2, which is further used to calculate the phase difference obtained in each case.

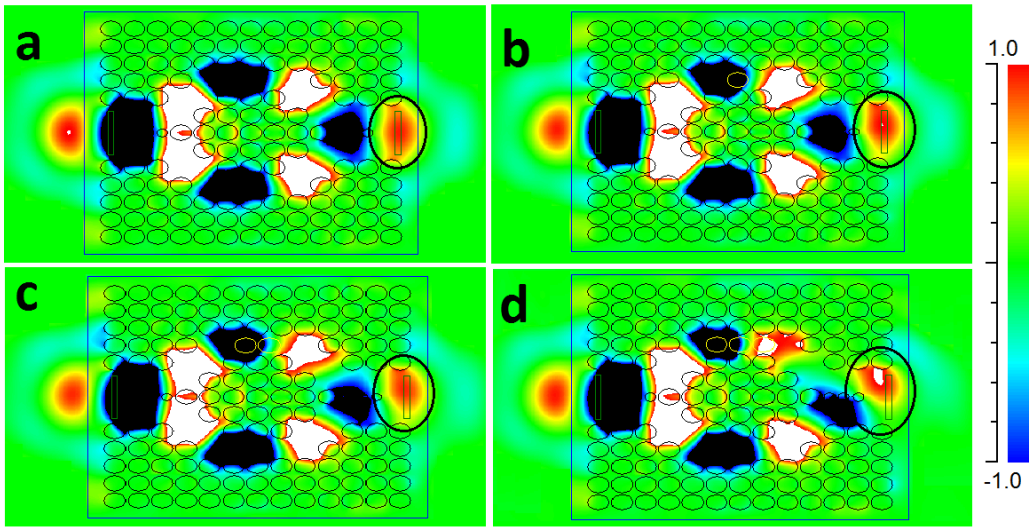

Figure 3.11 Electric field profile of propagating mode through the PMZI with no analyte in the sensing arm i.e. similar environmental condition in the two arms of the PMZI showing the centrally located field profile at the output end. (b), (c) and (d) Represent the effect of increasing analyte volume as V_1, V_2 and V_3 respectively, on the field profile at the output, showing plasmon-analyte interaction.

3.3.8 Phase shift

Fixing analyte volume to V_1 the phase shift is obtained with respect to various cell lines. For this, power is obtained at the output and plotted against time scale converted into distance. Its graphical representation is given in Figure 3.12 (a) with the expanded scale in its inset. Power is examined and path difference is

measured to further calculate the phase shifts as the RI of the cell changes, this variation is exposed in Figure 3.12 (b). Significant phase shift is observed providing a useful scale for RI detection and hence cancer cell differentiation can be easily done. These observations are summarized in Table 3.3 describing that maximum phase shift of 1.2357 in radian (~71°) is observed for MCF 7 cell line establishing it as a highly sensitive ultra-compact yet simple device for disease diagnosis.

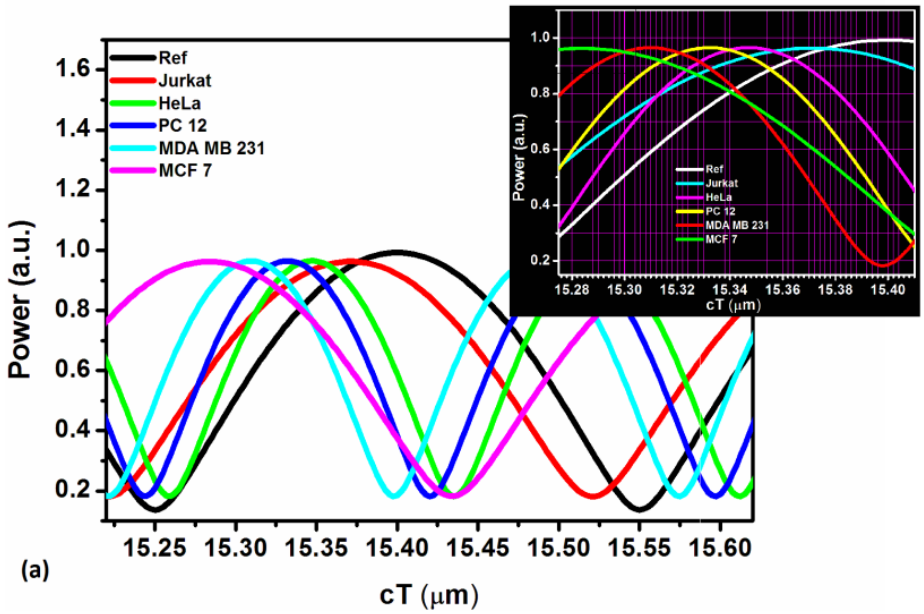

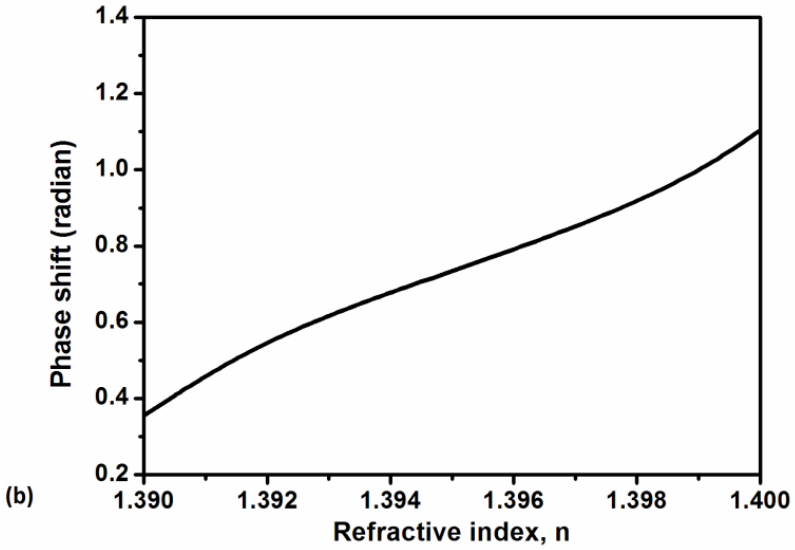

Figure 3.12 (a) Variation of power at the output through the span of time. Inset show expanded scale for measuring the shifts. (b) Plot of phase shift with refractive index showing significant change yielding easy detection of carcinoma cell lines

Table 3.3 Path difference and phase difference obtained for different cancer cell lines

Table 3: Path difference and phase difference obtained for different cancer cell lines			
Cancer cell line	**Refractive Index n**	**Path difference (μm)**	**Phase shift (radian)**
Jurkat	**1.390**	**0.0337**	**0.3351**
HeLa	**1.392**	**0.0569**	**0.5655**
PC 12	**1.395**	**0.0739**	**0.7336**
MDA MB 231	**1.399**	**0.0970**	**0.9634**
MCF 7	**1.401**	**0.1244**	**1.2357**

3.4 Summary

As the diffraction limit restricts miniaturization of conventional photonic devices, the proposed miniaturized plasmonic Mach-Zehnder interferometer detects various types of cancer cell lines with high sensitivity using SPPBG effect for waveguidance. The peculiarity of the work is that it innovatively offers an ultra-compact highly sensitive novel device for sensing and overcomes the size limitations of the prism based SPR sensors. Periodic arrangement of metal nanorods offers plasmonic band gap assisting sub-wavelength confinement of the resultant mode through the defect. Outstanding figure of merit is achieved verifying the device performance. Volumetric analysis is carried out that express low analyte volume is sufficient to yield noticeable phase shift which indicate the proficiency of the proposed PMZI. Thus the proposed PMZI sensor implemented for classification of cancer cells makes this miniaturized device a promising candidate for practical application in the general areas of sensors and actuators, greatly improving disease diagnosis by combining plasmonics with interferometry.

Chapter 4
Enhanced Fano resonance in silver ellipsoidal plasmonic crystal cavity[1]

4.1 Introduction

In the previous two chapters it was the propagation characteristics of the metal nanoparticles based waveguide assisted by plasmonic band gap guidance that has led to the realization of various devices yet another important effect of metal nanoparticles is the local field enhancement which results highly amplified output. For closely spaced metal nanoparticles these enhanced fields can sum up and at resonance it can yield ultra-high transmission. And when the back scattering from these metal nanoparticles become appreciable the resonance curve obtained features asymmetry and is called Fano resonance. A brief introduction to Fano resonance and its analogy with resonance is described below.

4.1.1 Resonance

For an oscillating system, resonance is the tendency to oscillate with greater amplitude at some specific frequency called resonant frequency. The response of an oscillating system which is driven by external frequency ω is obtained about its resonant frequency ω_0 and is *symmetric* (for ideal case) as shown in Figure 4.1. The intensity I for such a system is approximated by universally accepted well-known Lorentzian function about its resonant frequency ω_0:

$$\boldsymbol{I(\omega)} \propto \frac{\left(\frac{\gamma}{2}\right)^2}{(\omega-\omega_0)^2+\left(\frac{\gamma}{2}\right)^2} \qquad (4.1.a)$$

[1] A part of the results reported in this chapter has been published in the paper, "Enhanced Fano resonance in silver ellipsoidal plasmonic crystal cavity', ***Journal of Applied Physics***, 114, pp. 234305. http://dx.doi.org/10.1063/1.4851775

where γ is the width of the resonance, which is dependent on damping.

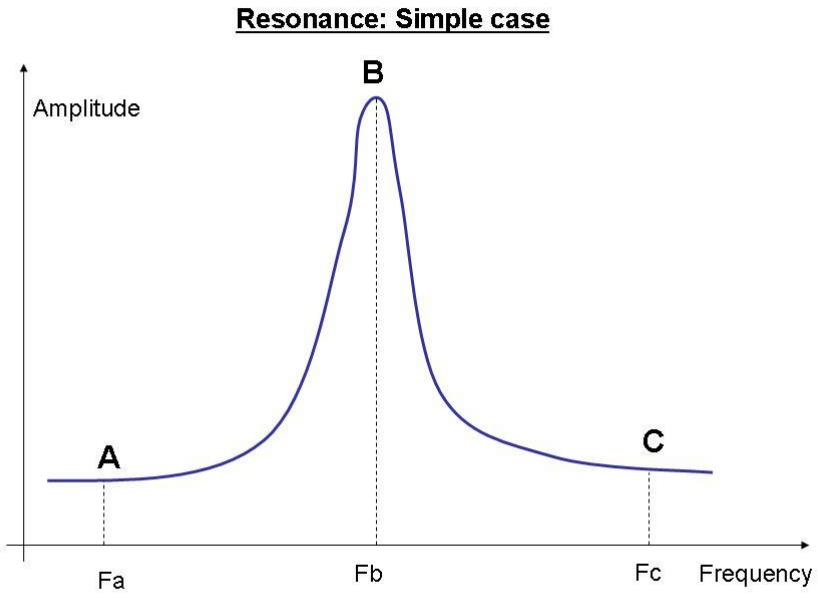

Figure 4.1 Simple representation of resonance phenomenon where the system exhibits resonance at frequency *Fb* having greater amplitude at point B, unlike frequency at point A and C.

4.1.2 Fano resonance

Fano resonance is a resonant scattering phenomenon that gives rise to an *asymmetric* resonance line shapes due to the interaction of discrete excited states of a system with its continuum excited states sharing same energy level. It was discovered by Ugo Fano [108]. In contrast to Lorentzian resonance, the Fano resonance exhibits a distinctly asymmetric shape (see Figure 4.2) having the following functional form:

$$\boldsymbol{I} \propto \frac{(\boldsymbol{F\gamma+\omega-\omega_0})^2}{(\boldsymbol{\omega-\omega_0})^2+\boldsymbol{\gamma^2}} \qquad (4.1.b)$$

where ω is the external frequency, ω_0 is the resonant frequency that is the position of resonance, γ is the width of the resonance and F is Fano parameter which describes the degree of asymmetry [109].

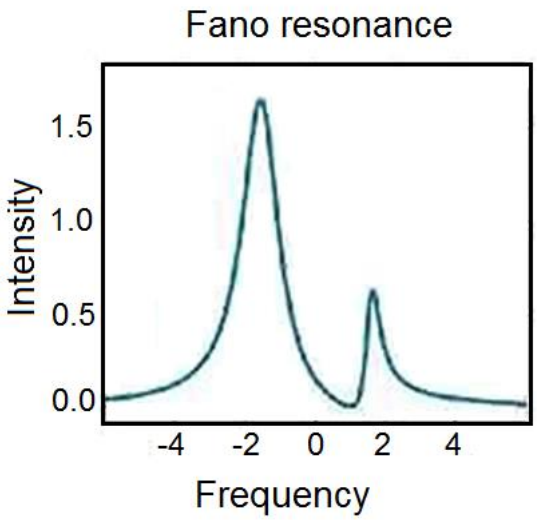

[2]

Figure 4.2 Asymmetric resonance shape is the defining characteristic of Fano resonance.

Fano resonance is generally specific to quantum systems that involve auto-ionization of atoms due to interference of excited leaky modes with incoming continuum radiation that is it couples the discrete bound state to the degenerate continuum of states. This interference (or auto-ionization) gives rise to asymmetric profile characteristics of the Fano resonance. Fano obtained a formula for the shape of the resonance profile of scattering cross section:

$$\boldsymbol{\sigma} = \frac{(\boldsymbol{\varepsilon}+\boldsymbol{q})^2}{\boldsymbol{\varepsilon}^2+\mathbf{1}} \qquad (4.2)$$

where q is the asymmetry parameter and ε is the reduced energy [110]. Formula given in 4.3 suggests that there are exactly one maximum and one minimum in the Fano profile as given below:

- $\sigma_{min}= 0$, at $\varepsilon=-q$
- $\sigma_{max}= 1+q^2$, at $\varepsilon=1/q$

The asymmetry parameter q is *ratio* of transition probabilities to the mixed state and to the continuum and give rise to the following cases (Figure

[2] Image courtesy: http://www.doctorlighthouse.com/fanoresonances.html

4.3):

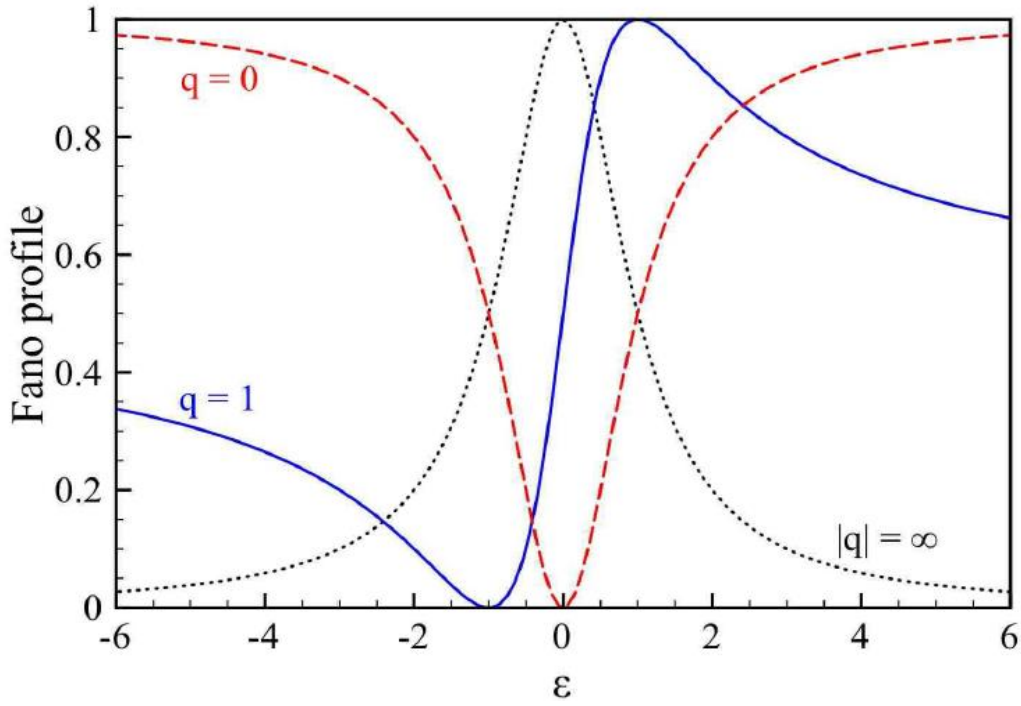

[3]

Figure 4.3 Fano resonance shape depending upon the asymmetry parameter q.

- Case 1 : when $|q| \rightarrow \infty$:
  - Transition to the continuum is very weak
  - Line shape is determined by transition through discrete states only and yields Lorentzian profile shown as dotted curve in Figure 4.3

- Case2 : when $q \approx 1$:
  - Then both the continuum and discrete transition are of the same strength
  - This results in asymmetric profile shown as solid curve in Figure 4.3

- Case 3 : when q=0:
  - This is very unique to Fano resonance
  - It describes a symmetrical dip marked as dashed curve in the Figure 4.3

[3] Image credit: http://journals.aps.org/rmp/abstract/10.1103/RevModPhys.82.2257

By using the comprehensive approach developed by Fano, it is possible to predict the position as well as the width of the Fano resonance [109, 110].

An important feature of Fano resonance is the possibility of destructive interference that leads to asymmetric line shape and its applications are mentioned next.

4.1.3 Applications

As this unique resonance arises from the interference between two or more oscillators, the system has intrinsic sensitivity towards local changes [109], making it well suited for application in chemical and biological sensors. Large shifts in the resonance frequency of the system are the basis of its sensing capability.

The characteristic Fano resonance profile also has promising applications in lasing, switching, slow-light devices, and plasmon-induced transparency. To realize these prospective applications, novel plasmonic designs with improved properties are required, for example, with respect to transmission, propagation and loss characteristics.

4.1.4 Fano resonance in metal nanoparticles

Metal nanoparticles support strong Fano resonance arising owing to the interference between the superradiant bright mode and the subradiant dark mode of the quantum system, which can be designed to achieve the desired optical response. The electromagnetic interactions within such a quantum system influence the line shape of the resultant plasmonic Fano profile. Plasmonic dimers, dolmen structures, metallic double gratings, quadrumers, and heptamers with different cross-sectional areas exhibit Fano resonance, which can be manipulated by tailoring the number and position of the monomeric units [111-114].

However, in simpler clusters like dimers and trimers, the electric dipole resonance subdues the Fano resonance. This limitation is addressed by adding structural complexity or breaking the symmetry to induce bright and dark modes available for interaction to produce Fano resonance [115].

Fano behavior of plasmonic crystal cavity formed in silver ellipsoidal nanoparticles and its cylindrical counterpart are explored and are described in the next few sections.

4.2 Silver ellipsoidal and cylindrical plasmonic crystal cavity

Hexagonally-arranged prolate silver ellipsoids with axes $a = b = 130$ nm, and $c = 500$ nm (with a dielectric constant $\varepsilon = \varepsilon_i + i\varepsilon_r = -110.143+8.807i$, corresponding to the input wavelength of 1600 nm) form the plasmonic crystal having periodicity of 400nm. The background index (n) is 1 and ε varies with the wavelength as shown in Figure 4.4.

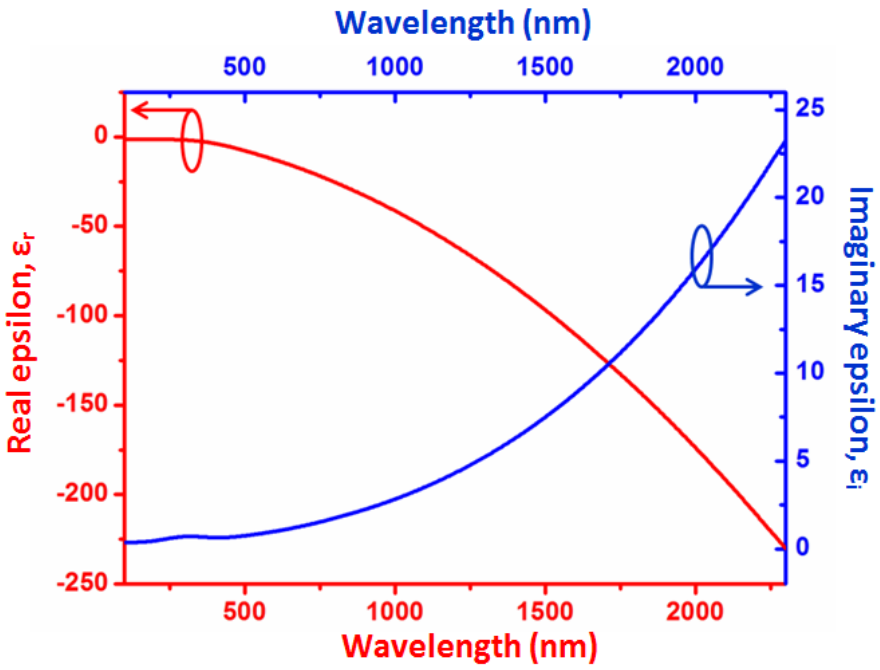

Figure 4.4 Variation of real and imaginary part of dielectric constant of silver with wavelength.

The ellipsoids are arranged to have a semi-axis *c* oriented along the vertical plane of the cavity (by removing an ellipsoid) located at the center of the plasmonic crystal (see Figure 4.5 (a)). This arrangement increases the coherent electromagnetic coupling within the particles that interferes destructively with the cavity mode resulting in Fano resonance. Large cluster results in dark modes that intensify the Fano resonance [112]. Similarly, cylindrical particles form silver cylindrical plasmonic crystal cavity as shown in Figure 4.5 (b)

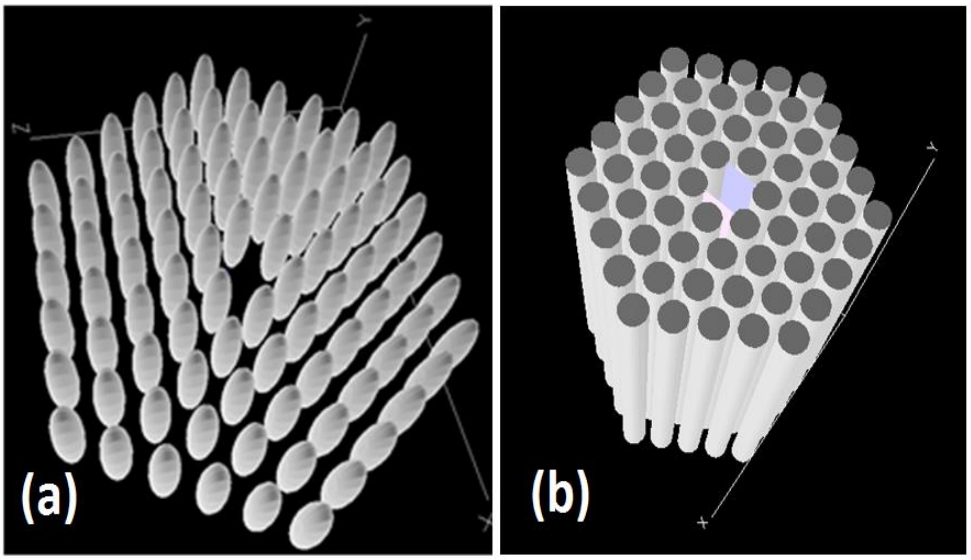

Figure 4.5 Hexagonal arrangement of silver (a) ellipsoidal and (b) cylindrical plasmonic crystal cavity.

4.3 Scattering model for silver ellipsoidal and cylindrical plasmonic crystal

It is observed that there is remarkable enhancement in asymmetric Fano resonance line shape, exhibited by the nanocavity introduced in hexagonally arranged ellipsoidal silver nanoparticles (see Figure 4.6 inset (iii)) as compared to cylindrical silver nanorods. Following scattering model is used to validate this observation.

Particles having ellipsoidal shape are smooth with no edges or corners which results into in-phase scattering of incident light unlike that of their cylindrical counterparts. The surface of an ellipsoid is defined by the following standard equation:

$$\frac{x^2}{a^2}+\frac{y^2}{b^2}+\frac{z^2}{c^2}=1 \tag{4.3}$$

where *a*, *b* and *c* are the semi-principle axes of the ellipsoid in Cartesian coordinates *(x, y, z)* system [113]. However, ellipsoidal coordinates (ξ, η, ζ) are preferred to determine the dipole moment and potential of an ellipsoidal particle in a uniform electric field. Therefore the surface of an ellipsoid in ellipsoidal coordinates (ξ, η, ζ) is defined as:

$$\frac{x^2}{a^2+\xi}+\frac{y^2}{b^2+\xi}+\frac{z^2}{c^2+\xi}=1, \quad -c^2<\xi<\infty \tag{4.4.a}$$

$$\frac{x^2}{a^2+\eta}+\frac{y^2}{b^2+\eta}+\frac{z^2}{c^2+\eta}=1, \quad -b^2<\eta<-c^2 \tag{4.4.b}$$

$$\frac{x^2}{a^2+\zeta}+\frac{y^2}{b^2+\zeta}+\frac{z^2}{c^2+\zeta}=1, \quad -a^2<\zeta<-b^2 \tag{4.4.c}$$

Also to any point *(x, y, z)* in Cartesian coordinates, there corresponds one set of ellipsoidal coordinates (ξ, η, ζ) which determine eight points, symmetrically located in each of the octants as given below [113]:

$$x^2=\frac{(a^2+\xi)(a^2+\eta)(a^2+\zeta)}{(b^2-a^2)(c^2-a^2)} \tag{4.4.d}$$

$$y^2=\frac{(b^2+\xi)(b^2+\eta)(b^2+\zeta)}{(a^2-b^2)(c^2-b^2)} \tag{4.4.e}$$

$$z^2 = \frac{(c^2+\xi)(c^2+\eta)(c^2+\zeta)}{(a^2-c^2)(b^2-c^2)} \quad (4.4.f)$$

Now, for a homogeneous ellipsoid placed in a uniform electric field aligned along *z*-axis, the potential Φ has symmetric properties as shown below:

$$\Phi(x, y, z) = \Phi(-x, y, z) = \Phi(x, -y, z) = \Phi(-x, -y, z)$$

and

$$\Phi(x, y, -z) = \Phi(-x, y, -z) = \Phi(x, -y, -z) = \Phi(-x, -y, -z) \quad (4.5.a)$$

Therefore, potential in only two octants having positive and negative *z* values is to be considered with the required condition that potential and its derivative are continuous on the plane $z = 0$. So, the octant in which the value of *x*, *y*, *z* is positive is chosen. Let Φ_0 denote the potential due to the external field E_0 whereas Φ_1 and Φ_2 denote the potential inside and outside the ellipsoid respectively. Further, let Φ_p, be the perturbing potential caused by the ellipsoid. Then, Φ_2 can be expressed as the superposition of Φ_0 and Φ_p, with Φ_0 given as:

$$\Phi_0 = -E_0 \left[\frac{(c^2+\xi)(c^2+\eta)(c^2+\zeta)}{(a^2-c^2)(b^2-c^2)}\right]^{1/2} \quad (4.5.b)$$

At sufficiently large distance from the ellipsoid the perturbing potential Φ_p is negligible and we observe that when $\xi >> a^2$ the limit

$$\lim_{\xi \to \infty} \Phi_p = 0 \quad (4.5.c)$$

Also, it is required that at the boundary of the ellipsoid, the potential should be continuous:

$$\Phi_1(0,\eta,\zeta) = \Phi_0(0,\eta,\zeta) + \Phi_p(0,\eta,\zeta) \quad (4.5.d)$$

Hence, the Laplace's equation to accurately describe the electric potential Φ in ellipsoidal coordinates is obtained and given as follows:

$$\nabla^2\Phi = (\eta-\zeta)f(\xi)\frac{\partial}{\partial\xi}\left\{f(\xi)\frac{\partial\Phi}{\partial\xi}\right\} + (\zeta-\xi)f(\eta)\frac{\partial}{\partial\eta}\left\{f(\eta)\frac{\partial\Phi}{\partial\eta}\right\} + (\xi-\eta)f(\zeta)\frac{\partial}{\partial\zeta}\left\{f(\zeta)\frac{\partial\Phi}{\partial\zeta}\right\} = 0 \quad (4.5.e)$$

where Φ is the scalar potential and expression f is defined for a variable q as

$$f(q) = \{(q+a^2)(q+b^2)(q+c^2)\}^{1/2} \quad (4.5.f)$$

Now in order to solve the Laplace's equation (4.5.e), using (4.5.b) we assumed that the potentials Φ_1 and Φ_p are of the form:

$$\Phi(\xi,\eta,\zeta) = F(\xi)\{(c^2+\eta)(c^2+\zeta)\}^{1/2} \quad (4.5.g)$$

and it follows from (4.5.e) that the function F(ξ) satisfies the ordinary differential equation:

$$f(\xi)\frac{d}{d\xi}\left\{f(\xi)\frac{dF}{d\xi}\right\} - \left(\frac{a^2+b^2}{4}+\frac{\xi}{2}\right)F(\xi) = 0 \quad (4.5.h)$$

yielding a solution of the form:

$$F_1(\xi) = (c^2+\xi)^{1/2} \quad (4.5.i)$$

which is verified by substituting it in (4.5.h) and follows from the fact that (4.5.b) satisfies the Laplace's equation (4.5.e).

A second linear independent solution to (4.5.h) is obtained by integrating (4.5.i):

$$F_2(\xi) = F_1(\xi) \int_{\xi}^{\infty} \frac{dq}{F_1^2(q) f(q)} \tag{4.5.j}$$

with the property $\lim_{\xi \to \infty} F_2(\xi) = 0$.

The function F_1 is not compatible with the required condition given in (4.5.c); therefore the perturbing potential of the ellipsoidal particle is given as:

$$\boldsymbol{\Phi_p(\xi, \eta, \zeta) = C_2 F_2(\xi)\{(c^2 + \eta)(c^2 + \zeta)\}^{1/2}} \tag{4.5.k}$$

and for the potential inside the particle to be finite at the origin, we must have:

$$\boldsymbol{\Phi_1(\xi, \eta, \zeta) = C_1 F_1(\xi)\{(c^2 + \eta)(c^2 + \zeta)\}^{1/2}} \tag{4.5.\textit{l}}$$

where C_1 and C_2 are constants. Therefore, the field inside the particle is uniform and aligned parallel to the applied field.

The boundary condition given in (4.5.d) yields an equation in constants C_1 and C_2 as mentioned below:

$$C_2 \int_0^{\infty} \frac{dq}{(c^2+q) f(q)} - C_1 = \frac{E_0}{\{(a^2-c^2)(b^2-c^2)\}^{1/2}} \tag{4.5.m}$$

And, the requirement that the normal component of the displacement vector be continuous at the boundary of the particle and the medium yields the second equation:

$$\varepsilon_m C_2 \left[\int_0^\infty \frac{dq}{(c^2+q)f(q)} - \frac{2}{abc}\right] - \varepsilon_1 C_1 = \frac{\varepsilon_m E_0}{\{(a^2-c^2)(b^2-c^2)\}^{1/2}} \quad (4.5.n)$$

This gives the required potential inside and outside the particle as follows:

$$\Phi_1 = \frac{\Phi_0}{1+\frac{L_3(\varepsilon_1-\varepsilon_m)}{\varepsilon_m}} \quad (4.5.o)$$

$$\Phi_p = \Phi_0 \frac{\frac{abc(\varepsilon_m-\varepsilon_1)}{2\quad\varepsilon_m}\int_\xi^\infty \frac{dq}{(c^2+q)f(q)}}{1+\frac{L_3(\varepsilon_1-\varepsilon_m)}{\varepsilon_m}} \quad (4.5.p)$$

where

$$L_3 = \frac{abc}{2}\int_0^\infty \frac{dq}{(c^2+q)f(q)} \quad (4.5.q)$$

The equation (4.5.o) and (4.5.p) give the potential at all points in space and is a consequence of the particle symmetry.

In a similar way, the solution for potential inside and outside the cylindrical particles can be obtained at all points in space. The details have been exhaustively given in the book by Bohren and Huffman [113] which also describes the polarizability tensor and the scattering matrix. It is inferred from the scattering matrix, that scattering is attributed to the particles which are not spherically symmetric and an ellipsoid can be easily approximated to sphere for a=b=c, unlike cylinders [113]. Therefore, ellipsoidal particles are more likely to result into in-phase scattering as compared to cylindrical particles.

The inference of the scattering model discussed above is that the shapes of the particles have noteworthy influence on the scattered waves. The resultant

wave scattered in a given direction by a particle is due to the interference of the scattered waves from the entire volume. Thus it is concluded that the maximum scattered intensity is obtained when angle between the scattering surface and the incident field is small. With this qualifier, the in-phase scattering in ellipsoidal geometry vis-à-vis cylindrical geometry is compared and studied.

4.4 Results

This section briefly summarizes the important results obtained for the proposed systems.

4.4.1 Ultrahigh transmission in ellipsoidal silver nanorods cavity

The asymmetry observed in the response of the cluster of ellipsoidal silver nanorods (ESN) results from the introduction of the nanocavity and the characteristic ellipsoid shape (see Figure 4.6). Fano resonance can be described by a general formula based on Maxwell's equation derived by Gallinet and Martin [116], which includes the contribution of electromagnetic interactions:

$$\sigma_a(\omega) = \frac{\left(\frac{\omega^2-\omega_a^2}{2W_a\omega_a}+q\right)^2+b}{\left(\frac{\omega^2-\omega_a^2}{2W_a\omega_a}\right)^2+1} \tag{4.6}$$

where ω_a is the resonance frequency, W_a is the spectral width in frequency units, q is the asymmetry parameter and b is the damping parameter.

This equation describes Fano resonance for lossy materials in defined plasmonic nanostructures.

FDTD method is employed for scattered waves for controlling the scattering of the plasmonic nanoparticles for ellipsoidal silver nanorods and cylindrical silver nanorods (CSN).

In both cases, asymmetric output curves are observed (blue curves in Figures 4.6 and 4.7), in contrast to the symmetric source profile shown as the green curves in Figure 4.6 (inset (i)) and Figure 4.7. These output asymmetric curves represent the unique characteristic of Fano resonance.

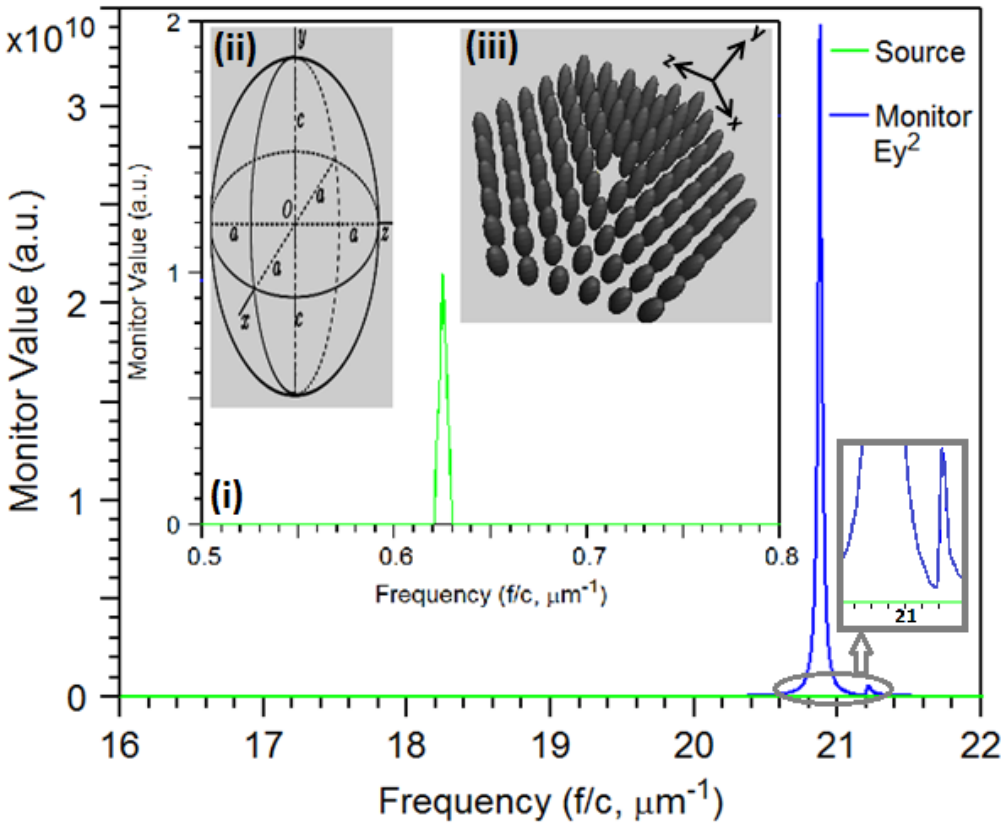

Figure 4.6 Cavity response of hexagonally arranged ellipsoidal silver nanoparticles, the zoomed out illustration shows the asymmetry in the output response. Inset (i) displays the symmetric input source profile, inset (ii) presents the semi-axes 'a', 'b' and 'c' of the ellipsoid and inset (iii) presents cavity in the hexagonal arrangement of the silver ellipsoids.

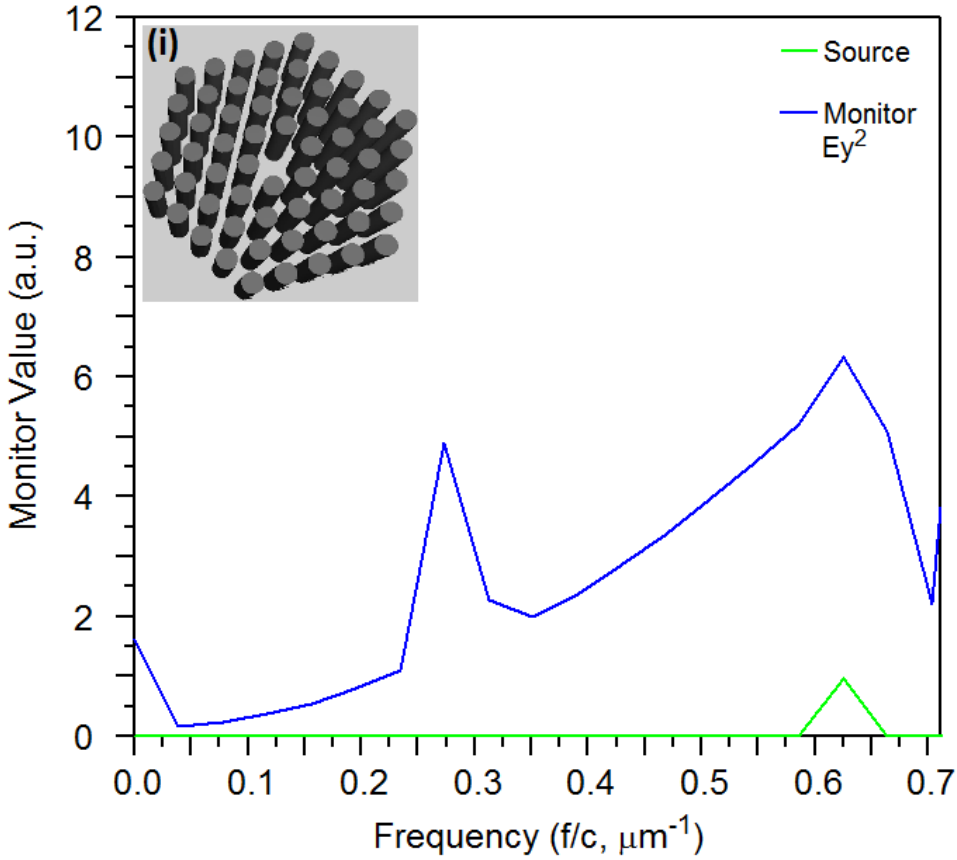

Figure 4.7 Cavity response of hexagonally arranged cylindrical silver nanorods with inset (i) presenting the arrangement of the cylindrical nanorods.

Transmission is given as $T = 1 - E$, where T is the transmission and E is the extinction, which includes losses due to absorption A and scattering S of the cavity. Transmission in the case of ESNs is extraordinarily high (Figure 4.6) in comparison to CSN (Figure 4.7). This ultrahigh transmission can be attributed to the geometry of ESNs, the cross-sectional area ($\sigma_{\text{prolate ESN}} = \pi a^2$) of which varies smoothly as semi-axis $a = b$ decreases gradually from $a = a_{\max}$ to $a = 0$ and semi-axis c varies from $c = 0$ to $c = c_{\max}$. This is in contrast to the sudden boundary change in the case of CSNs at $c = c_{\max}$, which causes extreme scattering losses.

The absorption losses are negligible in both cases, thereby making scattering the main factor that contributes to the extinction. Therefore, these observations validate the distinct shape enhancement of the asymmetric line shape of Fano resonance in ESNs, in contrast to CSNs, due to the interference of

the superradiant bright cavity mode and the subradiant dark mode. This is also evident in the 3D contour plots of the field distribution in the cavities formed in ESNs and CSNs [see Figure 4.8 (a) and (b)].

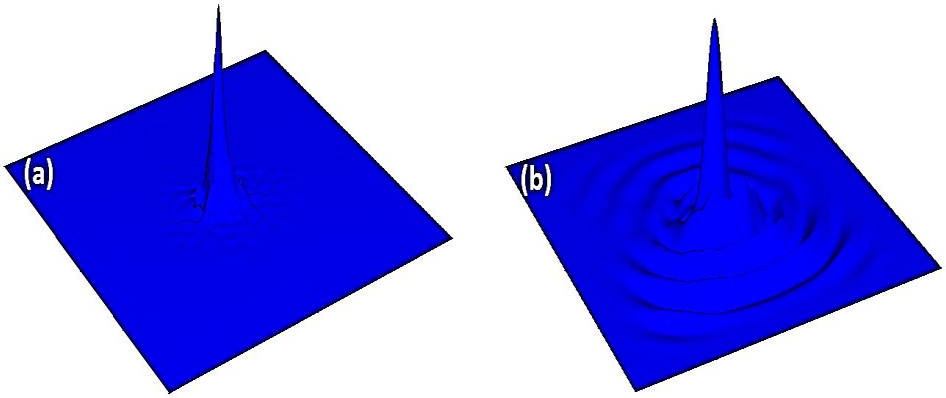

Figure 4.8 3D contour plot of the field distribution in the cavity formed in ESN and CSN.

Characteristic Fano curves are obtained for different input wavelengths, as shown in Figure 4.9 (a) and (b). For ESN cavity, as the input wavelength increases, the transmission through the cavity also increases until 800 nm, after which it decreases until 1300 nm. Between 1300 and 1600 nm, there is a steep rise in transmission, which is followed by a fall at 1800 nm and again a rise at 2100 nm.

All the curves are characterized by a short peak (Peak 1) followed by a central peak (Peak 2); these peaks represent the asymmetric Fano profile.

The maximum transmittance is obtained at 1600 nm with peak values of 23699.73 and 184840.60 (arbitrary units) for Peak 1 and Peak 2, respectively [see Table 4.1 and Figure 4.9 (b)]. This indicates that the considered ESN is suitable for applications in lasing and for plasmon-induced transparency.

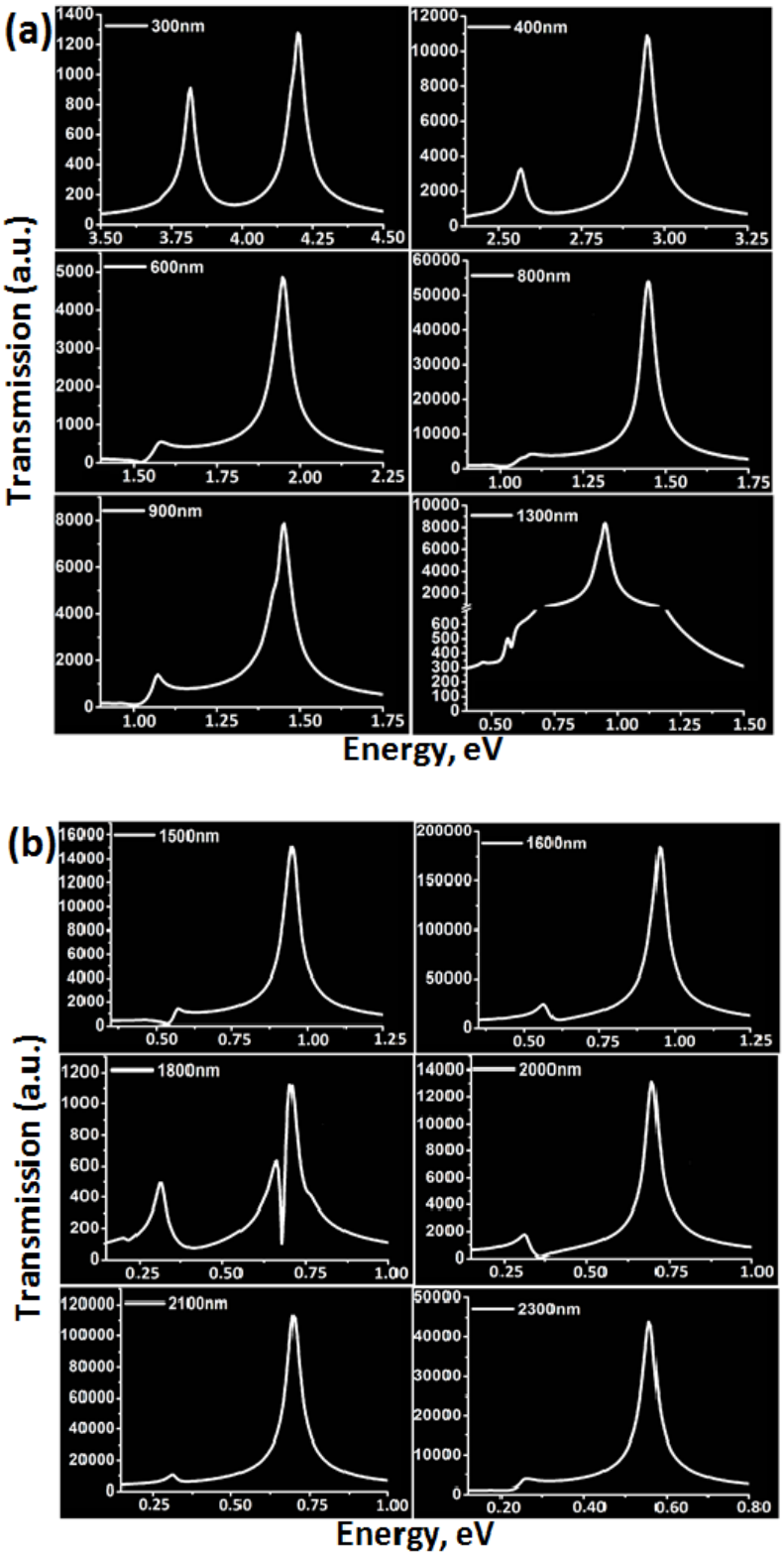

Figure 4.9 (a) and (b) Transmission characteristics (1-Extinction; for normalized output) of the ESN cavity for different input wavelength presenting the variation in Fano lineshapes.

TABLE 4.1: Peak amplitude values obtained for peak 1 and 2		
Wavelength (nm)	**Peak 1 (a.u.)**	**Peak 2 (a.u.)**
100	8195.91	21637.04
200	4150.61	6232.61
300	910.58	1277.39
400	3284.35	10887.45
500	534.00	4001.24
600	551.93	4861.58
700	231.15	1519.85
800	4238.18	54694.67
900	1382.95	7869.13
1000	716.09	2776.31
1100	414.84	3917.64
1200	332.44	1322.46
1300	502.39	8409.09
1400	332.27	1248.81
1500	1412.12	15042.29
1600	23699.73	184840.60
1700	9740.62	29054.09
1800	631.10	1120.833
1900	758.33	2368.738
2000	1758.96	13138.58
2100	10367.99	113064.20
2200	3028.58	3360.73
2300	3861.49	43866.16

The peak values obtained in each case are tabulated in Table 4.1 and the variation of peak amplitude with wavelength is presented in Figure 4.10.

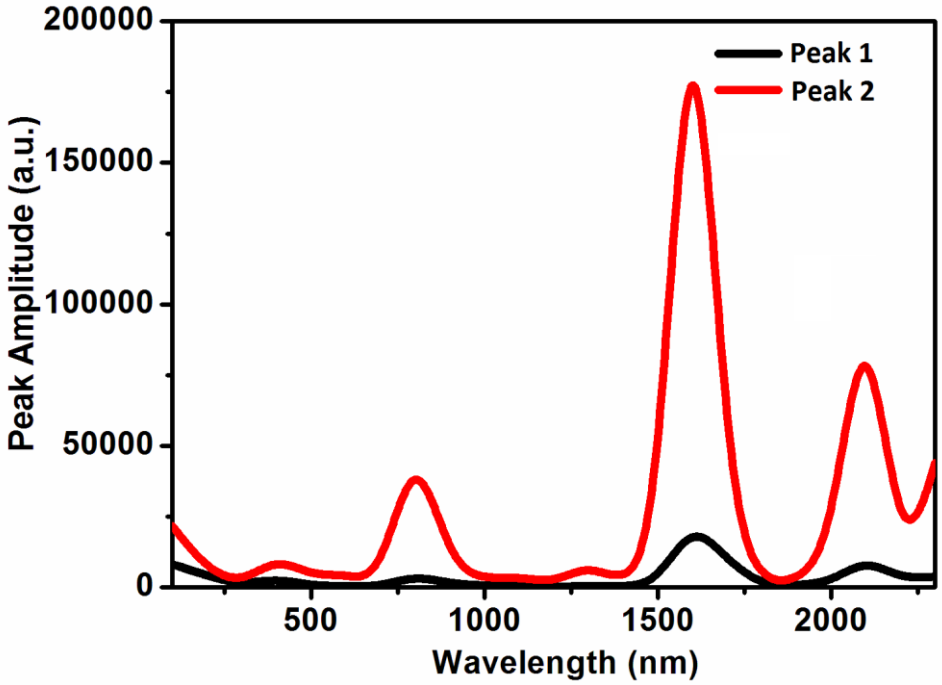

Figure 4.10 Spectral variation of peak amplitude for the ESN cavity highlighting switching application.

4.4.2 Higher harmonic generation

The ESN cavity response demonstrated in Figure 4.10 reveals bands which reflect significant Fano resonance centered at λ_1 = 800 nm, λ_2 = 1600 nm and λ_3 = 2100 nm. The peak wavelengths of the second and third bands (λ_2 and λ_3) are exactly twice and approximately three times that of the first band (λ_1). The formation of bands at regular intervals appears to be related to geometry-dependent nonlinear optical phenomena such as sum/difference frequency generation, that is, frequency mixing processes, which lead to significant Fano resonance.

Moreover, when we closely analyze the response of the ESN cavity shown in Figure 4.6, we find that for an input frequency of 1.875×10^8 s^{-1} (corresponding to 0.625 μm^{-1}; green curve in the inset (i) of Figure 4.6), the

cavity transmits a frequency of 62.7×10^8 s^{-1} (corresponding to 20.9 μm^{-1}; blue curve in Figure 4.6). Thus, the output frequency is approximately 33 times the input frequency, confirming the occurrence of HHG and the storing of energy at higher frequencies. Therefore, HHG also contributes to ultrahigh amplification of the input signal in ESNs but not for CSNs (see Figure 4.7) resulting in the shape-enhanced Fano resonance in ESN cavity.

4.4.3 Power dependence and switching application

The difference in the amplitudes of Peak 1 and Peak 2 of ESN can be exploited for switching applications. From the curves in Figure 4.10, three peaks (i.e. 800, 1600 and 2300 nm) are identified suitable for switching applications because of their different peak amplitudes.

By varying the power, the line shape of the Fano resonance can also be controlled by enhancing the continuum transition rate to match the saturated discrete level transition.

Four different input powers viz. 0.01, 0.1, 1.0 and 10 mW termed P_1, P_2, P_3 and P_4, respectively, were applied in the ESN cavity. The effect of the input power on the transmission spectrum at the wavelengths λ = 800, 1600 and 2300 nm is shown in Figure 4.11 (a), (b) and (c), respectively.

The ratios of the peak amplitudes, i.e. Γ = Peak 2/Peak 1, are summarized in Table 4.2.

Table 4.2: Ratio of peak amplitudes Peak 2/Peak 1 for different input power P_1, P_2, P_3 and P_4

Wavelength (nm)	P_1	P_2	P_3	P_4
800	0.95	1.71	12.91	1.05
1600	0.68	1.80	7.79	3.52
2300	0.43	0.22	11.36	3.85

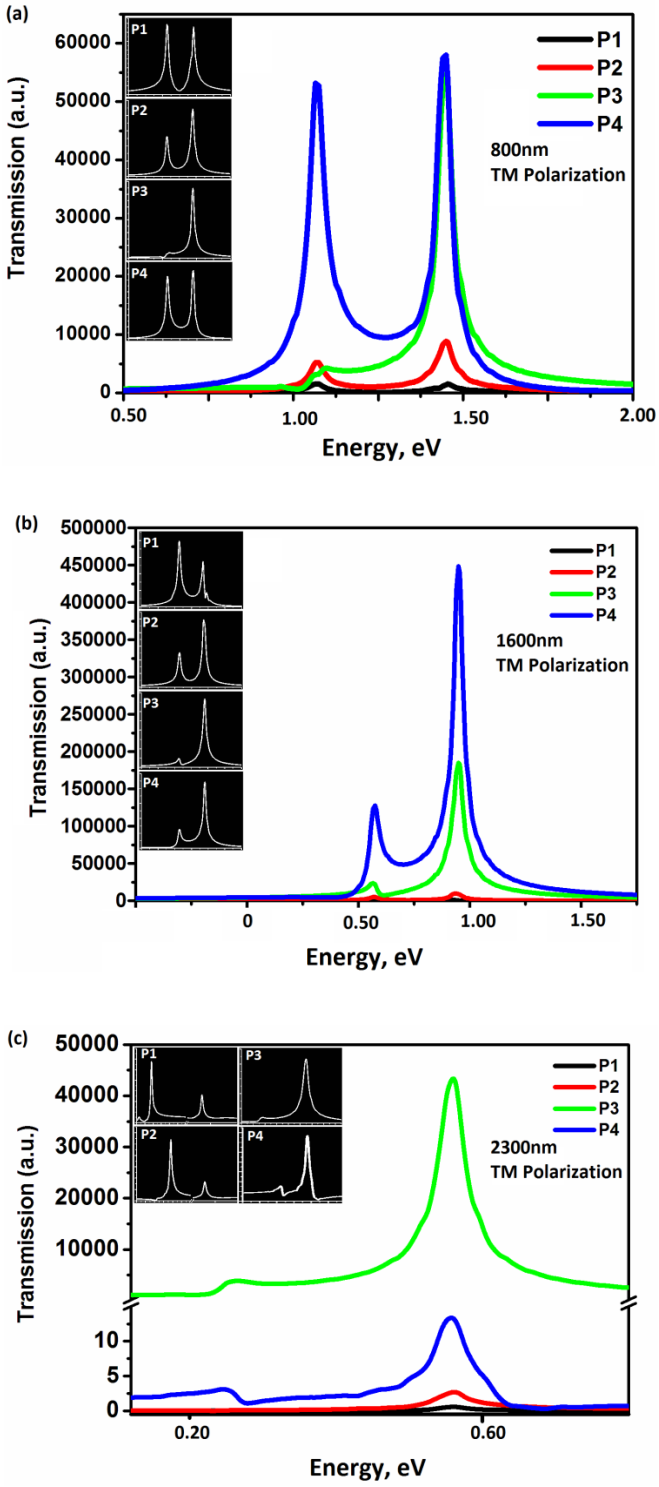

Figure 4.11 (a), (b) and (c) Power dependence of Fano lineshapes showing the adaptation of resonance profile with varying input power. TM polarization establish strong mutual coupling resulting in distinct Fano profile.

At 800 nm for power P_1, Peak 1 is larger than Peak 2 (i.e. $\Gamma < 1$) but as the input power is increased to P_2 and above, the amplitude of Peak 1 decreases and the amplitude of Peak 2 increases, such that $\Gamma > 1$. The maximum value of Γ (12.91) is obtained for input power P_3, thereby making this the optimum operating power to achieve maximum switching efficiency in the proposed ESN. The lower switching efficiency for power P_4 may have been due to the power applied to the cavity being exceeding the tolerance limit of the structure. At power P_3, the values of Γ obtained at 1600 and 2300 nm, were 7.79 and 11.36, respectively. From these observations we conclude that the best switching capability of the ESN cavity is obtained for a wavelength of 800 nm at a power of 1.0 mW.

4.4.4 Polarization dependence

Plots for TM and TE polarized light at different input powers for λ = 800, 1600 and 2300 nm are given in Figure 4.11 and Figure 4.12, respectively. For TM polarization, the electric field component is parallel to the longitudinal semi-axis '*c*' of the ellipsoids resulting in the alignment of the charges along the *y* axis. This, in turn, results in strong mutual coupling of the electrical field components between the ellipsoids and, hence, coherent coupling to the radiation continuum.

Accordingly, for TM polarization, well-defined, distinct Fano resonance line shapes are obtained, as illustrated in Figure 4.11 (a), (b) and (c). However, for TE polarization, the electric field is parallel to the shorter semi-axis '*a*', which is transverse to the longitudinal direction. Hence it results in weak mutual coupling and multiple random peaks in the transmission response of the cavity, as presented in Figure 4.12 (a), (b) and (c). These results have therefore demonstrated that the Fano line shape is polarization dependent.

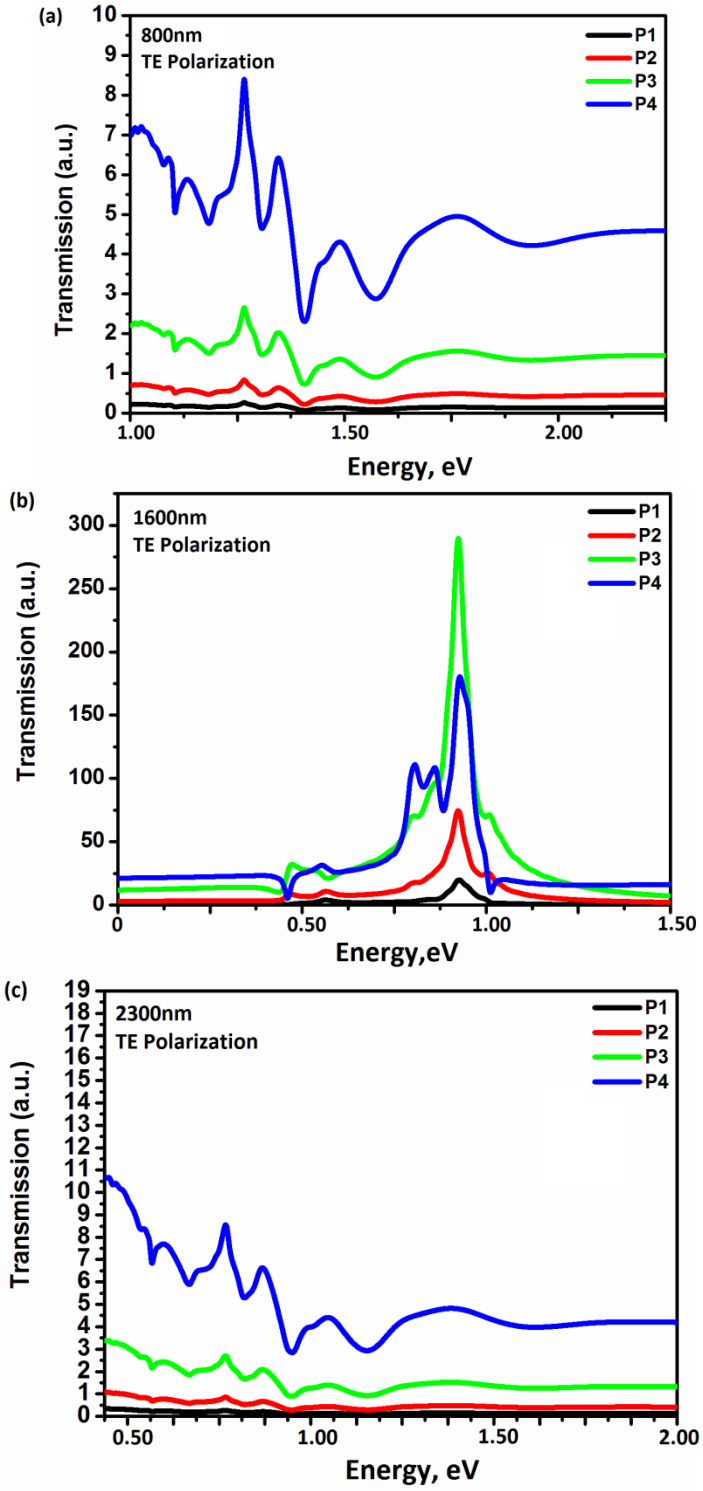

Figure 4.12 (a), (b) and (c) Effect of TE polarization on the Fano lineshapes validating weak mutual coupling.

4.5 Summary

Fano resonance is observed and studied in ellipsoidal silver nanorods and cylindrical silver nanorods. A scattering model is used to gain an understanding of how the structural symmetry controls the in-phase scattering. FDTD method is used to model and analyze the results. The ESN cavity, which exhibits ultrahigh transmission at 1600 nm because of HHG, can be used for applications in lasing and plasmon-induced transparency. The influence of input power and its application in switching is demonstrated with maximum efficiency displayed in the visible region. The Fano response of the proposed system revealed that different wavelength regimes are suitable for different applications, thereby highlighting the potential of the ESN cavity in a broad range of applications including lasing, switching, sensing, design of surface plasmon polariton-based filters.

Chapter 5
Resonant plasmon tunneling in silver nanodisk dimer[1]

5.1 Introduction

From the previous chapter it is learnt that a particular cluster of metal nanoparticles support Fano resonance and can be employed in sensing, lasing etc due to high transmission. Yet another effect that adds to the extraordinary transmission is resonant plasmon tunneling. There are many factors that control resonant plasmon tunneling for example interparticle distance, size of the particles however in addition to this skin depth effect, incident wavelengths also contribute to the resonant plasmon tunneling and is discussed in this chapter.

Tunneling is quantum mechanical phenomenon which allows a particle to tunnel through a barrier that it classically could not overcome. Related applications are tunnel diode, quantum computing, scanning tunneling microscope etc. In optics photon tunneling refers to transmission of light through apertures that have dimensions smaller than the incident wavelength of the light by tunneling. Resonant tunneling refers to tunneling through a structure yielding sharp peaks about certain energies in transmission spectra obtained of the structure under study (conventional structure comprise of quantum well sandwiched between two tunnel barriers)

5.1.1 Resonant plasmon tunneling

Resonant plasmon tunneling occurs in closely spaced metal-insulator-metal system and hence has contribution in transmission spectra. Resonant tunneling of surface plasmon polariton across interruption in the metallic film observes high tunneling efficiency with greater amplitude transmission [123]. Plasmon

[1] A part of the results reported in this chapter has been communicated to a peer reviewed journal.

tunneling transmits energy and hence enhances forward transmission [129] leading to extraordinary transmission even without the presence of holes [130] exhibiting enhancement in transmission several orders of magnitude compared to the predicted values. Plasmon induced resonant tunneling can be manipulated using an external static magnetic field and monitored during the excitation of SP modes to be used as resonator or waveguide. Hence it is needed that various systems of metal nanostructures should be studied to set a platform for plasmon tunnelled devices such as plasmon tunnel diode, plasmonic Josephson junction assisted superconductivity, plasmon tunnelled field-effect transistors etc.

Plasmon mediated transfer of energy holds an important key in explaining how a nanoplasmonic system would behave. Resonant plasmon tunnelling is one such phenomenon that allows transfer of energy and needs to be researched extensively as it involves nano regime complexity. Plasmon tunneling is opening avenues for applications such as coupling of single quantum emitters [117], locally controlled enhanced fluorescence[118], single surface plasmon polariton (SPP) interferometry [119], single SPP mediated energy transfer [120] etc.

For metallic nanostructures at nanometer spacing, free electrons tend to couple electrically across the gap [121] resulting in plasmons with enhanced optical fields confined within the gap where tunnelling becomes significant. Optical resonant tunnelling effect of surface plasmons has been studied in various periodic structures such as silver film with zero order gratings [122], metal films with symmetrical and non-symmetrical geometries [123], evanescent tunnelling of plasmons in metal grating [124], metamaterials [125] etc. But, with metal nanoparticles (MNPs) the plasmonic system truly goes quantum by incorporating the “wave” nature of matter exhibited in ultra-small MNPs whereas “particle” nature for quantum information processing [126, 127].

MNPs having sub-nanometer dimensions or gap whether individual, dimers, array or hybrid, with quantum dots exhibit quantum plasmon resonances, non-linear effects in field enhancement Fano resonance [128] etc.

5.1.2 Gradient potential dependent skin depth theory

As discussed above, it is perceived that metal nanoparticles concede remarkable results. This section confers resoant plasmon tunneling through silver nanodisk dimer, and also the role of incident wavelength on skin depth and thus on tunneling. Gradient potential dependent skin-depth theory (GPST) explains resonant plasmon tunneling for the dimer system with sub-nanometer interparticle distance. The region between adjacent nanodisks gives rise to gradient potential due to the property of its geometry leading to the formation of tunneling zone and is substantiated by finite difference time domain computational method. Energy eigen value and wavelength eigen values are obtained for the dimer system.

If the interparticle distance between two metal nanodisks is just few nanometer (see Figure 5.1 (a)), the force and hence the potential on bisector XY is maximum at radial centre represented by a circle (Figure 5.1 (b), from both the disks lying at the shortest distance from the boundary points P and P' of the two particles. Therefore the potential decreases with increasing distance between the boundary of the particle and that of bisector and is represented by a star symbol in Figure 5.1 (b). So, the geometry of the nanodisk instigate region of varying potential (Figure 5.1 (b)) with V_{max} and V_{dec} represented as circle and star respectively.

As the nanodisks come closer, this region of varying potential between both the particles overlaps (Figure 5.1 (c)). This overlapping gives rise to a region of gradient potential between two consecutive nanodisks as shown in Figure 5.1 (d) and is marked as tunneling zone.

The common overlapped domain acts as a tunneling zone for plasmons facilitating strong plasmon-plasmon interaction for adjacent metal nanodisks in an array of nanoparticles forming a periodic system (Figure 5.1 (e)). This periodic system along with the region of gradient potential between the particles act as a corrugated metal-insulator system and thus skin depth comes into effect.

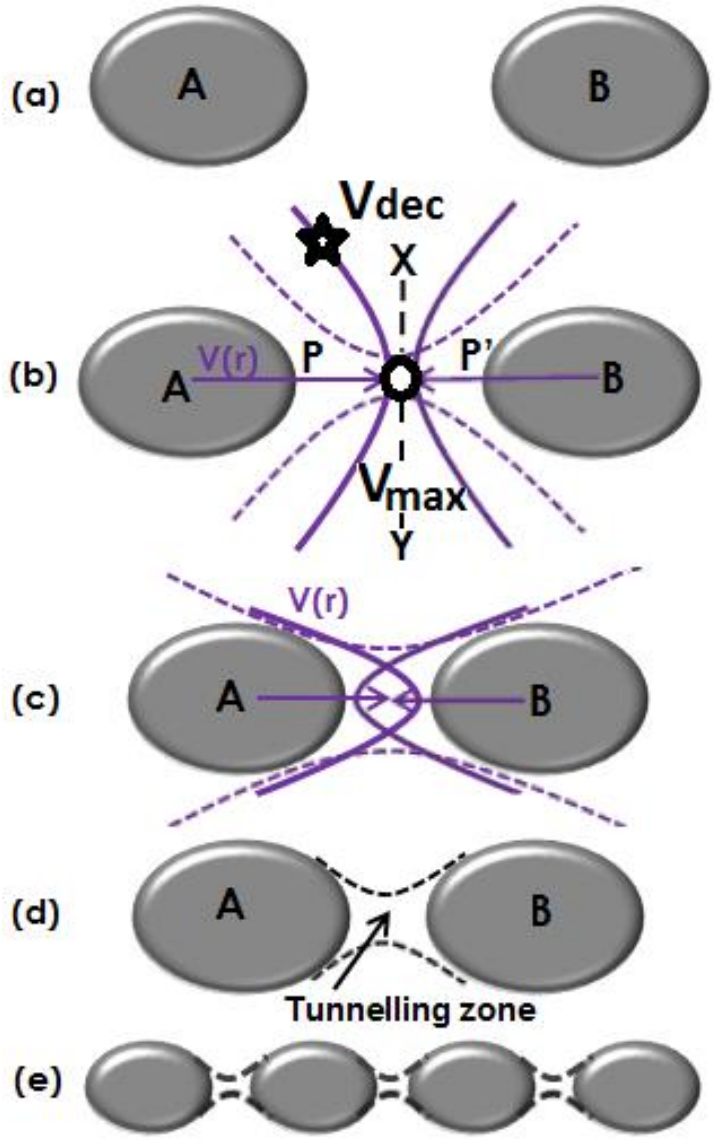

Figure 5.1 Schematic representations of closely spaced silver nanodisks revealing formation of tunnelling zone between the nanodisks. (a) Closely spaced silver nanodisks with subnanometer interparticle distance. (b) Variation of potential between the nanodisks. (c) and (d)The region of high potential overlaps as the disks come closer forming a tunnelling zone which assists resonant plasmon tunnelling. (e) Array of closely spaced nanodisks with tunnelling zone forming a periodic arrangement.

5.1.3 Skin depth effect

Skin depth effect is an important phenomenon which cannot be ignored when a region of very high potential between nanoparticles is expected with sub-

nanometer interparticle spacing. It is possible via plasmonics that optical field can be localized tightly if the size of metal nanoparticles is smaller than the skin depth [131]. Skin depth which is a wavelength dependent function plays a pivotal role in resonant tunneling mechanism since it can control the losses due to retardation effects, transmission, radiation etc.

As skin-depth is a function of incident wavelength, it is observed that larger incident wavelength results in increased skin depth (see Figure 5.2) and hence increases the total tunnelled intensity at the output end of the system. Figure 5.2 reveals that as the incident wavelength increases it has deeper skin effect while propagating through the particles.

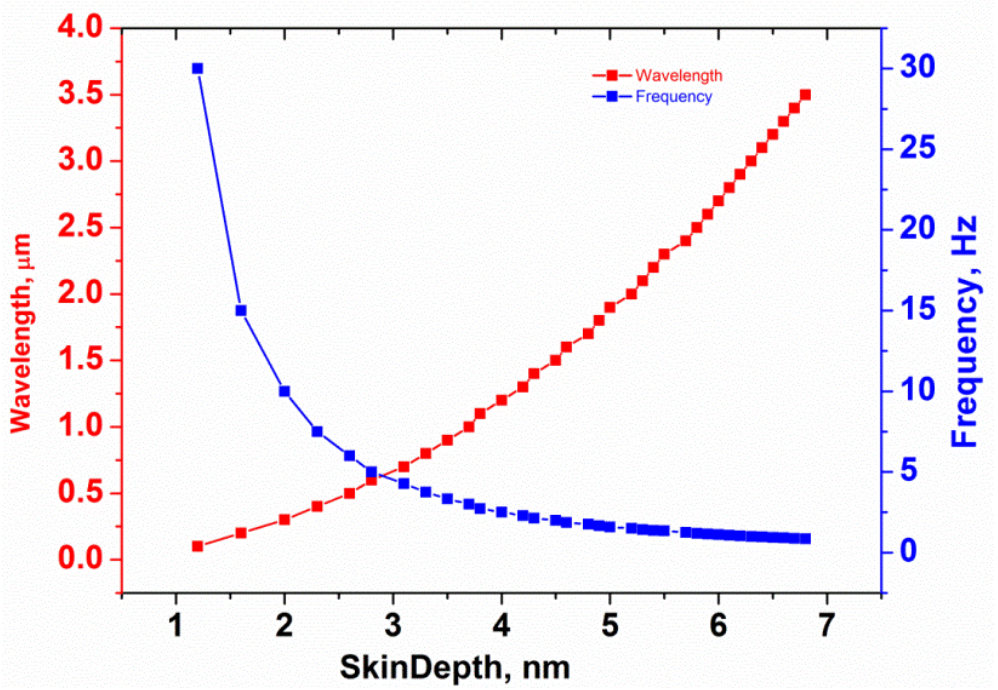

Figure 5.2 Plot showing skin depth dependence on incident wavelength and the corresponding frequency.

Therefore the gradient potential present between the silver nanodisks along with wavelength dependent skin depth effect assists resonant plasmon tunneling through the nanoparticles system.

5.2 Silver nanodisk dimer

The system under study comprises of silver nanodisk dimer system with radius 10 nm and interparticle spacing of 5nm or less. An important point to be considered in case of the metal nanoparticles is that there is local field enhancement at each individual nanoparticle. With interparticle distance less than few nanometers these local fields interact and the resultant output is actually the synergy of the enhanced local field and the skin depth effect. Also, the size of the nanoparticle plays an important role in tunneling mechanism, that is, if the particle size is smaller than the skin depth for a particular incident wavelength then the tunneling efficiency is more and if the particle size is larger than the skin depth then the system exhibit less tunneling efficiency. Furthermore, the output is expected to be the resultant of in-phase interaction among the tunnelled plasmons (bonding mode) or out-of-phase interaction (antibonding mode) regardless of the particle size. It is realised from the plot (Figure 5.2) that as the incident wavelength increases, the skin depth increases respectively and is between 3-4nm for infrared regime. To comprehend the effect of skin depth on a nanoparticle we take a silver nanodisk of radius 10nm and study the transmission spectra for the same over a range of input wavelengths with transverse magnetic (TM) polarization.

5.3 Results

The normalized transmission spectra obtained using finite difference time domain method is shown in Figure 5.3 and the system exhibit a distinctive configuration. It is perceived that there are few allowed energy bands that are particular to this system and the spectra is illustrated with respect to wavelength in the inset of Figure 5.3. Plot in the inset reveals out that the incident wavelength of 1.1μm has gained the most due to skin depth effect.

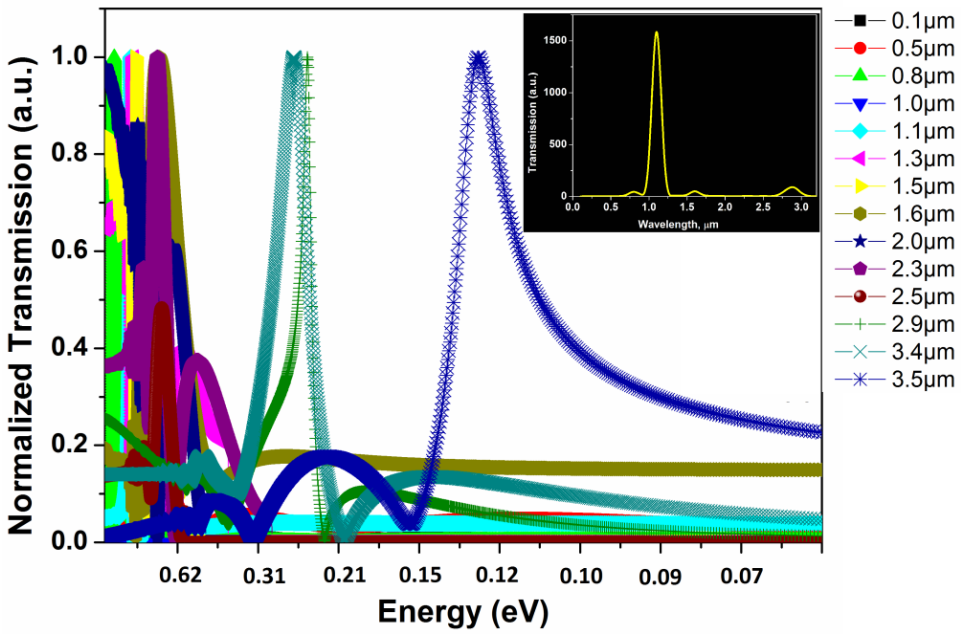

Figure 5.3 Normalized tranimission spectra for a silver nanodisk revealing allowed energy bands for the system. The inset highlights the wavelength of 1.1μm gains the most due to skin depth effect.

These bands are analogous to the energy eigen values and corresponding frequencies for the nanodisks system. Hence, the eigen values entails more tunnelling efficiency and the effect is maximum. Therefore we consider the wavelength of 1.1μm as the input wavelength from launch L and proceed with a system of two silver nanodisks dimer as shown in Figure 5.4 (a) and vary the interparticle distance with monitors M_1, M_2 and M_3 to record the transmission from d_1 to d_8 as 5.00nm, 4.00nm, 3.00nm, 2.00nm, 1.75nm, 1.50nm, 1.25nm and 1.00nm as shown in Figure 5.4 (c) to (j). It is observed that when the interparticle distance between the two nanodisks is less than 1.5nm, there is a significant overlap of the gradient potential of the two resulting in the formation of tunneling zone and it is also verified through electric field profile obtained via finite difference time domain method. Electric field Ey, profile obtained for the system (see Figure 5.4 (b)) confirms tunnelling zone which assists resonant plasmonic tunneling. Besides, depending upon the interparticle distance there can be a node

(Figure 5.4 (k)) or antinode (Figure 5.4 (l)) at the position of the monitors M_2 and M_3 contributing to the overall tunneling efficiency.

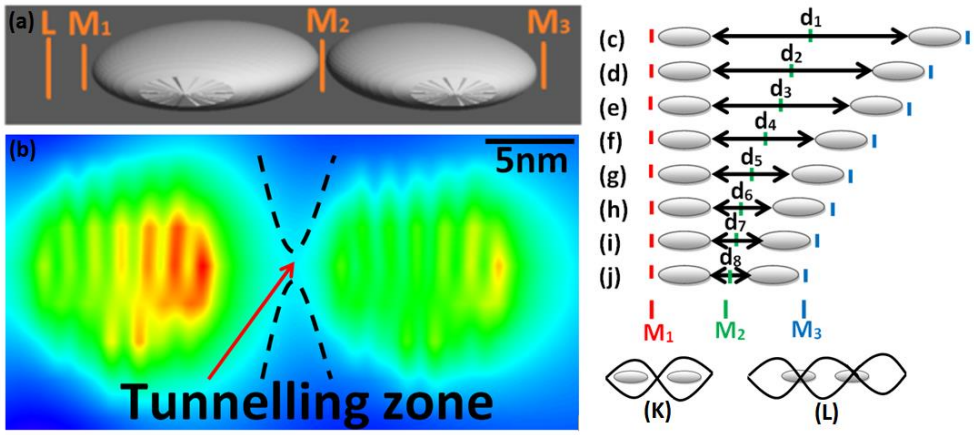

Figure 5.4 (a) System of silver nanodisk dimer with subnanometer interparticle spacing with 'L' as the launch and monitors M_1, M_2 and M_3 to record the transmission spectra. (b) Electric field profile for the nanodisk dimer with significant field intensity between the disks edifying the tunnelling zone. (c) to (j) Diagrammatic representation of variation of distance between the dimers from d_1 to d_8 (k) and (l) Illustration depicting formation of node and antinode between the nanodisk consequently contributing to the total tunnelled efficiency.

The incident wavelength of 1.1μm is launched from L, and the monitors M_1, M_2 and M_3 measure the transmission spectra with respect to the position of the monitor as shown in Figure 5.5 (a), (b) and (c) and hence revealing the tunneling efficiency as the distance between the two disks decreases from d_1 to d_8 as 5.00nm, 4.00nm, 3.00nm, 2.00nm, 1.75nm, 1.50nm, 1.25nm and 1.00nm.

The reason for analysing them separately through these plots is very exciting. It is observed that for the input monitor M_1 all the curves obtained are symmetrical and exhibit single peak centred at λ_1= 0.84 μm (Figure 5.5 (a)) although there is a blue shift (or high energy shift) with respect to the input wavelength which happens due to the interaction of the enhanced local field of the first particle with the incident beam.

But at second monitor M_2 we notice some remarkable results. After the resonant plasmons tunnel through the first nanodisk the transmission

characteristics obtained on monitor M_2 reveal two additional peaks λ_2 at 0.88 μm (±0.01μm) and λ_3 at 1.0 μm (±0.01μm) along with the central peak λ_1 (Figure 5.5 (b)). These subsequent multiple peaks at frequent intervals represent the allowed wavelengths corresponding to the allowed energy eigen values E_1, E_2 and E_3 for the silver nanodisk dimer system.

Also, another important observation is that as the distance between the nanodisks decreases from d_1 to d_3 it is realised that there is steady increase in transmission but as the distance decreases further from d_4 to d_8 transmission due to plasmon tunneling increases significantly; with d_4 and d_5 showing maximum attributed to the in-phase (bonding mode) interaction of tunnelled plasmons at M_2. This happens because when the distance is 1.5 nm or less, then the gradient potential of the two nanodisks form tunnelling zone supporting resonant plasmon tunnelling and hence resulting in increased transmission.

Further, as the transmission is recorded on the third monitor M_3 we observe that there are four additional peaks λ_2 at 0.88 μm (±0.01μm), λ_3 at .94μm (±0.01 μm), λ_4 at 1.02μm (±0.01 μm) and λ_5 at 1.16μm (±0.01 μm) along with the central peak λ_1 as shown in Figure 5.5 (c). These wavelengths correspond to the energy eigen values E_1 to E_5 (Figure 5.5 (c)) for the dimer system.

The intensity of transmission on the monitor placed at M_3 position decreases with decreasing distance from d_1 to d_8 because as the nanodisks get closer, the dimer acts as a bigger particle offering larger resistance to the tunnelling plasmons as well as out-of-phase interaction (antibonding mode) resulting in decreased intensity.

Moreover, observing these transmission spectra in Figure 5.5 (b) and (c), it is realised that there is an increase in number of eigen values on M_3 as compared to that on M_2. This is attributed to the redistribution of energy when the tunnelling plasmons pass through second nanodisk (in case of M_3) and the system behaves as a coupled oscillating system due to the formation of tunnelling zone between the two nanodisk unlike in case of M_2. Hence the proposed theory of

gradient potential with skin depth dependence helps in understanding the output of the silver nanodisks dimer.

In addition to the above results the transmission spectra were obtained with respect to the distance having curves mapped on the three monitors for a fixed value of distance. Figure 5.6 (a) to (h) demonstrate the transmission spectra obtained on M_1, M_2 and M_3 when the distance between the nanodisks varies from d_1 to d_8 respectively. The curves acquired on the monitors M_1, M_2 and M_3 representing transmission characteristics are shown in black, red and blue colours respectively (see Figure 5.6).

It is worth mentioning that the values obtained on the monitors M_2 and M_3 are of notable intensity which can be due to the significant tunneling of resonating plasmons with decreasing distance between the nanodisks (Figure 5.6 (a) to (h)). But, there is no regular increasing or decreasing pattern when distance between the nanodisks decreases from d_1 to d_8. This can be understood from Figure 5.4 (k) and (l) since the position of the monitors M_2 and M_3 varies when distance changes from d_1 to d_8 (Figure 5.4 (c) to (j)) and there can be formation of node or antinode at the position of M_2 and M_3 resulting in less or high intensity peaks.

Hence, it is inferred from Figure 5.4 (k) and (l) that when the distance is more than what is required for tunnelling zone, then the factors which control the tunnelling are node or antinode formationalong with in-phase or out-of-phase interaction at the monitor position yielding overall resonating plasmons' tunnelled efficiency. But when the disks are appreciably close resulting in tunnelling zone then it is the gradient potential and the skin depth effect which control the total tunnelled efficiency.

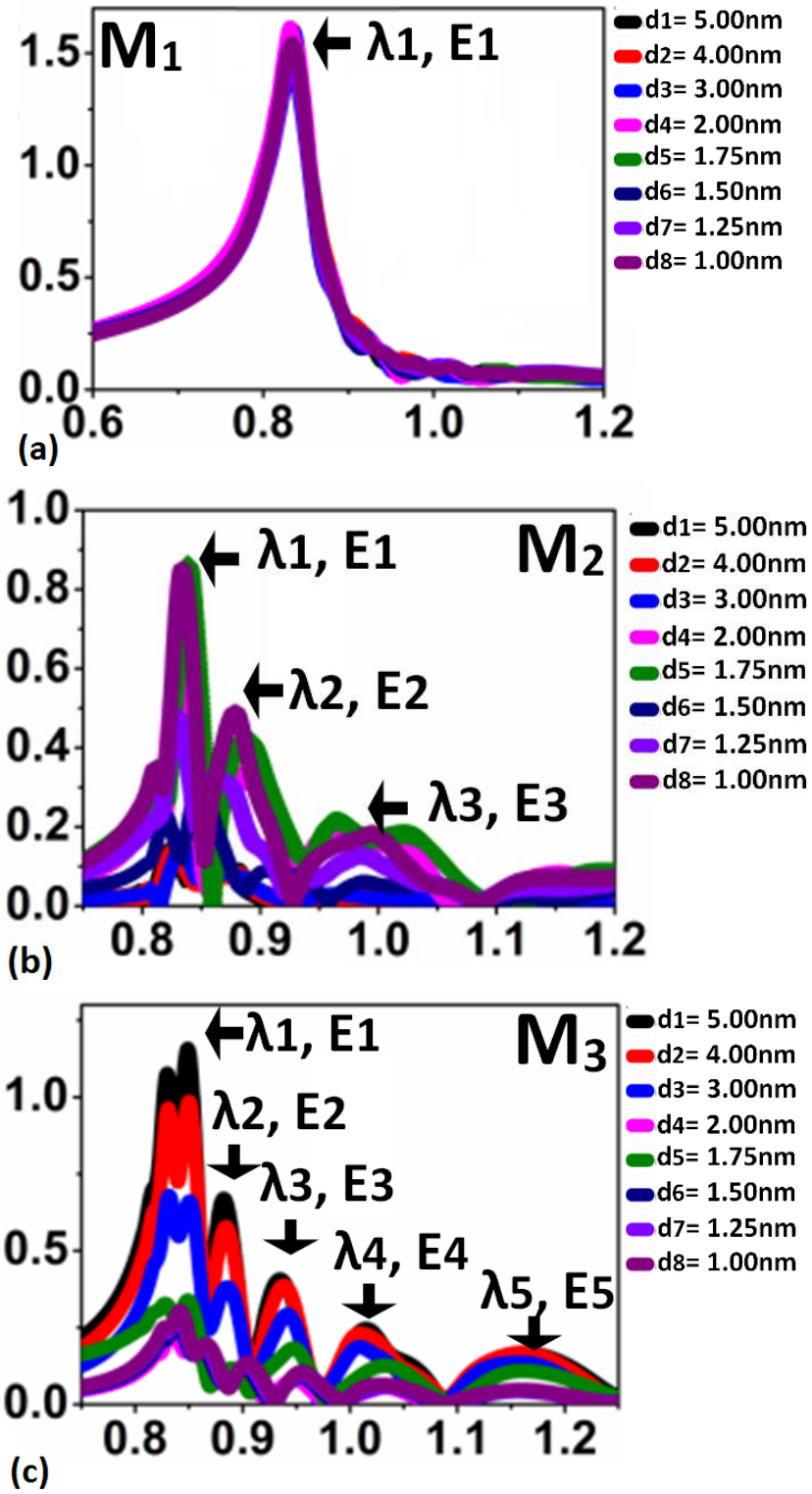

Figure 5.5 (a), (b) and (c) Show transmission spectra obtained on monitors M_1, M_2 and M_3 respectively with wavelength and energy eigen values in (b) and (c) after tunnelling through the first and second nanodisk

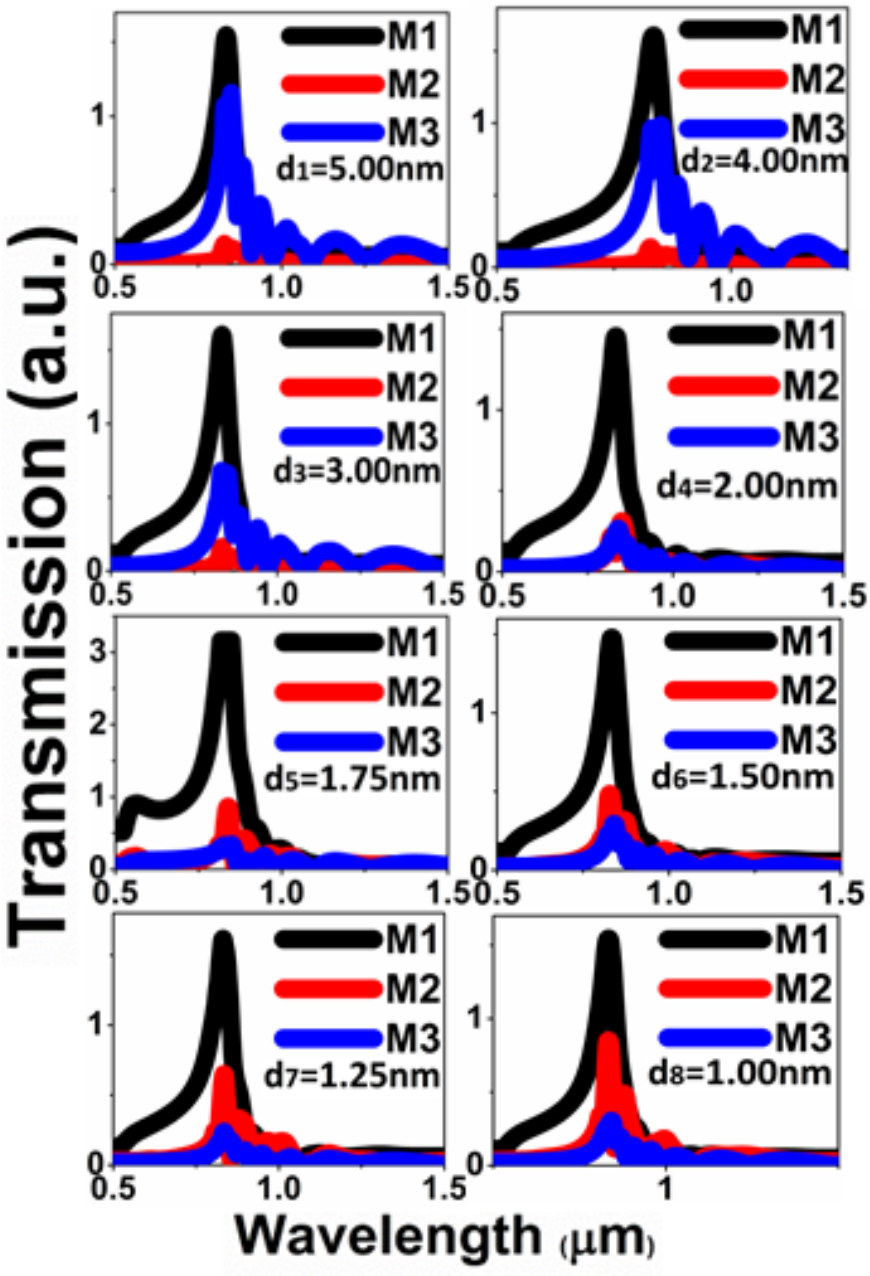

Figure 5.6 (a) to (h) Transmission spectra obtained on monitors M_1 M_2 and M_3 with distance varying from d_1 to d_8 between the nanodisks showing variation of tunnelling efficiency with varying interparticle distance.

Also the electric field profiles for the silver nanodisks dimer system were obtained to understand the field behaviour. Figure 5.4 (b) display the electric field profile of the silver nanodisks dimer demonstrating formation of tunneling zone when the distance between the nanodisks is 1.5nm. Figure 5.7 (a) to (h) display

the electric field profile of the silver nanodisks quantum system demonstrating formation of tunnelling zone when the distance between the nanodisks decreases from d_1 to d_8. When observed carefully it shows a region of high potential when the disks get closer leading to the formation of tunnelling zone thereby encouraging resonant plasmon tunnelling and if the input wavelength is sufficient enough resulting in higher skin depth then tunnelling efficiency is indeed high.

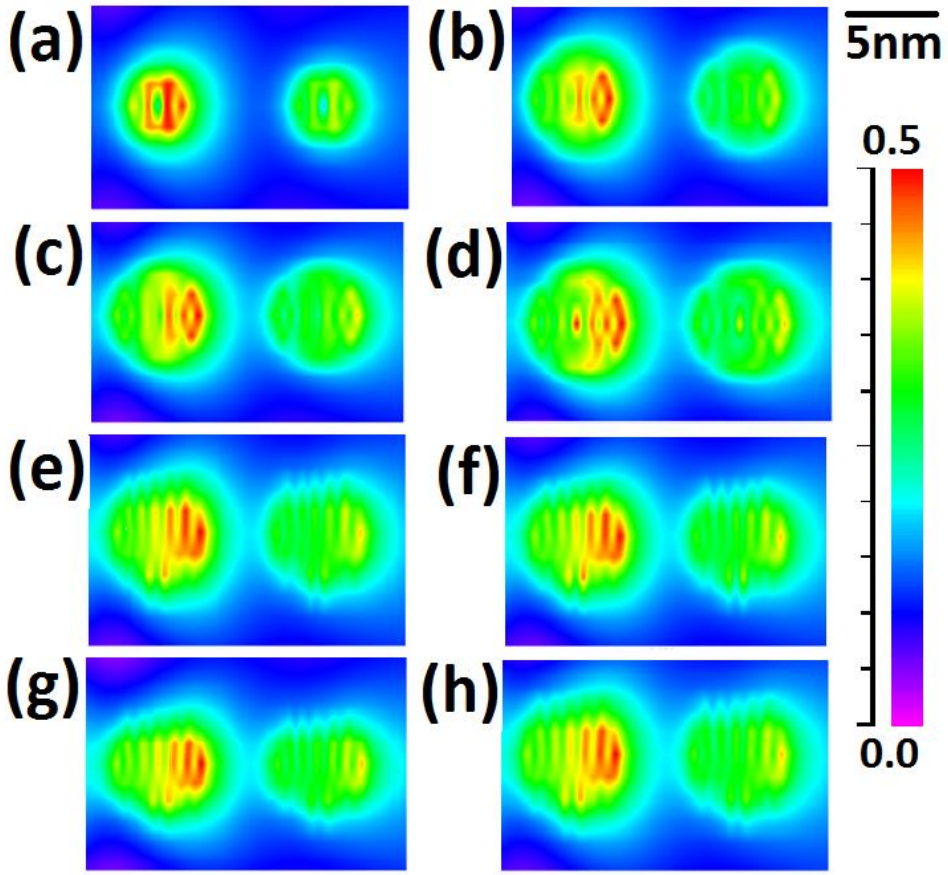

Figure 5.7 (a) to (h) Electric field profile of the silver nanodisks quantum system with varying distance demonstrating formation of tunnelling zone when the distance between the nanodisks decreases from d_1 to d_8.

5.4 Summary

In summary, the proposed gradient potential dependent skin depth theory efficiently describes the tunneling behaviour of resonating plasmons through the

metal nanoparticles system and helps in envisaging the transmission characteristics of the system precisely. It is observed that when the interparticle distance is less than 1.5nm, the system of silver nanodisks dimer exhibit tunneling zone and skin depth plays an important role in resonant plasmon tunnelling mechanism. Appreciably the energy eigen values and corresponding wavelengths are obtained for the dimer system with significant validation with the proposed theory. Hence it is the overall effect of skin depth, gradient potential along with in-phase or out-of-phase interaction, node or anti node formation and the role of distance between the nanodisks that comes as the final output of the tunnelled plasmons. As the advent of nanotechnology brings down the experimental regime to nanoscales, the quantum effects become significant in plasmonic nanostructures. Gradient potential model for plasmonic systems help in appreciating the unique properties exhibited by them. Proposed GPST provides an insight to explore the nano plasmonic system, to apprehend the results hence providing the tool to predict the behaviour of the system under study. It can help to comprehend various resonating plasmons tunnelled systems such as plasmon tunnel diode, plasmonic Josephson junction assisted superconductivity; plasmon tunnelled field-effect transistors etc. significantly improving the performance of integrated circuits.

Chapter 6
Plexcitonic interaction[1,2]

6.1 Introduction

In the previous chapter it is learnt that plasmons tunnel through closely spaced metal nanoparticles and this effect can also contribute when nanostructured metals and semiconductors are layered to form hybrid composites resulting in plexcitonic interactions discussed in this chapter.

Plexcitons are the coupled plasmon-exciton modes having excellent properties leading to potential applications biosensing, surface enhanced spectroscopy, lasing etc. Exciton is a bound state of an electron and hole that are attracted to each other by Coulomb force. An exciton is formed when a photon is absorbed by a semiconductor. It is electrically neutral quasi particle and can transport energy without transporting net electric charge. As discussed in earlier chapters plasmon is a quanta of plasma oscillations that is quanta of collective oscillations of electrons in metals.

Thus, coherently coupled plasmons and excitons give rise to new optical excitations called plexcitons [132]. These strongly interacting plasmons and excitons that is plexcitons can be observed in a system having semiconductor-metal interfaces, composites etc. Numerous systems of metal dielectric hybrid nanostructures forming plexcitonic systems have been examined that exhibit

[1] A part of the results reported in this chapter has been published in conference proceeding as 'Ag-GaAs-Ag quantum nano-lenses system for plexcitonic interaction,' In *Photonics 2014: 12th International Conference on Fiber Optics and Photonics, December 13-16, 2014,* © OSA 2014 (T3A.42). *http://dx.doi.org/10.1364/PHOTONICS.2014.T3A.42*

[2] A part of the results reported in this chapter has been published in conference proceeding as 'Field enhanced plexcitonic coupling between InAs quantum dot and silver film: highly sensitive plasmonic composite,' In *SPIE NanoScience+ Engineering, August 17-21, 2014* (pp. 91630W-91630W). International Society for Optics and Photonics. *http://dx. doi:10.1117/12.2061914*

excellent electromagnetic properties [133-137]. The importance of plexcitonic interactions are discussed below.

6.1.1 Importance of plexcitonic interaction

Through plexcitonic interaction the energy can be transferred resonantly over distances of hundreds of nanometers hence can yield increased propagation length. The linewidth of plasmon modes is larger than the linewidth of excitons which leads to the fact that plasmon lifetime is in femtoseconds as compared to exciton lifetime which is in picosecond.

Therefore, the interaction between the exciton and plasmon modes can be considered as the coupling of a single mode (exciton) to a broader continuum (plasmon) resulting in Fano resonances. In turn Fano resonance has applications in sensing, lasing, switching etc. Thus, plexcitonic interaction will lead to Fano resonance and hence to the applications of Fano resonance

6.2 Plexcitonic structures

6.2.1 Metal/semiconductor/metal nanodisk system

A layered system of silver/gallium arsenide/silver (Ag-GaAs-Ag) is proposed having quantum nano-lenses of GaAs sandwiched between silver nanosdisk forms the plexcitonic system. Hybrid plasmonic band gap is obtained for the same with respect to TE and TM polarization of light. Further a cavity is introduced and its transmission is obtained.

6.2.2 Semiconductor/metal/semiconductor/metal/semiconductor system

Another plasmonic composite comprising of indium arsenide quantum dots on silver film is proposed. The thickness of the silver layer is varied and its effect is studied. Also the depth to which the semiconductor dots are embedded is varied to see its effect on the propagation.

6.3 Silver-Galium Arsenide-Silver nanodisks system

6.3.1 Structure and results

The proposed plexcitonic system comprises of an array of layered Ag-GaAs-Ag in hexagonal arrangement with GaAs quantum nano-disks sandwiched between the two layers of Ag nano-disks as shown in Figure 6.1.

The three layered system of disks touch at the convex edge and are arranged in hexagonal lattice with lattice constant a = 100 nm and radius r = 40 nm. This metal-semiconductor-metal system of nanodisks excite plexcitonic coupling and can have important applications in lasing, nano-antennae, Fano devices etc.

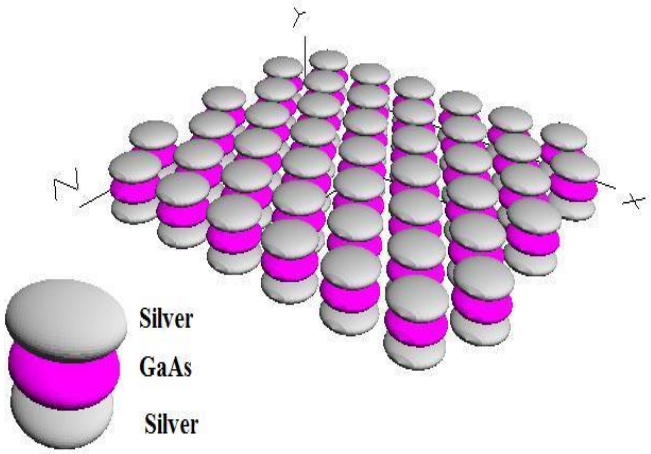

Figure 6.1 Three layered system of Ag-GaAs-Ag nano-disks in hexagonal arrangement.

The proposed system is studied for band gap by using 3D plane wave expansion (PWE) method to get hybrid band structure as given in Figure 6.2. It is observed from Figure 6.2 that the system offers hybrid band structure giving transverse electric (TE-odd parity) and transverse magnetic (TM-even parity) gap in ultraviolet regime of the electromagnetic spectrum. Further, to investigate its optical response, we employ finite difference time domain (FDTD) method. A cavity defect is introduces at the center of the system. Transmission characteristics of the cavity are obtained as given in Figure 6.3 with the monitor value representing the transmission in the graphs. It is observed that for TM wave

(Figure 6.3 the peak value of the cavity is 0.4 (blue curve) with respect to the source with peak value of 0.6 (green curve in *inset*), hence resonating with more than 66%.

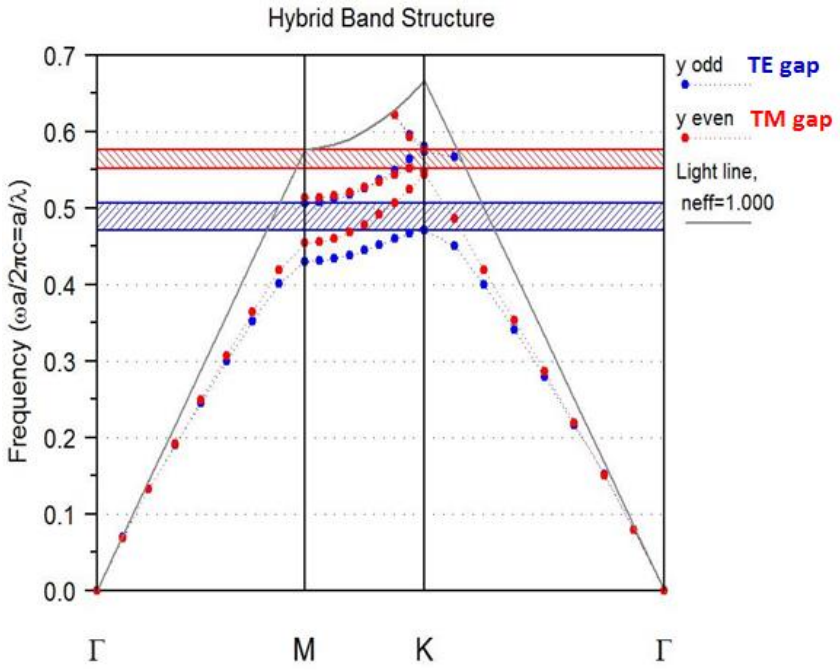

Figure 6.2 Hybrid band structure of the proposed plexcitonic system with odd parity for TE gap and even parity for TM gap.

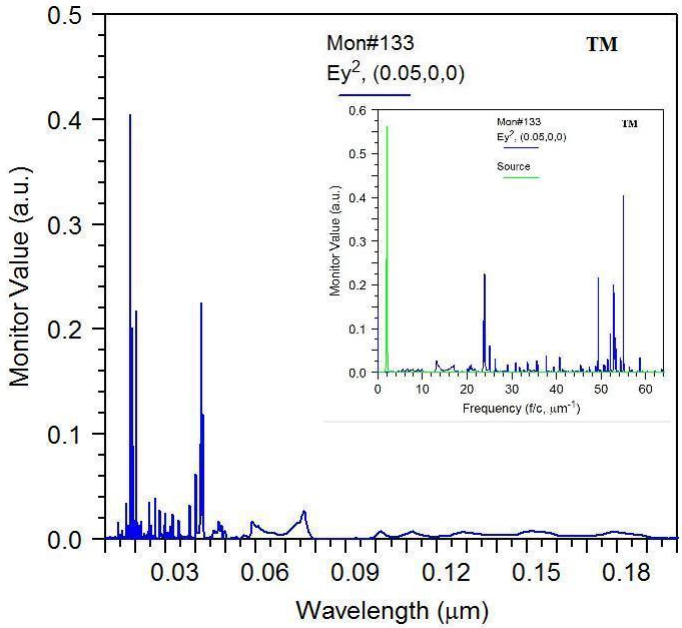

Figure 6.3 Transmission characteristics of the Ag-GaAs-Ag nano-lenses plexcitonic system for TM waves (Monitor value represents transmission).

Contrary to this we observe that for TE wave the peak intensity is very low (Figure 6.4), that is of the order of 10^{-10} and is negligible.

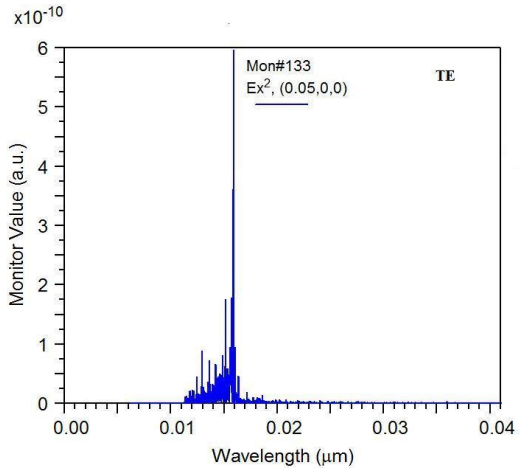

Figure 6.4 Transmission characteristics of the Ag-GaAs-Ag nano-lenses plexcitonic system for TE waves (Monitor value represents transmission).

Although the hybrid band structure (Figure 6.2) reveal gap for TE wave as well, but due to the presence of silver metal nano-lenses, the plexcitonic system enhances the TM mode which is the characteristic property of plasmonic system. This observation was verified by using the optimized value for the input of 193nm (Figure 6.5 (c)) yielding sharp rise for the output signal (blue) with respect to the input (green peak in the inset of Figure 6.5(c) i.e. the system increases the output 10 times.

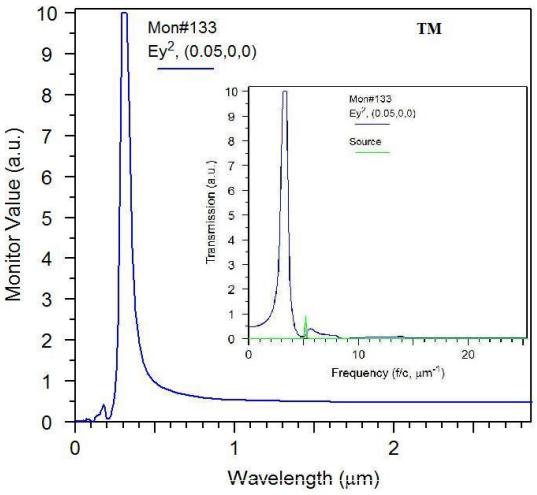

Figure 6.5 Strongly resonating peak is obtained for the input of 193nm with enhanced signal with respect to the input.

The output signal shifts with respect to the input due to the plexcitonic coupling. The 3D contour for electric field Ey, for the cavity defect is given in Figure 6.6 showing strongly confined intense cavity resonance.

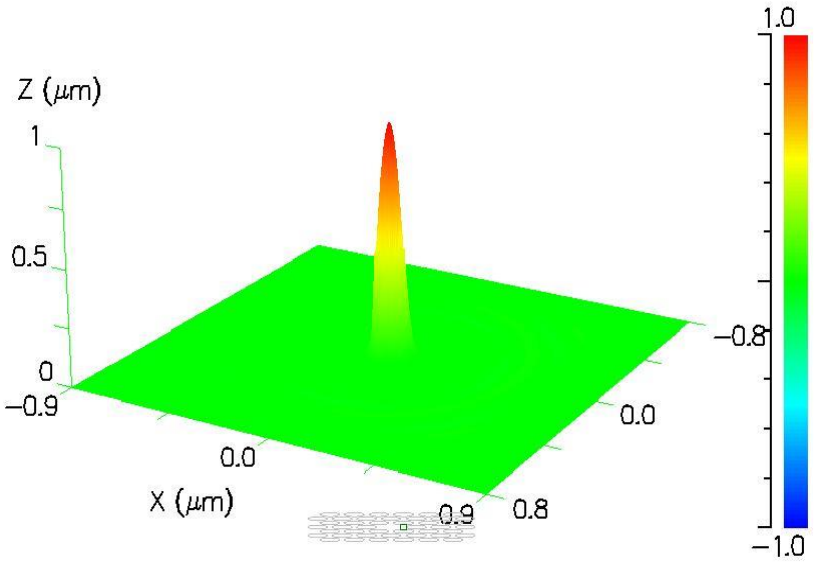

Figure 6.6 3D contour for electric field Ey, for the cavity defect showing strongly confined intense cavity resonance.

6.4 Indium Arsenide – Silver – Silicon – Silver – Indium Arsenide

6.4.1 Structure and results

The proposed system comprises of metal-dielectric-metal etched with indium arsenide, InAs quantum dots as shown in Figure 6.7 (a). The thickness of silver layer is varied and a transmission characteristic of the waveguide is studied.

Another parameter that plays an important role is the depth to which the quantum dots are etched into silver film, as given in Figure 6.7 (b) and (c).

Propagation characteristics of the silver-silicon-silver (Ag-Si-Ag) waveguide are studied as shown in Figure 6.8. It is observed that the intensity of the plasmon propagation decreases as the wave traverses its path.

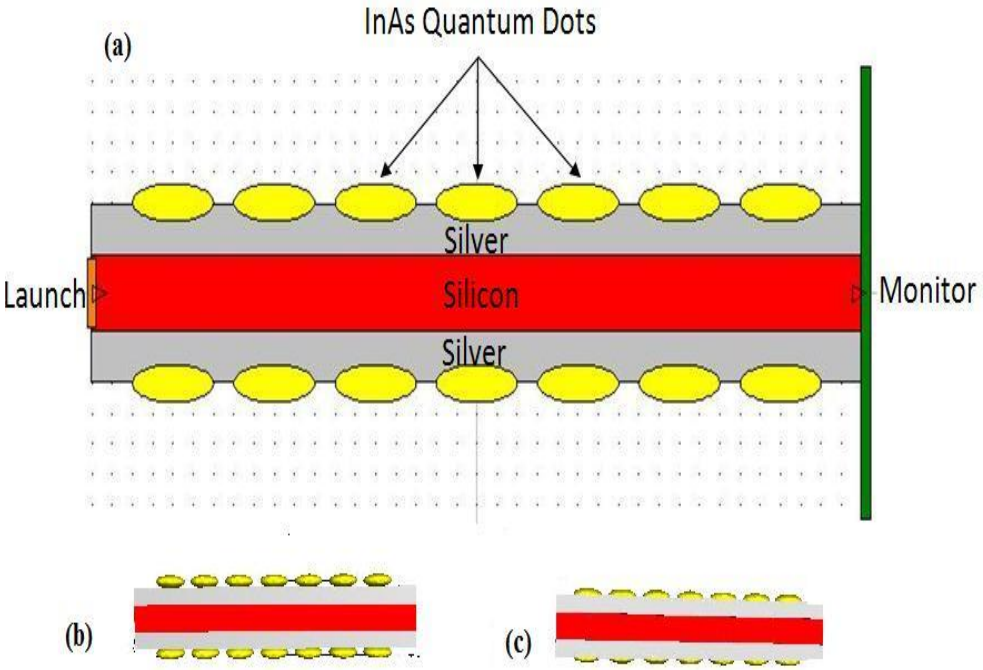

Figure 6.7: Schematic of the proposed structure for plexcitonic waveguide system.

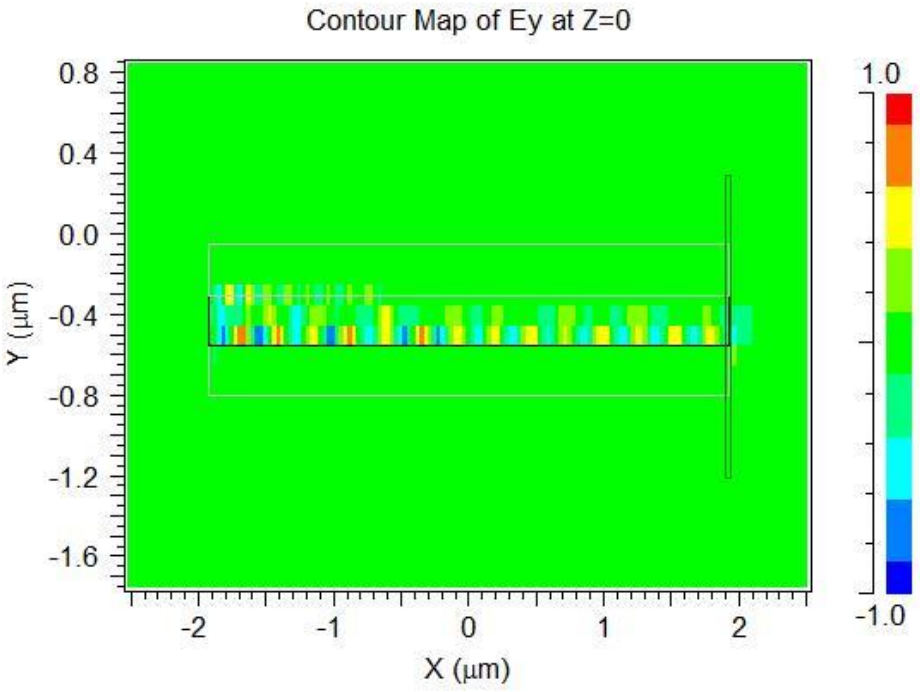

Figure 6.8: Propagation of plasmons through silver-silicon-silver waveguide.

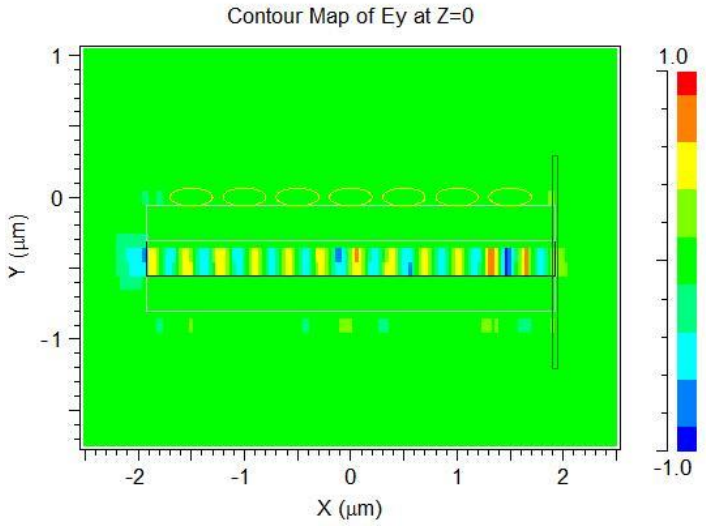

Figure 6.9: Propagation of resultant plexcitons through silver-silicon-silver waveguide with InAs quantum dots on one surface of the proposed system.

Further it is observed that by etching the surface of the top of the silver film by InAs QD, (Figure 6.9) the system results in plexciton propagation through the proposed composite. The propagation length increases in this case but it was observed that the plexciton energy was leaking through the lower layer of silver. This loss was addressed by making the structure symmetrical by etching the lower silver surface by InAs QD as well, see Figure 6.10.

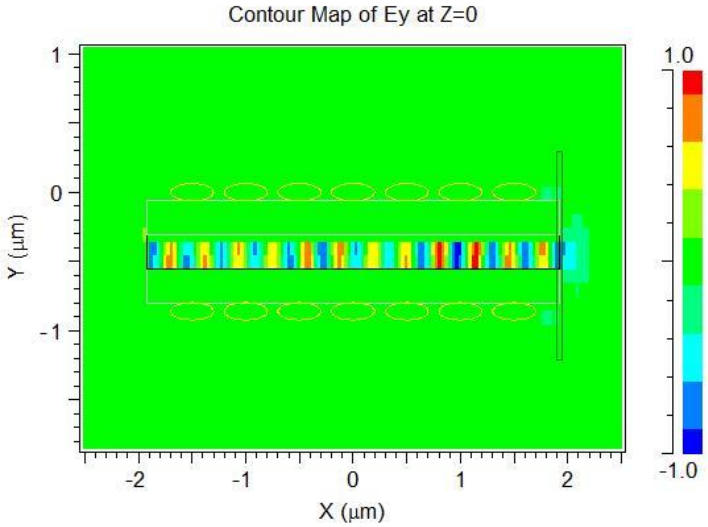

Figure 6.10: Propagation characteristics of the plexcitons through InAs-Ag-Si-Ag-InAs waveguide.

It is observed that the propagation length of the resultant wave decreases when the thickness of the silver film is decreased from 167nm to 55nm as shown in Figure 6.11 (a) and (b) respectively.

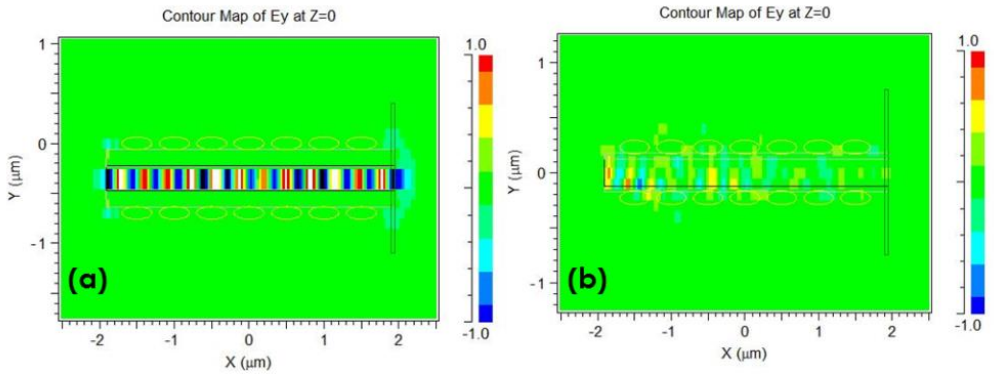

Figure 6.11. (a) and (b) The propagation length of the resultant wave also depends on the thickness of silver film and decreases with decreasing thickness from 167nm to 55nm as given in (a) and (b) respectively.

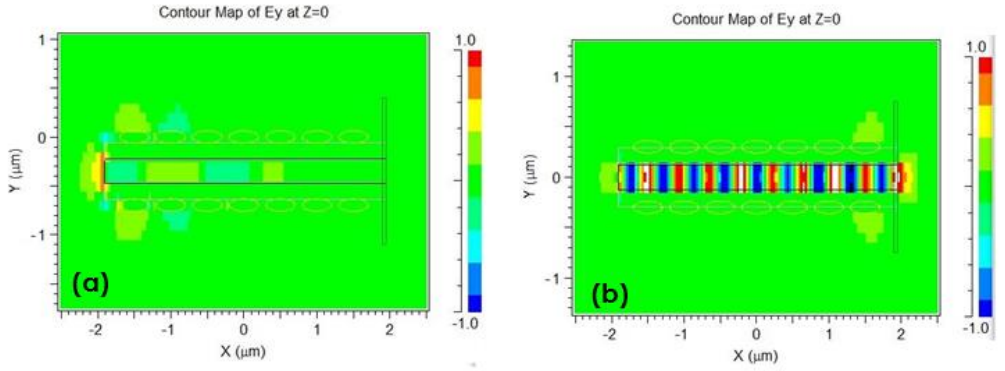

Figure 6.12 (a) and (b) Field enhancement arising due to the coupling of plexcitons between InAs QD with silver film passing through the silicon waveguide depending upon the depth to which QDs are etched into silver. (a) QDs on the surface of silver and (b)QDs etched into silver.

The effects of structural parameters were studied and it was observed that as the QDs were etched into the silver film, the propagating field enhances for the input wavelength of 1.55 μm, given in Figure 6.12 (a) and (b). This field enhancement is due to the plexcitonic coupling between the InAs QD with the silver film propagating through silicon waveguide. Also, we found that

completely embedding the QDs into silver results in abrupt losses which may be due to loss of photon absorption when they are completely inside metal unlike when in insulators.

To study the quantum effects the interparticle separation is decreased to sub-nanodimensions. It is observed that as the distance between the particles decreases, the quantum potential at the surface of each of the particles result in enhanced field between the two particles.

6.5 Summary

In this chapter different plexcitonic structures have been proposed. At first a multi-layered Ag-GaAs-Ag quantum nano-lenses plexcitonic system is proposed that results in strongly confined and enhanced resonance for cavity defect. Hence the system has applications in lasing, switching, sensing etc. As the cavity mode resonates in ultra-violet regime, it can be an alternative for excimer lasers. Further, a system of InAs QDs-Ag-Si-Ag-InAs QDs results in as excellent plexcitonic system resulting in ultra high local field enhancement at the interface whereas the energy propagates longitudinally due to resonating quantum plasmonic tunnelling. The system has applications in sensing, solar cells, lasing etc.

Chapter 7
Summary and future scope

7.1 Summary

The work carried out in this thesis is summarized here as it facilitates how to reach out to an ever-increasing need for strong confinement of light with larger propagation lengths and low losses. Closely spaced periodic array of silver nanoparticles embedded on silicon-on-insulator substrate yields a novel method for strong confinement of light with low losses for plasmon propagation through these plasmonic waveguides.

Silver nanorods array palisading silicon to form core of SOI waveguide is theoretically modelled. Proposed geometry serves as the basis waveguide for different devices such as straight waveguide, bend design, y-splitters. Propagation characteristics of the waveguide expose plasmonic bandgap in the visible regime. Basis waveguide exhibit low-loss propagation, larger propagation length and strong confinement of the traversing plasmonic mode.

The periodic arrangement of metal nanoparticles give rise to surface plasmon polariton band gap (SPPBG) effect. The SPPBG effect allows lossless plasmon propagation whereas SOI substrate renders transverse confinement and use of metal nanoparticles result in local field enhancement that assist plasmon amplification.

The basis geometry exhibiting SPPBG effect is further used to devise plasmonic Mach-Zehnder interferometer (PMZI) for refractive index sensing with applications in sorting and classification of different types of cancer cells. PMZI is analyzed for its potential in sensing, intended for cancer therapy. SOI substrate grants strong spatial confinement and assist waveguidance to the propagating plasmon mode due to the SPPBG effect. This arrayed system triggers local field

enhancement promoting sensing proficiency of the device and is assessed in terms of wavelength and phase shift. Phase shift obtained for the breast adenocarcinoma and blood cancer cell lines read very high value to identify extremely small changes in refractive index of the analyte. Figure of merit calculated thereby expose impressive device performance outdoing preceding plasmonic sensors leading to validation of proposed ultra-compact sensitive PMZI design.

In addition, it is observed that the geometry of metal nanoparticles control the plasmon resonance. Silver ellipsoidal plasmonic crystal cavity exhibit enhanced Fano resonance with applications in switching and lasing. Enhancement in the asymmetric line shape of Fano resonance is observed and extensively examined for cavities in plasmonic crystals of ellipsoidal silver nanoparticles with hexagonal arrangement. Scattering models for ellipsoidal and cylindrical nanoparticles are compared and it is found that the spectral interference between the cavity mode and the background scattering mode results in a sharp asymmetric peak, which is the defining characteristic of Fano resonance. The cavity in ellipsoidal nanoparticles yields high transmission. Higher harmonic generation is also observed, which confirms the ultrahigh cavity response in ellipsoidal nanoparticles. The effect of power variation on the Fano resonance profile is described, and its application in the field of switching is explored. The extraordinary rise in asymmetric line shapes of the Fano resonance promises profound applications in the field of sensing, switching and lasing devices.

Another important effect studied in this thesis is the quantum resonant plasmon tunnelling in silver nanodisk dimer system. The region between adjacent silver nanodisks at sub-nanometer spacing, exhibit gradient potential due to the property of its geometry leading to the formation of tunnelling zone and is substantiated by finite difference time domain computational method. Significantly, the energy eigen values and hence the wavelength eigen values are obtained for the quantum system of silver nanodisk dimer. Incident wavelength influences the skin depth, which along with local enhanced field around each

nanoparticle assists quantum plasmonic resonant tunnelling. The proposed gradient potential skin depth theory can be used to predict the performance of plasmon tunnel diode, plasmon tunnelled field-effect transistors, plasmonic Josephson junction assisted superconductivity etc.

Furthermore, a plexcitonic system is formed by multi-layered silver-gallium arsenide-silver (Ag-GaAs-Ag) quantum nano-lenses and various optical properties using finite difference time domain method are studied. Interaction between plasmons and excitons from semiconductor quantum dots (QDs) give rise to plexcitons which results in enhanced emission, allowing controlled energy transfer and can also modify spontaneous emission in QDs. Plane wave expansion method reveals hybrid band-structure in the ultraviolet regime of the electromagnetic spectrum. Proposed metal-semiconductor-metal system of quantum nano-lenses excite plexcitonic coupling and have important applications in lasing, nano-antennae, Fano devices etc. Cavity defect support strongly confined mode. As the cavity mode resonates in ultra-violet regime, it can be an alternative for excimer lasers. Further, a system of InAs QDs-Ag-Si-Ag-InAs QDs results in an excellent plexcitonic system resulting in ultra high local field enhancement at the interface whereas the energy propagates longitudinally due to resonating quantum plasmonic tunnelling. The system has applications in sensing, solar cells, lasing etc.

7.2 Scope for future work

In view of the above studies it would be interesting to carry out the following studies:

- Metal nanoparticles yield plasmonic band gap and thus can be exploited and tailored in varied fashion to obtain desired results. Their resonance can concede numerous applications.
- Surface plasmon polariton band gap effect based devices can be designed that will allow manipulation of light of desired frequencies.

- Plexcitonic composites of different permutations can be further studied for different applications.
- Plexcitonic interaction with varying distance between the particles can be studied as the quantum potential at the surface of each of the particles result in enhanced field between the two particles and hence the increased sensitivity.

References

1. Wood, R. W. "XLII. On a remarkable case of uneven distribution of light in a diffraction grating spectrum." *The London, Edinburgh, and Dublin Philosophical Magazine and Journal of Science* **4**, 396-402 (1902).
2. Wood, R. W. "XXVII. Diffraction gratings with controlled groove form and abnormal distribution of intensity." *The London, Edinburgh, and Dublin Philosophical Magazine and Journal of Science* **23**,310-317 (1912).
3. Rayleigh, Lord. "On the dynamical theory of gratings." *Proceedings of the Royal Society of London. Series A, Containing Papers of a Mathematical and Physical Character* **79**, 399-416 (1907).
4. Bohm, D., and Pines, D. "A collective description of electron interactions. I. Magnetic interactions." *Physical Review* **82** 625 (1951).
5. Pines, D., and Bohm, D. "A collective description of electron interactions: II. Collective vs individual particle aspects of the interactions." *Physical Review* **85**, 338 (1952).
6. Bohm, D., and Pines, D. "A collective description of electron interactions: III. Coulomb interactions in a degenerate electron gas." *Physical Review* **92**, 609 (1953).
7. Pines, D. "A collective description of electron interactions: IV. Electron interaction in metals." *Physical Review* **92**, 626 (1953).
8. Ritchie, R. H. "Plasma losses by fast electrons in thin films." Physical Review **106**, 874 (1957).
9. Kretschmann, E., and Raether, H. "Notizen: Radiative Decay of Non Radiative Surface Plasmons Excited by Light." *Zeitschrift für Naturforschung A* **23**, 2135-2136 (1968).

10. Otto, A. "Excitation of nonradiative surface plasma waves in silver by the method of frustrated total reflection." *Zeitschrift für Physik* **216**, 398-410 (1968).
11. Liedberg, B., Nylander, C., and Lunström, I. "Surface plasmon resonance for gas detection and biosensing." *Sensors and actuators* **4**, 299-304 (1983).
12. Cullen, D. C., Brown, R. G. W., and Lowe, C. R. "Detection of immuno-complex formation via surface plasmon resonance on gold-coated diffraction gratings." *Biosensors* **3**, 211-225 (1988).
13. Jory, M. J., Bradberry, G. W., Cann, P. S., and Sambles, J. R. "A surface-plasmon-based optical sensor using acousto-optics." *Measurement Science and Technology* **6,** 1193 (1995).
14. Lawrence, C. R., Geddes, N. J., Furlong, D. N., Sambles, J. R. "Surface plasmon resonance studies of immunoreactions utilizing disposable diffraction gratings." *Biosensors and Bioelectronics* **11**, 389-400 (1996).
15. Pockrand, I., Swalen, J. D., Gordon, J. G., and Philpott, M. R. "Surface plasmon spectroscopy of organic monolayer assemblies." Surface Science **74,** 237-244 (1978).
16. Liedberg, B., Lundström, I., and Stenberg, E. "Principles of biosensing with an extended coupling matrix and surface plasmon resonance." *Sensors and Actuators B: Chemical* **11,** 63-72 (1993).
17. Zhang, L-M., and Uttamchandani. D,. "Optical chemical sensing employing surface plasmon resonance." *Electronics Letters* **24**, 1469-1470 (1988).
18. Striebel, C., Brecht, A., and Gauglitz, G., "Characterization of bio-membranes by spectral ellipsometry, surface plasmon resonance and interferometry with regard to biosensor application." *Biosensors and Bioelectronics* **9**, 139-146 (1994).
19. Maier, Stefan Alexander. *Plasmonics: fundamentals and applications*. Springer Science and Business Media, (2007).

20. Raether, Heinz. *Surface plasmons on smooth surfaces*. Springer Berlin Heidelberg, (1988).
21. Barnes, W. L., Dereux, A. and Ebbesen, T. W., "Surface plasmon subwavelength optics." *Nature* **424**, 824-830 (2003).
22. Barnes, W. L., "Surface plasmon polariton length scales: a route to subwavelength optics." *Journal of Optics A: Pure and Applied Optics* **8**, S87 (2006).
23. Yao, K, and Liu, Y., "Plasmonic metamaterials." *Nanotechnology Reviews* **3**, 117-210 (2014).
24. Atwater, H. A., "The promise of plasmonics." *Scientific American* **296**, 56-62 (2007).
25. Schuller, J. A., Barnard, E. S., Cai, W., Jun, Y. C., White, J. S., and Brongersma, M. L., "Plasmonics for extreme light concentration and manipulation." *Nature materials* **9**, 193-204 (2010).
26. Lindquist, N. C., Nagpal, P., Lesuffleur, A., Norris, D. J., and Oh, S. H., "Three-dimensional plasmonic nanofocusing." *Nano letters* **10**. 1369-1373 (2010).
27. Cai, W., White, J. S., and Brongersma, M. L. "Compact, high-speed and power-efficient electrooptic plasmonic modulators." Nano letters **9**, 4403-4411 (2009).
28. Caulfield, H. J., and Dolev, S. "Why future supercomputing requires optics." *Nature Photonics* **4**, 261-263 (2010).
29. Dionne, J., Sweatlock, L. A., Sheldon, M. T., Alivisatos, A. P., and Atwater, H. A., "Silicon-based plasmonics for on-chip photonics." *Selected Topics in Quantum Electronics, IEEE Journal of* **16,** 295-306 (2010).
30. Anker, J. N., Hall, W. P., Lyandres, O., Shah, N. C., Zhao, J., and Van Duyne, R. P., "Biosensing with plasmonic nanosensors." *Nature materials* **7**, 442-453 (2008).
31. Adato, R., Yanik, A. A., Amsden, J. J., Kaplan, D. L., Omenetto, F. G., Hong, M. K.,Erramilli, S and Altug, H., "Ultra-sensitive vibrational

spectroscopy of protein monolayers with plasmonic nanoantenna arrays." *Proceedings of the National Academy of Sciences* **106**, 19227-19232 (2009).

32. Alù, A., and Engheta, N. "Multifrequency optical invisibility cloak with layered plasmonic shells." *Physical review letters* **100**, 113901 (2008).
33. Renger, J., Kadic, M., Dupont, G., Aćimović, S. S., Guenneau, S., Quidant, R., and Enoch, S. "Hidden progress: broadband plasmonic invisibility." *Optics Express* **18**, 15757-15768 (2010).
34. Alu, A, and Engheta, N. "Plasmonic and metamaterial cloaking: physical mechanisms and potentials." *Journal of Optics A: Pure and Applied Optics* **10**, 093002 (2008).
35. Maier, S. A., and Atwater, H. A., "Plasmonics: Localization and guiding of electromagnetic energy in metal/dielectric structures." *Journal of Applied Physics* **98**, 011101 (2005).
36. Ozbay, E., "Plasmonics: merging photonics and electronics at nanoscale dimensions." *science* **311**, 189-193(2006).
37. Dionne, J. A., Sweatlock, L. A., Atwater, H. A., and Polman, A., "Plasmon slot waveguides: Towards chip-scale propagation with subwavelength-scale localization." *Physical Review B* **73**,035407 (2006).
38. Politi, A., Cryan, M. J., Rarity, J. G., Yu, S., and O'Brien, J. L., "Silica-on-silicon waveguide quantum circuits." Science **320**, 646-649 (2008).
39. Law, M., Sirbuly, D. J., Johnson, J. C., Goldberger, J., Saykally, R. J., and Yang, P."Nanoribbon waveguides for subwavelength photonics integration." *Science* **305**, 1269-1273 (2004).
40. Stipe, B. C, Strand1, T.C., Poon, C. C, Balamane, H., Boone, T. D., Katine, J. A., Li, J., Rawat, V., Nemoto, H., Hirotsune, A., Hellwig1,O., Ruiz, R., Dobisz, E., Kercher D. S., Robertson, N., Albrecht, T. R., and Terris, B. D.,. "Magnetic recording at 1.5 Pb m− 2 using an integrated plasmonic antenna." *Nature Photonics* **4**, 484-488 (2010).

41. Sivis, M., Duwe, M., Abel, B., and Ropers, C. "Extreme-ultraviolet light generation in plasmonic nanostructures." *Nature Physics* **9**, 304-309 (2013).
42. Haes, A. J., Haynes, C. L., McFarland, A. D., Schatz, G. C., Van Duyne, R. P., and Zou, S., "Plasmonic materials for surface-enhanced sensing and spectroscopy." *Mrs Bulletin* **30**, 368-375 (2005).
43. Xu, T., Wu, Y. K., Luo, X., and Guo, L. J. "Plasmonic nanoresonators for high-resolution colour filtering and spectral imaging." *Nature Communications* **1,** 59 (2010).
44. Pala, R. A., Shimizu, K. T., Melosh, N. A., and Brongersma, M. L."A nonvolatile plasmonic switch employing photochromic molecules." *Nano letters* **8**, 1506-1510 (2008).
45. Aydin, K., Ferry, V. E., Briggs, R. M., and Atwater, H. A., "Broadband polarization-independent resonant light absorption using ultrathin plasmonic super absorbers." *Nature communications* **2**, 517 (2011).
46. Stewart, M. E., Anderton, C. R., Thompson, L. B., Maria, J., Gray, S. K., Rogers, J. A., and Nuzzo, R. G. "Nanostructured plasmonic sensors." *Chemical reviews* **108**, 494-521 (2008).
47. Feng, J., Siu, V. S., Roelke, A., Mehta, V., Rhieu, S. Y., Palmore, G. T. R., and Pacifici, D."Nanoscale plasmonic interferometers for multispectral, high-throughput biochemical sensing." *Nano letters* **12**, 602-609 (2012).
48. Zia, R., Schuller, J. A., Chandran, A., and Brongersma, M. L.,"Plasmonics: the next chip-scale technology." *Materials today* **9**, 20-27 (2006).
49. Ozbay, E., "Plasmonics: merging photonics and electronics at nanoscale dimensions." *Science* **311**, 189-193 (2006).
50. Ebbesen, T. W., Lezec, H. J., Ghaemi, H. F., Thio, T., and Wolff, P. A.,"Extraordinary optical transmission through sub-wavelength hole arrays." *Nature* **391**, 667-669 (1998).

51. Thio, T., Pellerin, K. M., Linke, R. A., Lezec, H. J., and Ebbesen, T. W. "Enhanced light transmission through a single subwavelength aperture." *Optics Letters* **26**, 1972-1974 (2001).
52. Jain, P. K., and El-Sayed, M. A. "Plasmonic coupling in noble metal nanostructures." *Chemical Physics Letters* **487**, 153-164 (2010).
53. Knight, M. W., Grady, N. K., Bardhan, R., Hao, F., Nordlander, P., and Halas, N. J. "Nanoparticle-mediated coupling of light into a nanowire." *Nano Letters* **7**, 2346-2350 (2007).
54. Ferry, V. E., Sweatlock, L. A., Pacifici, D., and Atwater, H. A. "Plasmonic nanostructure design for efficient light coupling into solar cells." *Nano letters* **8**, 4391-4397 (2008).
55. Anker, J. N., Hall, W. P., Lyandres, O., Shah, N. C., Zhao, J., and Van Duyne, R. P. "Biosensing with plasmonic nanosensors." *Nature materials* **7**, 442-453 (2008).
56. Stewart, M. E., Anderton, C. R., Thompson, L. B., Maria, J., Gray, S. K., Rogers, J. A., and Nuzzo, R. G. "Nanostructured plasmonic sensors." *Chemical reviews* **108**, 494-521 (2008).
57. Willets, K.A., and Van Duyne, R. P., "Localized surface plasmon resonance spectroscopy and sensing." *Annu. Rev. Phys. Chem.* **58**, 267-297 (2007).
58. Grande, M., Vincenti, M. A., Stomeo, T., Morea, G., Marani, R., Marrocco, V., .. and Scalora, M. "Experimental demonstration of a novel bio-sensing platform via plasmonic band gap formation in gold nano-patch arrays." *Optics Express* **19**, 21385-21395 (2011).
59. Stiles, P. L., Dieringer, J. A., Shah, N. C., and Van Duyne, R. P. "Surface-enhanced Raman spectroscopy." *Annu. Rev. Anal. Chem.* **1**, 601-626 (2008).
60. Moskovits, M., "Surface-enhanced Raman spectroscopy: a brief retrospective." *Journal of Raman Spectroscopy* **36**, 485-496 (2005).

61. Nie, S., and Emory, S. R. "Probing single molecules and single nanoparticles by surface-enhanced Raman scattering." *Science* **275**, 1102-1106 (1997).
62. Barhoumi, A., Zhang, D., Tam, F., and Halas, N. J. "Surface-enhanced Raman spectroscopy of DNA." *Journal of the American Chemical Society* **130**, 5523-5529 (2008).
63. Giannini, V., Fernández-Domínguez, A. I., Heck, S. C., and Maier, S. A. "Plasmonic nanoantennas: fundamentals and their use in controlling the radiative properties of nanoemitters." *Chemical Reviews* **111**, 3888-3912 (2011).
64. Novotny, L., Bian, R. X., and Xie, X. S., "Theory of nanometric optical tweezers." *Physical Review Letters* **79**, 645 (1997).
65. Fang, N., Lee, H., Sun, C., and Zhang, X. "Sub–diffraction-limited optical imaging with a silver superlens." *Science* **308**, 534-537 (2005).
66. Liu, Z., Lee, H., Xiong, Y., Sun, C., and Zhang, X. "Far-field optical hyperlens magnifying sub-diffraction-limited objects." *Science* **315**, 1686-1686 (2007).
67. Lal, S., Clare, S. E., and Halas, N. J."Nanoshell-enabled photothermal cancer therapy: impending clinical impact." *Accounts of chemical research* **41**, 1842-1851 (2008).
68. Maier, S. A., Brongersma, M. L., Kik, P. G., Meltzer, S., Requicha, A. A., and Atwater, H. A. "Plasmonics—a route to nanoscale optical devices." *Advanced Materials* 13, 1501-1505 (2001).
69. Guo, X., Qiu, M., Bao, J., Wiley, B. J., Yang, Q., Zhang, X., .. and Tong, L. "Direct coupling of plasmonic and photonic nanowires for hybrid nanophotonic components and circuits." *Nano letters* **9**, 4515-4519 (2009).
70. Zia, R., Selker, M. D., Catrysse, P. B., and Brongersma, M. L. "Geometries and materials for subwavelength surface plasmon modes." *JOSA A* **21**, 2442-2446 (2004).

71. Holmgaard, T., Bozhevolnyi, S. I., Markey, L., and Dereux, A. "Dielectric-loaded surface plasmon-polariton waveguides at telecommunication wavelengths: Excitation and characterization." *Applied Physics Letters* **92**, 11124-11124 (2008).
72. Huang, C. C., "Hybrid plasmonic waveguide comprising a semiconductor nanowire and metal ridge for low-loss propagation and nanoscale confinement." *Selected Topics in Quantum Electronics, IEEE Journal of* **18**, 1661-1668 (2012).
73. Dai, D., and He, S."A silicon-based hybrid plasmonic waveguide with a metal cap for a nano-scale light confinement." *Optics Express* **17**, 16646-16653 (2009).
74. Maier, S. A., "Plasmonics: Metal nanostructures for subwavelength photonic devices." *Selected Topics in Quantum Electronics, IEEE Journal of* **12**, 1214-1220 (2006).
75. Javey, A, and Hongjie D., "Regular arrays of 2 nm metal nanoparticles for deterministic synthesis of nanomaterials." *Journal of the American Chemical Society* 127, 11942-11943 (2005).
76. Boltasseva, A., and Shalaev, V. M., "Fabrication of optical negative-index metamaterials: Recent advances and outlook." *Metamaterials* **2,** 1-17 (2008).
77. Hulteen, J. C., Treichel, D. A., Smith, M. T., Duval, M. L., Jensen, T. R., and Van Duyne, R. P."Nanosphere lithography: size-tunable silver nanoparticle and surface cluster arrays." *The Journal of Physical Chemistry B* **103**, 3854-3863 (1999).
78. Drezet, A., Koller, D., Hohenau, A., Leitner, A., Aussenegg, F. R., andKrenn, J. R.. "Plasmonic crystal demultiplexer and multiports." *Nano letters* **7**, 1697-1700 (2007).
79. Malyarchuk, V., Hua, F., Mack, N., Velasquez, V., White, J., Nuzzo, R., and Rogers, J. "High performance plasmonic crystal sensor formed by soft nanoimprint lithography." *Optics Express* **13**, 5669-5675 (2005).

80. Johnson, P.B., and Christy, R. W., "Optical constants of the noble metals." *Physical Review B* 6, 4370 (1972).
81. Atwater, H. A., and Polman, A., "Plasmonics for improved photovoltaic devices." *Nature materials* **9**, 205-213 (2010).
82. Sanders, A. W., Routenberg, D. A., Wiley, B. J., Xia, Y., Dufresne, E. R., and Reed, M. A.. "Observation of plasmon propagation, redirection, and fan-out in silver nanowires." *Nano letters* **6**, 1822-1826 (2006).
83. Pile, D. F., Ogawa, T., Gramotnev, D. K., Okamoto, T., Haraguchi, M., Fukui, M., and Matsuo, S., "Theoretical and experimental investigation of strongly localized plasmons on triangular metal wedges for subwavelength waveguiding." *Applied Physics Letters* **87**, 061106 (2005).
84. Gramotnev, D. K., and Bozhevolnyi, S. I. "Plasmonics beyond the diffraction limit." *Nature photonics* 4, 83-91 (2010).
85. Oulton, R. F., Sorger, V. J., Genov, D. A., Pile, D. F. P., andZhang, X. "A hybrid plasmonic waveguide for subwavelength confinement and long-range propagation." *Nature Photonics* 2, 496-500 (2008).
86. Ymeti, A., Greve, J., Lambeck, P. V., Wink, T., van Hövell, S. W., Beumer, T. A., ... and Kanger, J. S. "Fast, ultrasensitive virus detection using a Young interferometer sensor." *Nano Letters* **7**, 394-397 (2007).
87. Hua, P., Luff, B. J., Quigley, G. R., Wilkinson, J. S., & Kawaguchi, K.. "Integrated optical dual Mach–Zehnder interferometer sensor." *Sensors and Actuators B: Chemical* **87**, 250-257 (2002).
88. Wu, S. Y., Ho, H. P., Law, W. C., Lin, C., and Kong, S. K. "Highly sensitive differential phase-sensitive surface plasmon resonance biosensor based on the Mach–Zehnder configuration." *Optics Letters* **29**, 2378-2380 (2004).
89. Gao, Y., Gan, Q., Xin, Z., Cheng, X., and Bartoli, F. J. "Plasmonic Mach–Zehnder interferometer for ultrasensitive on-chip biosensing." *ACS nano* **5**, 9836-9844 (2011).

90. Bozhevolnyi, S. I., Volkov, V. S., Devaux, E., Laluet, J. Y., and Ebbesen, T. W. "Channel plasmon subwavelength waveguide components including interferometers and ring resonators." *Nature* **440**, 508-511 (2006).
91. Wahsheh, R. A., Lu, Z., and Abushagur, M. A. "Nanoplasmonic directional couplers and Mach–Zehnder interferometers." *Optics Communications* **282**, 4622-4626 (2009).
92. Pu, M., Yao, N., Hu, C., Xin, X., Zhao, Z., Wang, C., and Luo, X. "Directional coupler and nonlinear Mach-Zehnder interferometer based on metal-insulator-metal plasmonic waveguide." *Optics Express* **18**, 21030-21037 (2010).
93. Bozhevolnyi, S. I., Erland, J., Leosson, K., Skovgaard, P. M., and Hvam, J. M "Waveguiding in surface plasmon polariton band gap structures." *Physical review letters* **86**, 3008 (2001).
94. Drezet, A., Hohenau, A., Stepanov, A. L., Ditlbacher, H., Steinberger, B., Aussenegg, F. R. and Krenn, J. R. "Surface plasmon polariton Mach–Zehnder interferometer and oscillation fringes." *Plasmonics* **1**, 141-145 (2006).
95. Lal, S., Link, S., and Halas, N. J. "Nano-optics from sensing to waveguiding." *Nature photonics* **1**, 641-648 (2007).
96. Kim, D. S., Hohng, S. C., Malyarchuk, V., Yoon, Y. C., Ahn, Y. H., Yee, K. J., and Lienau, C"Microscopic origin of surface-plasmon radiation in plasmonic band-gap nanostructures." *Physical review letters* **91**, 143901-143901 (2003).
97. Choi, W. J., Jeon, D. I., Ahn, S. G., Yoon, J. H., Kim, S., and Lee, B. H., "Full-field optical coherence microscopy for identifying live cancer cells by quantitative measurement of refractive index distribution." *Optics express* **18**, 23285-23295 (2010).
98. Liang, X. J., Liu, A. Q., Lim, C. S., Ayi, T. C., & Yap, P. H., "Determining refractive index of single living cell using an integrated microchip." *Sensors and Actuators A: Physical* **133**,349-354 (2007).

99. Backman, V., Wallace, M. B., Perelman, L. T., Arendt, J. T., Gurjar, R., Müller, M. G., ... and Feld, M. S., "Detection of preinvasive cancer cells." *Nature* **406**, 35-36 (2000).

100. Song, W. Z., Zhang, X. M., Liu, A. Q., Lim, C. S., Yap, P. H., & Hosseini, H. M. M., "Refractive index measurement of single living cells using on-chip Fabry-Perot cavity." *Applied physics letters* **89,**.203901 (2006).

101. Lue, N., Popescu, G., Ikeda, T., Dasari, R. R., Badizadegan, K., and Feld, M. S., "Live cell refractometry using microfluidic devices." *Optics letters* **31**, 2759-2761 (2006).

102. Anker, J. N., Hall, W. P., Lyandres, O., Shah, N. C., Zhao, J., and Van Duyne, R. P "Biosensing with plasmonic nanosensors." *Nature materials* **7**, 442-453 (2008).

103. Homola, J., Yee, S. S., and Gauglitz, G. "Surface plasmon resonance sensors: review." *Sensors and Actuators B: Chemical* **54**, 3-15 (1999).

104. H. J. Park, M. Kang and L. J. Guo, "Large area high density sub-20nm SiO2 nanostructures fabricated by block copolymer template for nanoimprint lithography," ACS Nano **3**, 2601-2608 (2009)

105. L. J. Guo, "Nanoimprint lithography: Methods and material requirements," Adv. Mat. **19**, 495-513 (2007)

106. Park, H. J., Kang, M. G., and Guo, L. J., "Large area high density sub-20 nm SiO2 nanostructures fabricated by block copolymer template for nanoimprint lithography." Acs Nano **3**, 2601-2608 (2009).

107. Liang, X. J., Liu, A. Q., Lim, C. S., Ayi, T. C., and Yap, P. H.. "Determining refractive index of single living cell using an integrated microchip." *Sensors and Actuators A: Physical* **133**, 349-354 (2007).

108. Fano, U. "Effects of configuration interaction on intensities and phase shifts." *Physical Review* **124**, 1866 (1961).

109. Luk'yanchuk, B., Zheludev, N. I., Maier, S. A., Halas, N. J., Nordlander, P., Giessen, H., and Chong, C. T., "The Fano resonance in

plasmonic nanostructures and metamaterials." *Nature materials* **9**, 707-715 (2010).

110. Miroshnichenko, A. E., Flach, S., and Kivshar, Y. S., "Fano resonances in nanoscale structures." *Reviews of Modern Physics* **82**, 2257 (2010).

111. Gallinet, B., and Martin, O. J., "Influence of electromagnetic interactions on the line shape of plasmonic Fano resonances." *ACS nano* **5**, 8999-9008 (2011).

112. Fan, J. A., Bao, K., Wu, C., Bao, J., Bardhan, R., Halas, N. J., and Capasso, F. "Fano-like interference in self-assembled plasmonic quadrumer clusters." *Nano letters* **10**, 4680-4685 (2010).

113. Bohren, C. F. and Huffman, D. R., Wiley-Interscience Publications (1998)

114. Wu, D., Jiang, S., and Liu, X. "Fano-like resonances in asymmetric homodimer of gold elliptical nanowires." *The Journal of Physical Chemistry C* **116**, 13745-13748 (2012).

115. Fan, J. A., Wu, C., Bao, K., Bao, J., Bardhan, R., Halas, N. J., and Capasso, F., "Self-assembled plasmonic nanoparticle clusters." *Science* **328**, 1135-1138 (2010)

116. Gallinet, B., and Martin, O. J., "Ab initio theory of Fano resonances in plasmonic nanostructures and metamaterials." *Physical Review B* **83**, 235427 (2011).

117. Gerber, S., Reil, F., Hohenester, U., Schlagenhaufen, T., Krenn, J. R., and Leitner, A., "Tailoring light emission properties of fluorophores by coupling to resonance-tuned metallic nanostructures." *Physical Review B* **75**, 073404 (2007).

118. Schietinger, S., Aichele, T., Wang, H. Q., Nann, T., and Benson, O., "Plasmon-enhanced upconversion in single NaYF4: Yb3+/Er3+ codoped nanocrystals." *Nano letters* **10**, 134-138 (2009).

119. Kolesov, R., Grotz, B., Balasubramanian, G., Stöhr, R. J., Nicolet, A. A., Hemmer, P. R., and Wrachtrup, J., "Wave–particle duality of single surface plasmon polaritons." *Nature Physics* **5**, 470-474 (2009).

120. Fedutik, Y., Temnov, V. V., Schöps, O., Woggon, U., and Artemyev, M. V.,"Exciton-plasmon-photon conversion in plasmonic nanostructures." *Physical review letters* **99**, 136802 (2007).

121. Savage, K. J., Hawkeye, M. M., Esteban, R., Borisov, A. G., Aizpurua, J., and Baumberg, J. J. "Revealing the quantum regime in tunnelling plasmonics." *Nature* **491**, 574-577 (2012).

122. Tan, W. C., Preist, T. W., and Sambles, R. J. "Resonant tunneling of light through thin metal films via strongly localized surface plasmons." *Physical Review B* **62**, 11134 (2000).

123. Sergei, S., and Martin, O. J. F., "Resonant tunneling of surface plasmon-polaritons." *Optics Express* **15,** 6380-6388 (2007).

124. Shin, Y. M., So, J. K., Jang, K. H., Won, J. H., Srivastava, A., and Park, G. S., "Evanescent tunneling of an effective surface plasmon excited by convection electrons." *Physical review letters* **99**, 147402 (2007).

125. Tomita, S., Yokoyama, T., Yanagi, H., Wood, B., Pendry, J. B., Fujii, M., and Hayashi, S., "Resonant photon tunneling via surface plasmon polaritons through one-dimensional metal-dielectric metamaterials." *Optics Express* **16,** 9942-9950 (2008).

126. Zubin, J., "Quantum plasmonics." *MRS Bulletin* **37**, 761-767 (2012).

127. Zubin, J. and Shalaev. V., "Plasmonics goes quantum." (2011).

128. Scholl, J. A., Koh, A. L., and Dionne, "Quantum plasmon resonances of individual metallic nanoparticles." *Nature* **483**, 421-427 (2012)

129. Xiao, S., and Mortensen, N. A., "Resonant-tunnelling-assisted crossing for subwavelength plasmonic slot waveguides." *Optics Express* **16**, 14997-15005 (2008).

130. Avrutsky, I., Zhao, Y., and Kochergin, V. "Surface-plasmon-assisted resonant tunneling of light through a periodically corrugated thin metal film." *Optics Letters* **25**, 595-597 (2000).

131. Stockman, M.I., "Nanoplasmonics: The physics behind the applications." *Physics Today* **64**, 39-44 (2011).

132. Fofang, N. T., Grady, N. K., Fan, Z., Govorov, A. O., and Halas, N. J.. "Plexciton dynamics: exciton− plasmon coupling in a J-Aggregate− Au nanoshell complex provides a mechanism for nonlinearity." *Nano letters* **11**, 1556-1560 (2011).

133. Schlather, A. E., Large, N., Urban, A. S., Norlander P., and Halas, N. J., "Near field mediated plexitonic coupling and giant Rabi splitting in individual metallic dimmers," *Nano Letters* **13**, 3281-3286 (2013)

134. Li, J. B., Kim, N. C., Cheng, M. T., Zhou, L., Hao, Z. H., and Wang, Q. Q., "Optical bistability and nonlinearity of coherently coupled exciton plasmon system," *Optics Express* **20**, 1856-1861 (2012).

135. Melnikau, D., Savateeva, D., Susha, A., Rogach, A. L., and Rakovich, Y. P., "Strong plasmon-exciton coupling in a hybrid system of gold nanostars and J-aggregates," *Nanoscale research letters* **8**, 1-6 (2013)

136. DeLacy, B. G., Qiu, W., Soljacic, M., Hsu, C. W., Miller, O. D., Johnson, S. G., and Joannopoulos, J. D., " Layer-by-layer self-assembly of plexcitonic nanoparticles," *Optics Express* **21**, 19103-19112 (2013).

137. Manjavacas, A., Abajo, F. J. G. de, and Norlander, P., "Quantum plexcitonics: Strongly interacting plasmons and excitons," *Nano Letters* **11**, 2318-2323 (2011)

Brief Bio-data of Author

VENUS DILLU

Research Scholar,
Applied Physics Department, Delhi Technological University, Delhi

EDUCATION

Delhi Technological University (formerly Delhi College of Engineering), Delhi
Ph.D. in Applied Physics *(Pursuing)* **2009-Present**
Dissertation: "Integrated Plasmonic Waveguide and Devices"

National Institute of Technology, Jamshedpur
M.Tech in Surface Science & Engineering **2007 - 2009**
Thesis: "Conducting Polymer (CP) and Interpenetrating Polymer Network (IPN)"

St. John's College, Dr. B.R. Ambedkar University, Agra
M.Sc. Physics **2003 - 2005**
Specialization: Solid State Physics

Miranda House, University of Delhi, Delhi
B.Sc. Physics (Hons.) **2000 - 2003**

PUBLICATIONS AND PAPERS

S.N.	*Journal*	Title	*Authors*	*Year*	*DOI*
1.	*Journal of Applied Physics*	**Enhanced Fano resonance in silver ellipsoidal plasmonic crystal cavity**	*Venus Dillu, R.K. Sinha*	*2013*	*dx.doi.org/10.1063/1.4851775*
2.	*Plasmonics*	**Surface plasmon polariton band gap enabled plasmonic Mach Zehnder interferometer: Design analysis and application**	*Venus Dillu, R.K. Sinha*	*2014*	*dx.doi.org/10.1007/s11468-013-9652-5*
3.	*Physica E*	**Propagation characteristics of silver nanorods based compact waveguides for plasmonic circuitry**	*Venus Dillu, Shruti, Triranjita Srivastava, R.K. Sinha*	*2013*	*dx.doi.org/10.1016/j.physe.2012.11.025*
4	*OSA Technical Digest*	**Tuning Fano resonance in plasmonic nanocavity for enhance transmission**	*Venus Dillu, R.K. Sinha*	*2013*	*dx.doi.org/10.1364/FIO.2013.FTh3E.5*
5.	*Proc. SPIE*	**Fano resonance in silver nanoparticles in SOI structure: Design of plasmonic nanoswitch**	*Venus Dillu, Shruti, R.K. Sinha*	*2013*	*dx.doi.org/10.1117/12.2023931*
6.	*Proc. SPIE*	**Subwavelength plasmonic metallic nanopillar based coupler**	*Venus Dillu, Shruti, R.K. Sinha*	*2012*	*dx.doi.org/10.1117/12.929910*
7.	*Proc. SPIE*	**Hybrid metal-photonic crystal waveguide and cavities**	*Shruti, Venus Dillu, R.K. Sinha*	*2012*	*dx.doi.org/10.1117/12.929794*
8.	*Proc. SPIE*	**Design and analysis of plasmonic subwavelength waveguide array**	*Venus Dillu, Shruti, R.K. Sinha*	*2011*	*dx.doi.org/10.1117/12.892906*
9.	*Proc. SPIE*	**Infiltrated plasmonic photonic crystal cavity for sensing**	*Shruti, Venus Dillu, R.K. Sinha, R.Bhattacharyya*	*2011*	*dx.doi.org/10.1117/12.893754*
10.	*Proc. SPIE*	**Terahertz wave propagation in surface plasmon photonic crystal**	*Shruti, Venus Dillu, R.K. Sinha, R.Bhattacharyya*	*2011*	*dx.doi.org/10.1117/12.892903*
11.	*Proc. SPIE*	**One dimensional tunable surface plasmonic photonic crystal cavity**	*Shruti, Venus Dillu, R. Bhattacharyya, R.K. Sinha*	*2011*	*dx.doi.org/10.1117/12.899932*

PATENT

"*SYSTEM AND METHOD FOR DETECTING, INDENTIFYING AND CLSSIFYING CANCER CELLS"*
Indian Patent Application No.: *1168/DEL/2013*
Applicants: *Venus Dillu and R.K. Sinha*

TEACHING EXPERIENCE

Delhi Technological University, Aug-Nov 2009
Lecturer – Physics *(on Guest Faculty Position)*

MEMBERSHIPS

1. The Optical Society
2. SPIE

AWARDS AND RECOGNITIONS

1. OSI '**Excellent Paper Presentation**' for the paper with title, "Quantum size effects on plasmonic band gap of silver nanodisk heptamer," presented in ICOL held during 5-8 March 2014, **IRDE, Deharadun, India**

2. **Second Prize**, Poster presentation for the paper with title, "Arrayed silver nanopillars based plasmonic nano-cavity for telecom wavelength," presented in IONS-ASIA-3 held during 14-16 Sept. 2012, Changchun, China.

3. **OSA Foundation Award** from The Optical Society to attend FiO/LS 2013 and present paper "Tuning Fano resonance in plasmonic nanocavity for enhanced transmission" at Orlando, Florida, USA worth $1,500 USD

4. **Officer Travel Grant** from **SPIE** to attend Student Leadership Program and present paper at SPIE: Optics+Photonics 2011, San Diego, California, USA worth US$2200

5. **Officer Travel Grant** from **OSA** to attend Student Leadership Meeting and Frontiers in Optics 2012/Laser Science XXVIII at Rochester, New York, USA worth US$1600

6. **Student Travel Grant** from **OSA** to attend and present paper at IONS-AISA-3 at Changchun, China worth US$900

7. **Topper** in **M. Tech**(Surface Science and Engineering-2007-2009), NIT Jamshedpur

8. **GATE** (Graduate Aptitude Test of Engineers) Qualified 2007, All India Rank 633, Subject: Physics

PROFESSIONAL TRAININGS / SCHOOLS ATTENDED

1. **Siegman International School on Lasers**, 03-08 August 2014, Stanford University
2. **DST & Royal Society Indo-UK Seminar on Computational Photonics**, 01-03 March, 2014, IIT Delhi
3. **Guided Wave Optics and Devices**, 07-23 February, 2011, CGCRI, Kolkata
4. **National Workshop on Fiber Optics and Applications**, 28-29 November, 2009, Delhi University

EXTRA-CURRICULAR ACTIVITIES AND PERSONAL QUALITIES

Debating, Singing, Painting and doing Fine Arts
Basketball (Zonal Level, College)
Leadership Quality, Honesty and Hard-Work

Physica E 48 (2013) 75–79

Contents lists available at SciVerse ScienceDirect

Physica E

journal homepage: www.elsevier.com/locate/physe

Propagation characteristics of silver nanorods based compact waveguides for plasmonic circuitry

Venus Dillu, Shruti, Triranjita Srivastava, Ravindra Kumar Sinha *

TIFAC—Center of Relevance and Excellence in Fiber Optics and Optical Communication, Department of Applied Physics, Delhi Technological University (Formerly Delhi College of Engineering), Bawana Road, Delhi 110042, India

HIGHLIGHTS

- Silver nanorods based plasmonic waveguide is proposed.
- 3D FDTD and PWE methods are used for examining the basis waveguide.
- Proposed waveguide works for visible regime.
- Straight waveguide, bend and Y-splitter have been devised.
- Quality factor, confinement factor and losses are calculated.

GRAPHICAL ABSTRACT

We propose ultra-compact waveguides for plasmonic circuitry based on silver nanorods array embedded vertically into silicon on insulator substrate for nanoscale guidance of optical frequencies.

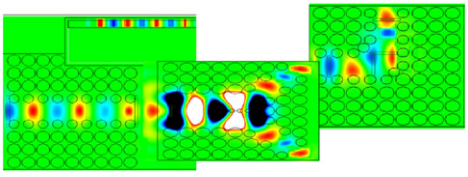

ARTICLE INFO

Article history:
Received 9 July 2012
Received in revised form
8 November 2012
Accepted 26 November 2012
Available online 7 December 2012

ABSTRACT

We propose ultra-compact waveguides for plasmonic circuitry based on silver nanorods array embedded vertically into silicon on insulator (SOI) substrate for nanoscale guidance of optical frequencies. Silver nanorods array palisade silicon to form core of SOI waveguide and is theoretically modeled for the first time. Propagation characteristics of the structure are obtained using finite difference time domain (FDTD) computations, exposing bandgap in the visible regime for transverse magnetic modes and are verified by the plane wave expansion (PWE) method. Narrow transmission bandwidth of ~10 nm with quality factor and confinement factor of 97.5% and 92% is achieved respectively, confirming strong confinement of the propagating mode at 633 nm and the losses calculated in decible per micrometer (dB/μm) for the waveguide is found to be .75 dB/μm for straight waveguide. Further, Y-splitter designed from the basis equally bifurcate power and the outputs received at the two ends are in phase yielding a viable 50–50 power splitter. Bend design routing light in nano-dimensions is also implemented successfully, offering components for high density plasmonic circuitry.

1. Introduction

Plasmonics as a subject deals with constricting electromagnetic (EM) radiation into subwavelength devices and offers extraordinary applications outdoing preceding technologies. Superfast computer chips [1], ultra-sensitive chemical–biomedical sensors [2], surface enhanced Raman spectroscopy (SERS) [3,4], cancer treatment [5], high performance solar cells [6], and ultra-efficient waveguide devices and nano-cicuitry [7,8] are few of the accomplishments achieved through plasmonics. Besides, the recent advancement in nanotechnology and nanophotonics has revolutionized the field of plasmonics promising miniaturization of circuitry to nanoscale dimensions and provides huge data transmission at the bandwidth of photonics [9–12]. But exhaustive research is needed to be able to make compact high density circuits which can be easily integrated with planar circuits requiring all its components on the same chip [13–14].

Among all the metallic elements, silver has the smallest damping constant Γ and is the best-performing choice at optical frequencies i.e. 400–700 nm [15]. Gold can be used as well but it has a larger Γ than silver and is often the metal of choice at lower near infrared (NIR) frequencies. Also, gold has high interband

* Corresponding author.
E-mail address: dr_rk_sinha@yahoo.com (R.K. Sinha).

1386-9477/$ - see front matter © 2012 Elsevier B.V. All rights reserved.
http://dx.doi.org/10.1016/j.physe.2012.11.025

losses in the visible spectrum. Similarly, copper, platinum, and palladium are avoided due to large interband losses over most of the visible spectrum. Thus, silver has predominately been the material of choice for plasmonic applications around the optical frequencies. Ag particles in air have plasmon resonances at 350–480 nm but they can be red-shifted in a controlled way over the entire 500–1500 nm spectral range by partially embedding them in SiO_2, Si_3N_4 or Si [16]. Kwata et al. reported subwavelength optical imaging through metallic nanorod array [17] presenting the performance of plasmonics. Silver wires behave as surface plasmon resonators and electromagnetic energy transport through metallic nanowires deposited on the dielectric substrate [18]. Hence the properties of nanostructured silver make it most suitable for the next generation plasmonics [19].

Metal nanowires/nanorods are adept choice for designing compact plasmonic waveguides since it is an attractive option mainly due to nanoscale—confinement, guiding, imaging and show comparatively low propagation losses [20,21] because of their unique optical properties. But integrating the horizontally lying nanorod structures with main circuitry is a challenge and hinders the efficient excitation of the surface plasmon polaritons (SPPs) which are excited using the end fire excitation technique [22] or the prism coupling [23], which is often cumbersome to be used in chip design.

To get over this, laying silver (Ag) nanorods perpendicularly into semiconductor material, opens up the option of making planar components for plasmonic circuitry as well as allow efficient coupling with parallel devices. So, we propose a new design for compact plasmonic waveguide in which square lattice array of silver nanorods are embedded in silicon on insulator (SOI) substrate, Fig. 1(a) with main purpose to show stronger confinement with appreciable propagation length of 633 nm wavelength, exhibiting substantial quality factor and thus can be efficiently implemented in high density on-chip circuits due to its planar geometry. Nanorods having negative dielectric constant are embedded into SOI with palisade high refractive index Si core and have SiO_2 base as substrate resulting in the proposed core for light propagation. Ag nanorods provide lateral confinement within the nano sized low loss Si core in contrast to lossy planar metal structure, arrayed structure provides bandgap and texturing due to base of metal rods, yields the momentum to the propagating plasmon through the waveguide. Insulator as substrate offers vertical confinement also making it rugged and compatible for integrated circuitry. The high refractive index core of silicon retains the propagating mode and the bandgap forbids the mode from leaking. Arrayed basis waveguide exhibits a bandgap in the visible region; however, the introduced defect provides a strong field confinement to the propagating 633 nm wavelength with a bandwidth of 10 nm, and can be used as a narrow band-pass filter as well. Pyayt et al. [24] employed tapered silver nanowire with polymers but it can be bothersome at high temperature.

Usefulness of this approach is that, such designs are compatible with the commercially examined available technology [25] and provides us the synergistic results of plasmonics via photonics and electronics [26] along with easy integration with planar circuitry. We have obtained strong confinement and low loss in the proposed waveguides. More importantly it is easy to introduce defects by removing nanorods to make various devices (straight waveguide, bend, S-bend, Y and T-splitters, couplers etc.) in the reported arrayed geometry without inducing an unwanted stress at bends and corners which is noticeable in case of metal sheets or films when they are cut at sharp bends or when holes and grooves are incised into metal. Hence the basis geometry can be easily employed to devise various optical components such as couplers, splitters, multiplexers, demultiplexers etc., thereby, opening new possibilities in the ultra compact plasmonic circuitry design.

2. Structure design and simulation method

The basis structure comprises of arrangement of silver nanorods in a square lattice lying perpendicularly on the silicon-on-insulator as substrate. The waveguide is designed by introducing defects in the periodicity. Proposed straight waveguide is composed of a line defect in the basis waveguide comprising of periodically arranged silver nanorods (with dielectric constant, $\varepsilon = -13.6089 + i0.995$ at 633 nm) embedded to an optimized depth of 50 nm into the SOI substrate. The schematic representation of the basis waveguide cross section (x–y plane) and top view (x–z plane) are shown in Fig. 1(a) and its inset respectively.

Values of various parameters of the components used in designing the devices are as mentioned here, the silver nanorods of radius (r_{Ag}) 45 nm, height (h_{Ag}) 150 nm and lattice constant $a_{Ag}=110$ nm are arranged in a square lattice arrangement into silicon layer of refractive index $n_{Si}=3.5$ with thickness (h_{Si}) 100 nm to a depth of 50 nm into it. SiO_2 layer of refractive index

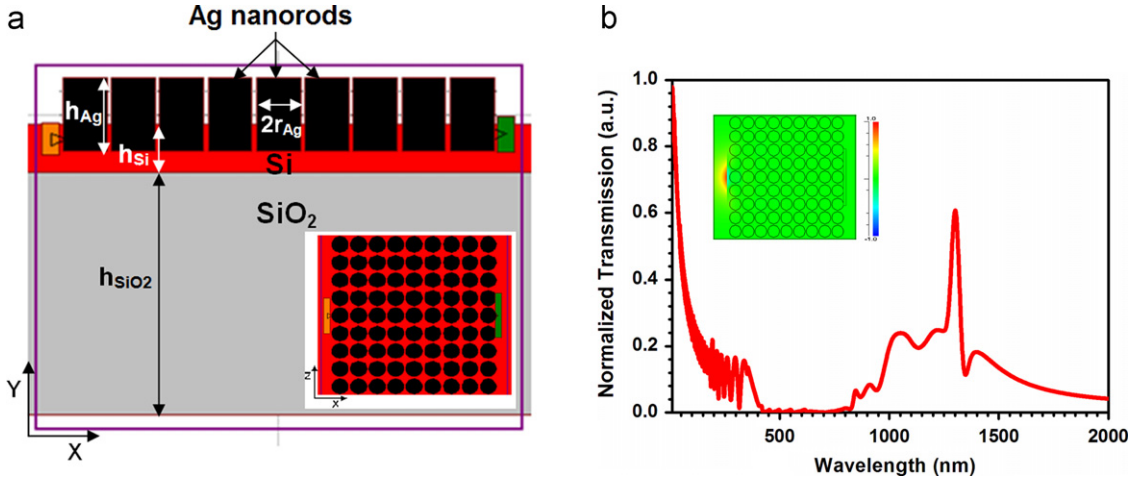

Fig. 1. (a) Schematic of the basis waveguide cross-section (x–y plane) and top view in inset (x–z plane) of proposed basis waveguide comprising of silver nanorods on silicon on insulator (SOI) substrate. (b) Normalized transmission for the basis structure showing bandgap within 400–800 nm and inset show E_y field profile depicting the light is forbidden from propagation.

$n_{SiO_2} = 1.45$ with thickness (h_{SiO_2}) 500 nm is chosen as a substrate. Such a basis waveguide has been found to exhibit a bandgap in the visible regime, this is shown in Fig. 1(b) as the normalized transmission depict gap within the visible regime and the simulated E_y field profile is represented in the inset of Fig. 1(b) indicating the gap offered by the periodic structure. The length of the waveguide is 1 μm. The defect in the straight waveguide is designed by removing silver nanorod linear array with diameter 90 nm and optimizing the adjacent rod radii to 35 nm resulting in nanometer sized defect. The bend design also has similar defect as in straight waveguide till 400 nm of length and then light bends at the corner with the aid of an additional nanorod introduced at the bend, traversing the remaining length of the waveguide. In Y-splitter the light is launched in a wider defect by removing three rows of nanorods and then the presence of four additional nanorods of radii 25 nm each bifurcate the propagating mode into the arms of the splitter each with a defect width of 90 nm.

Bandgap for the structure is verified by using plane wave expansion (PWE) simulations and the results yield accurate measurement of gap (Fig. 2(a)) and also confirm the results of transmissions characteristics (Fig. 1(b)). We have optimized various controlling parameters by running the scan over a range of parameter giving the option for choosing the appropriate values. The gap map calculated using the PWE method shows prominent transverse magnetic (TM) gap offered by the structure, as portrayed in Fig. 2(a) and largest gap is marked as Band-1. The gap-map is scanned for a range of radii giving the optimized radius value of 45 nm obtained from the central value of the maximum gap region i.e. Band-1 yielding the frequency value of 1.57 in units of $\omega a/2\pi c$. The structure is also scanned over a range of wavelengths; the graphical representation of the measured gap-map for the structure is indicated in Fig. 2(b) which shows that the bandgaps are larger around 600 nm wavelength and we can tailor our device near this wavelength. However by introducing a line defect we have proposed a straight, bend waveguides and Y-splitter which is discussed later in Section 3.

3. Results and discussion

In order to obtain the propagation characteristics of such waveguides, the 3D Finite Difference Time Domain (FDTD) method is employed. The simulation has been performed using perfectly matched layer (PML) boundary conditions with PML width=500 nm along the *x*, *y* and *z* directions and average grid size of 6.25 nm was taken along the *x*- and *z*-axis whereas, 10 nm along the *y*-axis. The light wave of wavelength 1550 nm is launched into the device perpendicular to the longitudinal axis of the Ag nanorods. We first examined the normalized transmission spectrum for the complete structure with no defect as a function of wavelength and this can be observed from Fig. 1(b) that the structure offers a transverse magnetic (TM) bandgap for wavelength range of 400 nm to 800 nm. This is also realised by observing the contour plot of Electric field (E_y) along the propagation direction for the launched wavelength in the inset of Fig. 1(b) which shows that the light is prohibited from propagating through the structure resulting in the bandgap. The gap is also verified by the PWE method and is pictorially presented in Fig. 2(a) and (b).

It is to be mentioned that since, the bandgap in the basis waveguide covers the visible region and silver support plasmons in visible spectrum, hence, the device was optimized for 633 nm anticipating its vast grounded applications. Thus, in the following we discuss the properties of the various waveguides and devices based on the defect in the basis waveguide at 633 nm.

Maier and his group have reported that electromagnetic energy can be carried along the array of Cu rods in air [27] which supports that it is possible to design plasmonic circuits with silver nanorods embedded into SOI which can carry the EM energy in the defect region of silicon fenced by metal rods and having SiO_2 beneath Si. The narrow defect forms the core of the waveguide where the energy propagates.

3.1. Straight waveguide

The basis waveguide is engineered for linear defect, which is introduced by removing the central row of nanorods, resulting in a straight waveguide, as shown in the inset (i_1) of Fig. 3(a). Also the radii of the nanorods lying in the adjacent rows (radius=35 nm) were tuned to insist the propagation of the launched light at 633 nm. The depth to which the rods are inserted is optimized to be 50 nm; by doing so we found that the maximum intensity of the mode stays in Si defect region as compared to that when kept superficially above silicon slab or when inserted completely. Electromagnetic energy traverses through the defect and the presence of metal nanorods leads to the confinement of this energy within the subwavelength defect. The textured interface at the base of the nanorods and Si slab leads to the generation of the localized plasmons and hence, provides strong confinement of light within the waveguide. Further, the inset (i_2) in Fig. 3(a) illustrates the top view and lateral view of the contour mode profile of transverse electric field (E_y) respectively which depicts that the mode stays within the desired subwavelength linear defect waveguide.

On introducing the linear defect, the structure acts like a waveguide and the defect parameters (radius, height etc.) are optimized for 633 nm wavelength because by preparing silver

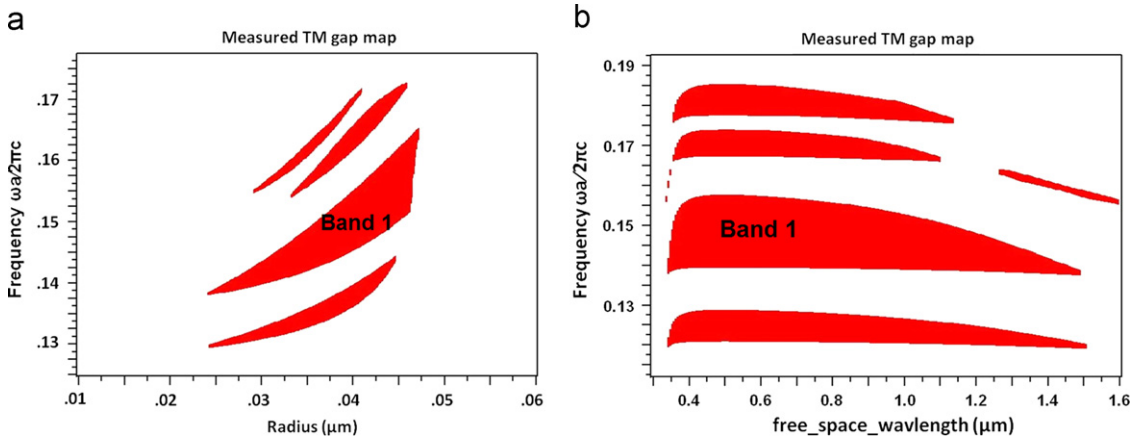

Fig. 2. (a) and (b) Measured TM gap map representing the gap region offered by the structure scanned over a range of radii and wavelengths respectively.

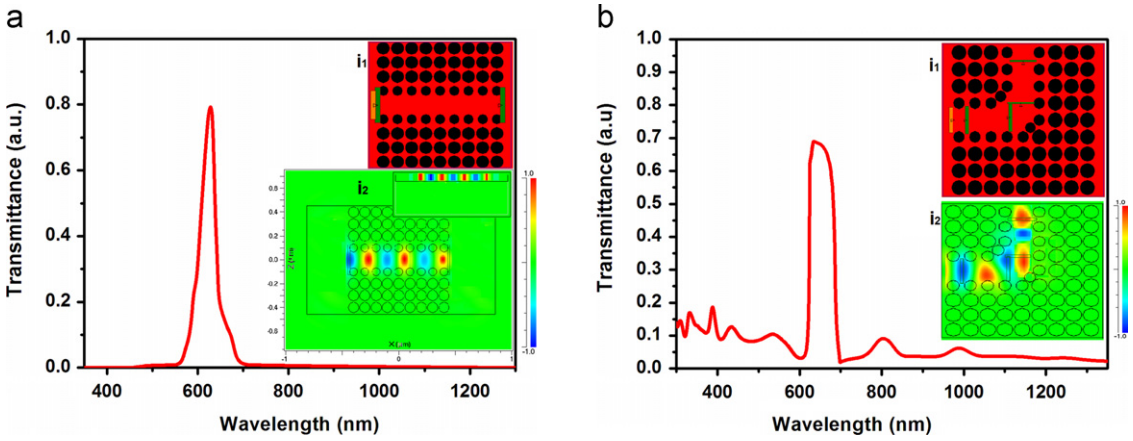

Fig. 3. (a) Normalized transmission for the proposed straight waveguide showing peak at $\lambda=633$ nm, schematic of the structure and the E_y field profile in the x–z and x–y planes are given in the inset. (b) Bend waveguide is shown with the resonating peak at 633 nm and the inset shows the structure and the E_y field profile depicting how the energy is bending in the waveguide.

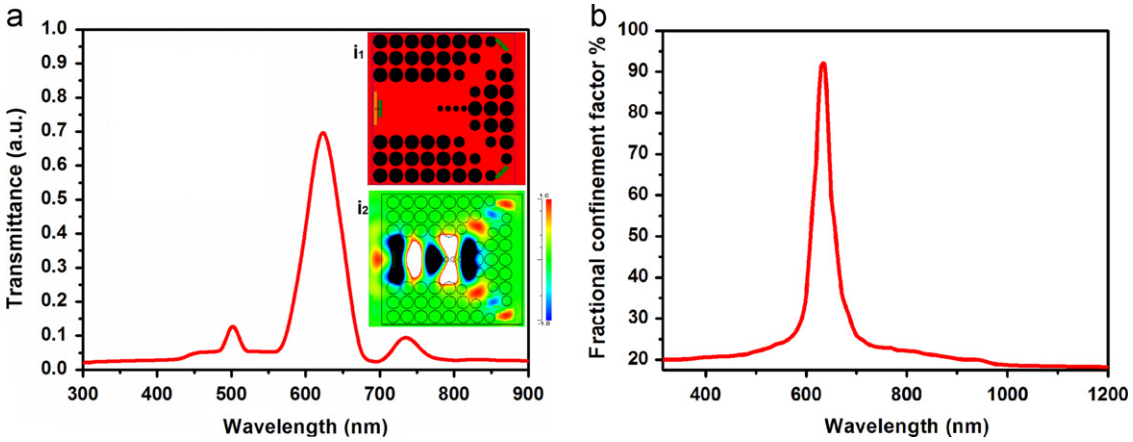

Fig. 4. (a) Normalized transmission for the proposed Y-splitter with resonating peak at $\lambda=633$ nm. Schematic and the E_y field profile showing energy splitting into the two arms is given in the inset. (b) Variation of fractional confinement factor with wavelength indicating maximum confinement for 633 nm wavelength.

nanostructures of different sizes and shapes the SPR wavelengths can be tuned for different wavelengths [28,29]. Also, it is observed that the plasmons in silver resonate over visible frequency range [16] therefore it is suitable to design devices having applications and requirement of the visible regime.

The normalized power transmittance for the nano-sized straight waveguide indicates the resonating peak at 633 nm as shown in Fig. 3(a) and is calculated by measuring the fraction of power at output with respect to the input. The straight waveguide exhibits a quality factor of 97.5% for $\lambda=633$ nm. Also, the fractional confinement factor i.e. ratio of power at the output of the core to the output of the whole waveguide is described later in this section. We see that 92% confinement for the propagating wavelength is for 633 nm and is calculated to be less for the rest of the wavelengths validating that the device is tuned for 633 nm wavelength, as shown in Fig. 4(b).

3.2. Bend waveguide

Apart from straight waveguide, the basis waveguide can also be utilized for making bend through it. An efficient bend design is devised by centrally removing the silver nanorods approximately at right angles. For the light to bend at the corner, an additional silver nanopillar with an optimized radius is introduced at the corner of the bend which acts as a reflector, as shown in the inset (i_1) of Fig. 3(b) and the curve plotted in the figure represents the normalized power transmission, which shows a major peak transmission at wavelength 633 nm along with a few smaller peaks. The propagating mode is able to take sharp bends with ease. The computed field (E_y) profile obtained on investigation of the bend design appears in the inset (i_2) of Fig. 3(b), exhibiting confinement of the modal power within the bend waveguide.

3.3. Y-splitter

The Y-splitter devised from the basis waveguide consists of y-shaped defect in the basis waveguide (top view as shown in the inset (i_1) of Fig. 4(a)). The pillars adjacent to the defect are optimized to a radius of 35 nm and additional nanorods of radius 25 nm introduced at the junction of the two bifurcating arms assist splitting. It is found that the introduced defect and its optimization provide easy propagation for 633 nm wavelength. The output power obtained at the end of the individual arms is found to be equal and incident light reaches the monitor at the end of the two arms in same phase. The normalized power transmission obtained from the proposed Y-splitter shows a peak at the optical wavelength of 633 nm and it is observed that the result overlaps for the two arms of the splitter, as shown in Fig. 4(a) hence it can work as 50–50 power splitter. Y-splitter shows confinement of modal power within the defect region of the waveguide. The contour map of the field E_y depicts and

indicates how the incident energy divides at the origin of the splitting arms of the splitter see the inset (i_2) of Fig. 4(a).

Further, the fractional modal power i.e. confinement factor for different wavelengths is investigated for the line defect as shown in Fig. 4(b). Fractional confinement factor is defined as ratio of power at the output of the core to the output of the whole waveguide. It is observed that the optimized straight waveguide shows the peak confinement factor of 92% for the propagating wavelength of 633 nm and is calculated to be less for the rest of the wavelengths validating that the device is tuned for 633 nm wavelength. The propagation length for the defect is calculated to be 1 μm which is more than sufficient when we have to make nano-sized circuit components. Subwavelength confinement of the 633 nm wavelength within the narrow defect opens the way for dense circuitry. Tolerance limit for various rod parameters was calculated, which comes out to be 5 nm in case of rod radii whereas 10 nm with respect to height of the rod which makes it to be a very sensitive device as well. We calculated the loss in dB/μm for all the considered structures and found it to be .75 dB/μm, .89 dB/μm and .77 dB/μm for the straight waveguide, bend waveguide and Y-splitter respectively, thereby exhibiting more loss in the bend waveguide as compared to the straight waveguide and Y-splitter. When the waveguide is bent to form bend design or Y-splitter, the propagating modes in these waveguides experience perturbation from the initial condition (i.e. w.r.t. the straight waveguide) at the bends and corners, which leads to losses thereby resulting in little broadening of the transmittance curve for bend design and Y-splitter shown in Figs. 3(b) and 4(a) respectively as compared to the transmittance curve for straight waveguide in Fig. 3(a). This can be seen by the calculated losses mentioned above, which depicts that in the straight waveguide we get low losses as compared to the bend waveguide and Y-splitter. In literature the transmission losses of about 6 dB/μm for gold and silver array structure particles are reported by Atwater [7] and the losses of 1.2 dB/μm for 1.5 μm wavelength in gold nanodots on SOI [30] which can be improved by incorporating the proposed geometry for making various devices. Hence, the proposed waveguides with high confinement ~92% with ~.75 dB/μm loss may lead to high density nanophotonic device. With these waveguides one can positively realize nanoscale circuitry i.e. "lab on a chip" [7] and make light route through nanoscale dimensions. Also, with the proposed bend design and Y-splitter, propagating modes can be bent with low losses. Since the device dimensions itself is in nano range, these designs can be used for high density integrated circuits. Apart from light transmission, nanoscale routing, waveguiding, and chip circuitry can also be used for making nano plasmonic sensors, Mach–Zehnder interferometer for calculating minute phase changes, EM field enhancement etc. It also provides a convenient planar geometry that can be easily integrated with other components forming the plasmonic circuitry.

4. Conclusion

In conclusion, we have proposed and analyzed compact Ag nanorods based plasmonic waveguides and devices for the visible regime of electromagnetic spectrum to be used for integrated plasmonic circuitry. Embedded design on SOI offers strongly confining geometry which can be utilized well as the waveguides and also make it robust. Induced defects in the basis waveguide restricts the mode in nano-sized defect and efficiently guide the propagating mode at 633 nm with low losses, which can also be tuned for other wavelengths by altering the various waveguide parameters such as, periodicity or radii of rods or the width of the defect. The quality factor achieved is 97.5%, which is good in case of plasmonics, appreciable propagation length of 1 μm is reached which is far more than sufficient in case of compact dense circuits and high fractional confinement of 92% with comparable losses exposes motivation for its implication to make other parallel devices. Successful implementation of bend design and Y-splitter affirms that such waveguide assist the possibility of making lab on a chip. The proposed planar geometry with strong lateral and vertical confinement of the modes renders easy integration with chip circuitry. The investigations provided here validate the use of nano-structures for the SPP propagation and hence, miniaturize the optical devices for specific applications.

Acknowledgment

The authors gratefully acknowledge (i) the initiatives and support toward establishment of "TIFAC—Center of Relevance and Excellence in Fiber Optics and Optical communication at Delhi College of Engineering, Delhi" through Mission Reach Program of Technology Vision 2020, Government of India and (ii) UGC sponsored major research project in the area of Photonic Crystal Fibers for sensing and telecom. applications.

References

[1] S.J.B. Yoo, Electronics Letters 45 (2009) 584.
[2] J. Homola, Chemical Reviews 108 (2008) 462.
[3] S. Nie, S.R. Emory, Science 275 (1997) 1102.
[4] X. Zhang, Q. Zhou, J. Ni, Z. Li, Z. Zhang, Physica E 44 (2011) 460.
[5] C. Loo, A. Lowery, N.J. Halas, J. West, R. Drezek, Nano Letters 5 (2005) 709.
[6] V.E. Ferry, L.A. Sweatlock, D. Pacifici, H.A. Atwater, Nano Letters 8 (2008) 4391.
[7] H. Atwater, Scientific AmericanApril Issue (2007) 56.
[8] S.A. Maier, M.L. Brongersma, P.G. Kik, S. Meltzer, A.A.G. Requicha, H. Atwater, Advanced Materials 13 (2001) 1501.
[9] W.L. Barnes, A. Dereux, T.W. Ebbesen, Nature 424 (2003) 824.
[10] X. Guo, M. Qiu, J. Bao, B.J. Wiley, Q. Yang, X. Zhang, Y. Ma, H. Yu, L. Tong, Nano Letters 9 (2009) 4515.
[11] T.W. Ebbesen, C. Genet, S.I. Bozhevolnyi, Physics Today (2008) 43.
[12] E. Ozbay, Science 311 (2006) 189.
[13] M. Hochberg, T.B. Jones, C. Walker, A. Scherer, Optics Express 12 (2004) 5481.
[14] G. Veronis, S. Fan, Applied Physics Letters 87 (2005) 131102.
[15] P.B. Johnson, R.W. Christy, Physical Review B 6 (1972) 4370.
[16] H.A. Atwater, A. Polman, Nature Materials 9 (2010) 205.
[17] A. Ono, J. Kato, S. Kwata, Physical Review Letters 95 (2005) 267407.
[18] T. Laroche, C. Girard, Applied Physics Letters 89 (2006) 233119.
[19] M. Rycenga, C.M. Cobley, J. Zeng, W. Li, C.H. Moran, Q. Zhang, D. Qin, Y. Xia, Chemical Reviews 111 (2011) 3669.
[20] C.J. Barrelet, A.B. Greytak, C.M. Leiber, Nano Letters 4 (2004) 1981.
[21] A. Ono, J. Kato, S. Kwata, Physical Review Letters 95 (2005) 267407.
[22] A.W. Sanders, D.A. Routenberg, B.J. Wiley, Y. Xia, E.R. Dufresne, M.A. Reed, Nano Letters 6 (2006) 1822.
[23] D.F. Pile, T. Ogawa, D.K. Gramotnev, T. Okamoto, M. Haraguchi, M. Fukui, S. Matsuo, Applied Physics Letters 87 (2005) 061106.
[24] A.L. Pyayt, B. Wiley, Y. Xia, A. Chen, L. Dalton, Nature Nanotechnology 3 (2008) 660.
[25] P. Dainesi, A. Kung, M. Chabloz, A. Lagos, P. Fluckiger, A. Ionescu, P. Fazan, M. Declerq, P. Renaud, P. Robert, Photonics Technology Letters 12 (2000) 660.
[26] R. Zia, J.A. Schuller, A. Chandran, M.L. Brongersma, Materials Today 9 (2006) 20.
[27] S.A. Maier, M.L. Brongersma, H.A. Atwater, Applied Physics Letters 78 (2001) 16.
[28] Y. Xia, N.J. Halas, MRS Bulletin 30 (2005) 338.
[29] M.E. Stewart, C.R. Anderton, L.B. Thompson, J. Maria, S.K. Gray, J.A. Rogers, R.G. Nuzzo, Chemical Reviews 108 (2008) 494.
[30] S. Maier, M.D. Friedman, P.E. Barclay, O.J. Painter, Applied Physics Letters 86 (2005) 071103.

Surface Plasmon Polariton Band Gap-Enabled Plasmonic Mach–Zehnder Interferometer: Design, Analysis, and Application

Venus Dillu & R. K. Sinha

Plasmonics

ISSN 1557-1955

Plasmonics
DOI 10.1007/s11468-013-9652-5

Springer

Plasmonics
DOI 10.1007/s11468-013-9652-5

Surface Plasmon Polariton Band Gap-Enabled Plasmonic Mach–Zehnder Interferometer: Design, Analysis, and Application

Venus Dillu · R. K. Sinha

Received: 7 June 2013 / Accepted: 19 November 2013

Abstract In this paper, we propose a design for surface plasmon polariton band gap (SPPBG)-enabled plasmonic Mach–Zehnder interferometer (PMZI) comprising of array of silver nanorods embedded upright into silicon on insulator (SOI) substrate and analyze its potential in sensing, intended for cancer therapy. Periodic arrangement of nanorods embedded into SOI substrate grants strong spatial confinement and assist waveguidance to the propagating plasmon mode due to the SPPBG effect. This arrayed system triggers local field enhancement promoting sensing proficiency of the device and is assessed in terms of wavelength and phase shift. Proposed design of SPPBG-enabled PMZI sensor is successfully employed for detection and classification of various cancerous cells. The structural parameters of PMZI are optimized in compliance with the plasmonic band gap in the range of 400–800 nm yielding exceptionally high sensitivity at input wavelength of 633 nm. Volumetric analysis of the analyte reveals that very small analyte volume of the order of 10^{-15} cc is sufficient to yield significant phase shift. Phase shift obtained for the breast adenocarcinoma and blood cancer cell lines are 1.2357radian and 0.3351radian, respectively, which read very high value of phase shifts to identify extremely small changes in refractive index of the analyte. Figure of merit calculated thereby expose impressive device performance outdoing preceding plasmonic sensors leading to validation of proposed ultra-compact-sensitive PMZI design.

Keywords Plasmonic Mach–Zehnder interferometer · Silver nanorods · Plasmonic band gap · Cancer cells · Sensitivity

V. Dillu · R. K. Sinha (✉)
TIFAC-Centre of Relevance and Excellence in Fiber Optics and Optical Communication, Department of Applied Physics, Delhi Technological University (Formerly: Delhi College of Engineering), Bawana Road, Delhi 110042, India
e-mail: dr_rk_sinha@yahoo.com

Introduction

Surface plasmon polaritons (SPPs) are electromagnetic waves guided along metal–dielectric interfaces resulting from the interaction of incident photon with that of collective electron oscillations in metals. Their field components decay exponentially in both the neighboring media with maximum intensity at the interface making them extremely sensitive to the surface features, ideal for designing sensors. Resultant SPPs have shorter wavelength than that of the incident photon and hence provide strong spatial confinement. Due to these properties, through plasmonics, one can govern light manipulation at nanoscale and this has brought tremendous changes in the device technology. Plasmon propagation and waveguiding is not only restricted to the planar interfaces but can also be efficiently controlled by plasmonic band gap effect arising due to periodic arrangement of metallic nanostructures [1–3]. The motivation for surface plasmon polariton band gap (SPPBG) structures arises from photonic band gap structures which allow lossless waveguiding even around sharp corners [4]. Thus, an obvious employment is to realize SPPBG structures, leading to ultra-compact and highly sensitive devices which can be efficiently achieved by exploiting metallic array of nanorods. Defect in SPPBG structures can trap and guide plasmons having frequencies that fall within the gap region by SPPBG effect. Using array of metal nanorods for creating SPPBG material yields control over the plasmonic band gap region and consequently over plasmon propagation, to get desired properties. By tailoring plasmon propagation via SPPBG, one can utilize its unique optical properties [5] with promising applications in nanoscale signal routing, waveguiding, miniaturization of integrated circuitry, extraordinary light transmission, sensing, etc., and out of these, sensing has unrivalled importance. Plasmonics has greatly influenced the sensing techniques. Efficiency of these sensors entails detecting minute changes and inferring

Published online: 30 November 2013

crucial conclusions from the output that can help in diagnosing grave diseases such as cancer.

To improvise sensing efficiency, interferometers are involved into sensing such as Mach–Zehnder interferometer (MZI), which offers profound method to inspect molecular response. Their response is further enhanced by employing plasmonics: in making sensors [6, 7], for determination of phase [8], to calculate electron density [9], etc. So, the synergy of plasmonics into interferometry extends accurate method for detection and enhances sensitivity by incorporation of metallic structures [7, 10–13]. To draw benefits from their plasmonic properties, metal structures of controlled size and shape [14, 15] at nanoscale are integrated with dielectric to get the desired results which enables tailoring the peak resonance; enhances electromagnetic field; improves sensitivity, transmission, and imaging properties, and their periodic arrangement can allow easy waveguidance through SPPBG effect [3]. Although thin metallic films can also be employed, but such geometry can lead to resistive losses [8, 12]; therefore, metallic nanostructures have specifically received considerable attention [15] especially for designing sensors. A rewarding application will be to design sensors for diagnosing and classifying different cancer cell lines.

In order to meet this challenge of designing sensor for studying cancer cells, photonics has competently offered techniques via optical microscopy, imaging, scanning refractive index, etc. [16–21]. Biophysical properties of cancer cells have been studied which helps in monitoring the inception and prognosis of cancer [22–27]. However, plasmonics [28–33] has directed the way for sophisticated methods than conventional methods known hitherto, since detection of cancer is an essential step towards monitoring the disease effectively. Cancer cells have higher refractive index (RI) than the normal cells [16, 18, 34]. Identifying this RI difference can help in quantitative analysis of malignant cells because increased RI points to cell anomaly. RI of living cells can be measured by following classical and modern approaches [16–18, 35–38], but sensing RI difference accurately is important, mainly because numerous biological substances can be identified and detected through sensing the variation in RI. Plasmonic sensors have effectively replaced traditional RI sensors due to extremely responsive interaction of SPP field with the analyte [39–41]. Sensors meant for pathological applications [42] calls for ultra-compact devices along with high sensitivity.

Thus, in this paper, we report what we believe to be a novel design for highly sensitive ultra-compact PMZI sensor based on SPPBG effect with applications in label-free detection and classification of various forms of cancer cell such as Jurkat (blood/bone marrow cancer cell), HeLa (cervical cancer cell), PC 12 (adrenal gland cancer cell), MDA MB 231(breast cancer cell), and MCF 7 (human breast adenocarcinoma cell). Proposed PMZI sensor is designed by embedding periodic array of silver nanorods into silicon on insulator (SOI) yielding SPPBG structure, with the defect forming the core for plasmon propagation, offering strong lateral confinement and assisting waveguidance to the resultant mode due to plasmonic band gap, reducing the propagation losses. This design overcomes the size limitation [6] and angular dependence of the prism-based devices. Arrayed silver nanorods also grant local field enhancement and avoid ohmic losses increasing the sensitivity of the device. Proposed PMZI produces significant wavelength and phase shift thus improving the proficiency of the plasmonic sensors reported in preceding literatures [7, 9, 43]. By merging arrayed silver nanorods geometry with interferometry, we get an ultra-compact PMZI design which is proficiently implemented for the detection of various cancer cell lines serving as an important compact nano-sized device for disease diagnosis.

Structural Design of PMZI Sensor

The schematic configuration for the SPPBG-enabled PMZI sensor for cancer cell analysis is shown in Fig. 1a. It utilizes non-prism geometry reducing the complexity which prisms add [6] to the surface plasmon resonance (SPR) sensors, providing it a platform to be used in multifarious environment. We have used arrayed silver nanorods to obtain the SPPBG effect for waveguidance of the propagating plasmons and to get intense surface field available for interaction with analyte. We use silver because among all other metallic element it has the smallest damping constant Γ [44]. Owing to the fact that silver has the lowest Γ, the device will result in approximately loss less intense plasmon field at the interface increasing the efficiency of the sensor. So, for sensing application where we need to detect the environmental changes, silver metal is preferred. Gold or other metal can also be used but they exhibit larger damping constant than silver and also show high interband losses [44] as compared to silver. The base structure includes arrayed silver nanorods (with dielectric constant, $\varepsilon = -13.6089 + i0.9950$ at 633 nm, rod radius, $r_{Ag} =$ 45 nm, and rod height, $h_{Ag} = 150$ nm) arranged in square lattice (lattice constant, $a = 110$ nm) embedded upright to a depth of 50 nm into SOI (Si-on-SiO_2, with Si thickness, $h_{Si} =$ 100 nm, and SiO_2 thickness, $h_{SiO2} = 500$ nm) substrate with plasmon mode propagating through the defect having frequency that lie within the plasmonic band gap obtained for full structure. We have applied transverse magnetic (TM) polarization of the incident light to the interferometer with electric field of the incident wave perpendicular to the x–y plane. Guo et al. [13] have used Ag and ZnO nanowires for designing MZI but curved surfaces of horizontally lying nanowires affix complexity to sensing application. We considered this limitation in our design by using a planar platform for the analyte. The arrayed geometry also allows easy drawing of any defect shape required for waveguiding by removing the nanorods intended for the defect [45]. Proposed design

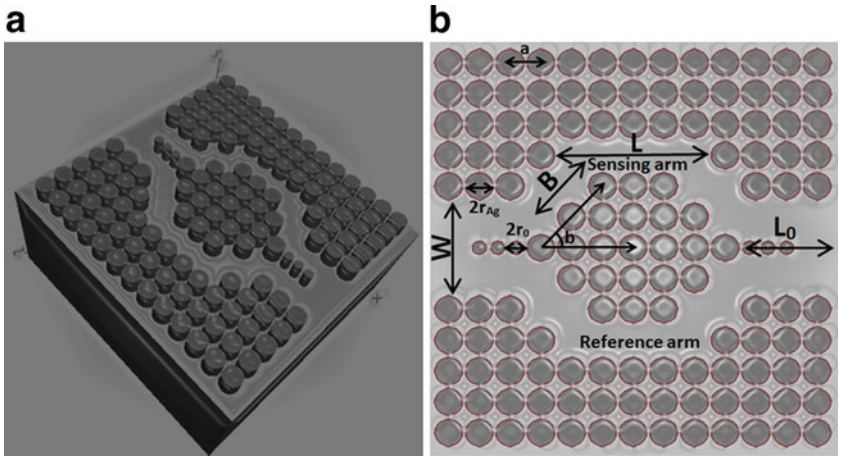

Fig. 1 **a** Schematic representation of the proposed plasmonic Mach–Zehnder interferometer (PMZI) using silver nanorods embedded upright into silicon on insulator (SOI) substrate. **b** Top view of PMZI presenting the various optimized parameters for SPP propagation and its interference

offers strong mode confinement due to the high refractive index contrast at the interface and band gap offered by the periodic structure. For designing sensing device from the base geometry, the width, arm length, bend angle, and bend length for PMZI are optimized to yield constructive interference at the output port to be able to sense the difference produced between the reference and sensing arms of the PMZI.

The width W and length L_0 (length before the bifurcating PMZI arms) of the PMZI undivided core are optimized to be 330 nm which concedes successful execution of plasmon interference in the proposed interferometer. Additional silver rods of radius, r_0=25 nm, are introduced at the input to optimize the condition for bifurcating the intensity of propagating plasmon mode into the two arms of the PMZI. Reference and sensing arm length L of the PMZI comes out to be 550 nm having width of 110 nm for its proper functioning. Bend angle and bend length obtained for the resultant propagating mode is b=45° and B=155 nm, respectively. The schematic of the contemporary design of the proposed PMZI is shown in Fig. 1a, b. One arm of the PMZI is designated as the sensing arm and the other as the reference arm. The sensor detects the RI changes implemented at the sensing arm with respect to the control at the reference arm. It allows plasmon propagation available for light–matter interaction equipped for sensing for the optimized structural parameters. Various parameters, i.e., width, arm length, bend angle, and bend length, are optimized in accordance to the results obtained using finite-difference time domain (FDTD) and plane wave expansion (PWE) method for the input wavelength of 633 nm.

Result and Discussion

Estimation of SPPBG Using PWE Method and Propagation Characteristics of SPP

To determine the plasmon-resonant properties of the proposed system, Maxwell's equation for the system are to be solved [15]. In case of spherical nanoparticles, Mie scattering theory provides rigorous solution, but for nonspherical geometries, FDTD method is widely used and it is a powerful technique for modelling nanostructures with complex shapes [15, 46]. Since the proposed PMZI structure comprises of a system of Ag nanorods array embedded into SOI, so we appropriately use FDTD computational method to numerically assess the temporal evolution of electromagnetic fields using Maxwell's equation whereas the plasmonic band gap is obtained by PWE method. The basis (full) structure exhibits plasmonic band gap for the wavelength region of 400–800 nm shown as band 1 in Fig. 2 for TM plasmon mode, using PWE method. Measured TM gap map reveals the optimized value for the input frequency and the rod radius obtained from the largest gap region and is marked in Fig. 2. The band gap region in Fig. 2 helps us to ascertain the approximate input wavelength falling within the band gap regime (≈400–800 nm) which can be used for our structure for the optimized parameter. Introducing a defect in the base structure allows light propagation for the wavelength which lies within the band gap region, obtained for the structure.

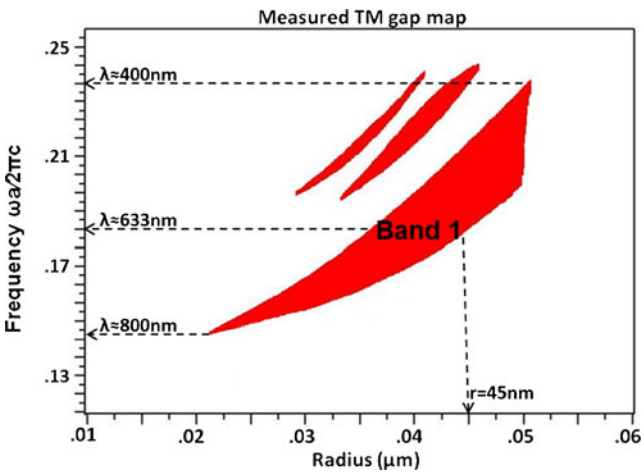

Fig. 2 Measured TM gap-map for the full structure representing gap region offered by the basis indicating relevant values of different parameters required for plasmon propagation

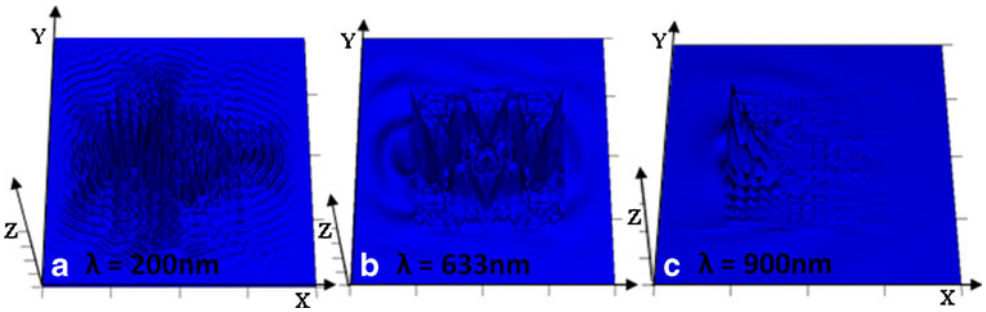

Fig. 3 **a**–**c** Three-dimensional (3D) contour plot of the field distribution of plasmon propagation through the device demonstrating its functioning for inputs λ=200, 633, and 900 nm exhibiting constructive plasmon interference at λ=633 obtained for the optimized parameters of PMZI

Proposed PMZI was scanned over a wavelength region of 200–1,000 nm to obtain propagating characteristics of the device using FDTD method. Perfectly matched layer (PML) boundary conditions are applied with PML width=500 nm along the x, y, and z directions. Average grid size taken along the x- and z-axes are 6.25 nm whereas along the y-axis it is taken as 10 nm. Three-dimensional (3D) contour plot of the field distribution of plasmon propagation through the device is obtained, distinctly representing the intensity of the traversing wavelength and is given in Fig. 3a–c. 3D plots in Fig. 3 demonstrate the functioning of PMZI for input wavelengths: λ=200, 633, and 900 nm exhibiting plasmon interference at λ=633 and thus establishing the findings of the optimized parameters. These observations verify the plasmonic band gap region, which assist the plasmon propagation through the defect, imparting strong spatial confinement.

SPP Interference in Proposed PMZI

It is noticed from Fig. 2 that the input wavelength of λ_a= 200 nm lies outside the band gap region (400–800 nm) offered by the arrayed nanorod–substrate system and therefore λ_a may not be able to propagate through the PMZI defect waveguide, designed in the base structure. This observation is further verified by the results obtained in Fig. 3a, which shows spreading of the input wavelength λ_a in arbitrary directions and does not show confinement for λ_a in the waveguide. As the contour plot in Fig. 3a does not represent well-defined interference pattern, the PMZI fails to be functional for interferometry sensing at input λ_a. Similarly, the PMZI strictly restricts the propagation of wavelength λ_c=900 nm as this wavelength also falls outside the band gap region (Fig. 3c), thereby making the device inoperable at higher wavelengths for the optimized parameters. But for the input wavelength of λ_b=633 nm, it is observed that the plasmon mode advances efficiently (Fig. 3b) exposing strongly confined impeccable plasmon propagation for this input wavelength as λ_b lies within the wavelength region (400–800 nm), i.e., the band gap obtained for the base structure of the proposed design. For λ_b, the proposed PMZI show a well-defined interference pattern, Fig. 3b, allowing accurate measurement of wave parameters; here we see that the input plasmon field intensity split equally into the reference and sensing arms of the interferometer, the plasmons propagate therein the arms and then interfere again constructively at the output end, maintaining the resultant amplitude equal to as that at the input end (analogous to famous Young's double slit interference experiment). The resultant constructive interference at the output for λ_b=633 nm yields same intensity at the output as that at the input which is not obtained in case of λ_a and λ_c. Also, owing to the fact that silver has plasmon frequency in the visible region [15] of the electro-magnetic spectrum—we get optimum propagation for input wavelength of 633 nm formulating it to be the operational wavelength for the interferometer. If we carefully examine the 3D contour, it can be discerned that for the optimized width W, length L_0, arm length L, bend length B, and the bend angle, the PMZI yield constructive interference at the output port and the resultant amplitude at the output port is maintained as that at the input port, demonstrating the plasmon interference during its propagation.

Table 1 Calculated values of wavelength shifts $\Delta\lambda$, sensitivity S, FWHM $\delta\lambda$, and figure of merit FOM obtained for various cancer cell lines

Cancer cell line	n	$\Delta\lambda_1$ (nm)	$\Delta\lambda_2$ (nm)	$\Delta\lambda_3$ (nm)	S_1 (nm/RIU)	S_2 (nm/RIU)	S_3 (nm/RIU)	$\delta\lambda_1$ (nm)	$\delta\lambda_2$ (nm)	$\delta\lambda_3$ (nm)	FOM_1	FOM_2	FOM_3
Jurkat	1.390	4.142	6.796	2.462	2,071	3,398	1,231	20	16	18	103.55	212.37	68.38
HeLa	1.392	5.730	8.300	3.900	2,865	4,150	1,950	22	16	20	130.22	259.36	97.50
PC 12	1.395	10.146	14.010	7.560	3,382	4,670	2,520	30	20	22	112.73	233.50	114.54
MDA	1.399	16.160	20.052	12.404	4,040	5,013	3,101	22	12	22	183.63	417.75	140.95
MCF 7	1.401	10.022	11.356	8.242	5,011	5,678	4,121	24	12	22	208.79	473.16	187.31

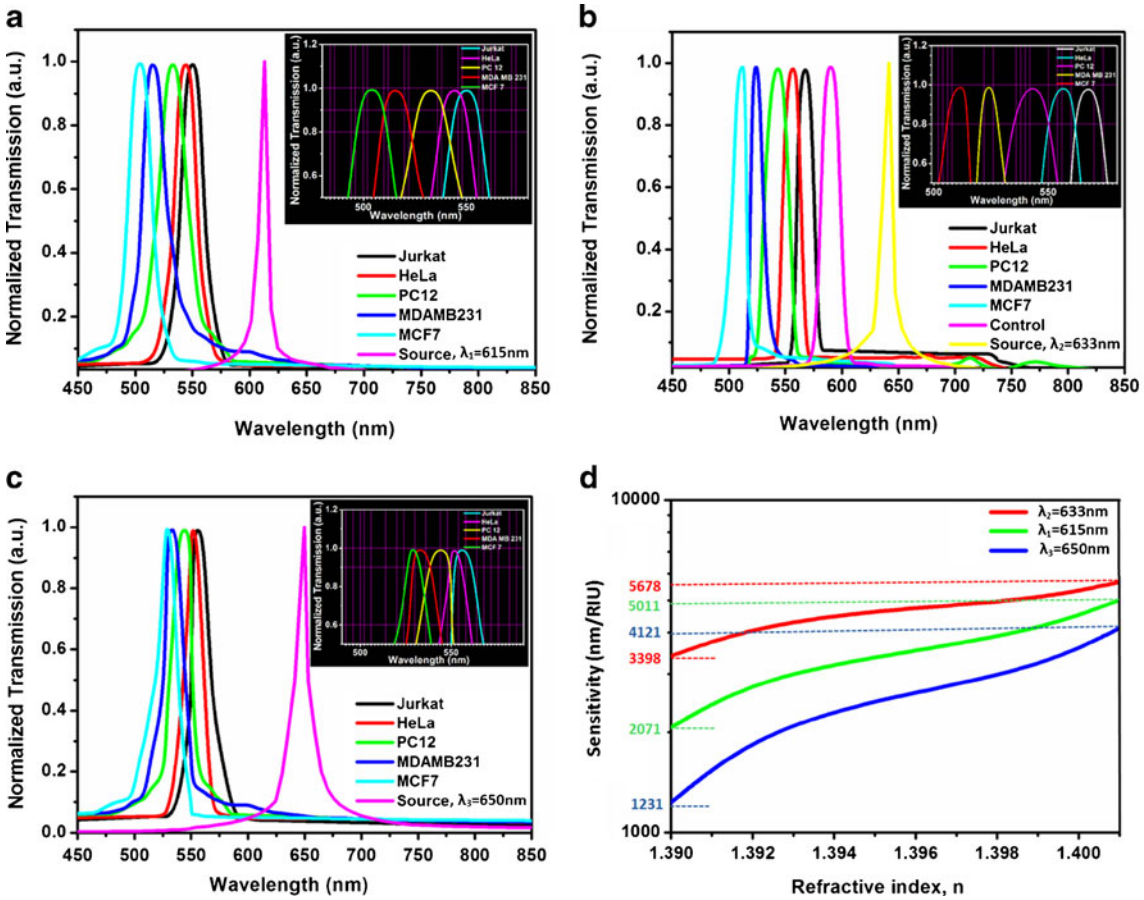

Fig. 4 **a**–**c** Normalized transmission obtained for different carcinoma cell lines representing blue shift with increasing RI for operational wavelength λ_1, λ_2, and λ_3, respectively. **d** Logarithmic variation of sensitivity of the device with change in RI

As the entire device parameters are aptly optimized, it is employed for sensing. Five different cell lines considered for detection are Jurkat (blood/bone marrow cancer cell), HeLa (cervical cancer cell), PC 12 (adrenal gland cancer cell), MDA MB 231(breast cancer cell), and MCF 7 (human breast adenocarcinoma cell). Refractive indices of these malignant cells have been determined by Liang et al. [18]. The RI values of these cancer cell lines have been incorporated in the devised PMZI for detection as summarized in Table 1.

Transmission Characteristics

The spectral distribution for the device is obtained representing normalized transmission for Jurkat, HeLa, PC 12, MDA MB 231, and MCF 7 with the input wavelength of λ_1=615 nm, λ_2=633 nm, and λ_3=650 nm of the visible regime that falls under the allowed frequencies that can traverse through the interferometer and is given in Fig. 4a–c, respectively, for the considered wavelengths. Sharp distinct peaks are obtained for different kinds of cancerous cell lines.

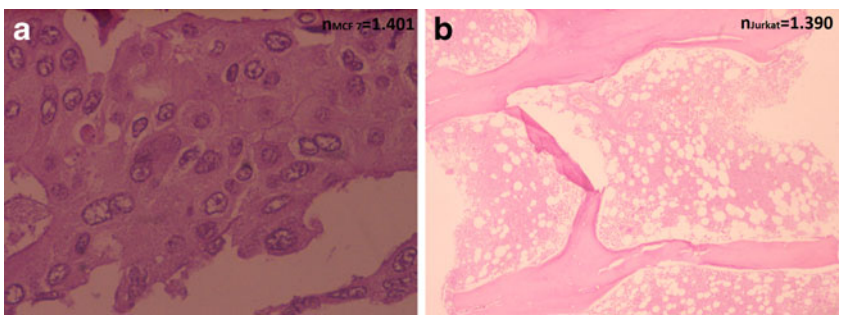

Fig. 5 **a**, **b** Cancer cell line micrographs of breast and blood cells representing dense cell constituents causing augmentation of refractive index

Table 2 Volumetric analysis of the sensor

	Analyte volume 10^{-15} cc	Path difference (μm)	Phase difference (radian)
V_1	0.95	0.124	1.231
V_2	1.90	0.153	1.518
V_3	2.86	0.190	1.886

Increase in refractive index results in blue shift of the spectral lines in each case. The insets in each case in Fig. 4a–c show expanded scale for finer observations. Noticeable spectral shift is achieved and is reported in Table 1 under the columns mentioned as $\Delta\lambda_1$, $\Delta\lambda_2$, and $\Delta\lambda_3$ for the input wavelength of λ_1, λ_2, and λ_3 respectively.

Spectral Sensitivity

It can be seen from Table 1 that remarkable shift is perceived in case of input wavelength λ_2 yielding maximum wavelength shift making it the most suitable operational wavelength for sensing using this PMZI. Spectral sensitivity interrogation is done and determined by using Eq. 1:

$$S = \left|\frac{\Delta\lambda}{\Delta n}\right| \tag{1}$$

where, $\Delta\lambda$ represent shift in wavelength and Δn is change in refractive index. RI sensitivity depends on the operational wavelengths and the calculated sensitivities for λ_1, λ_2, and λ_3 are tabulated in Table 1. Plot of sensitivity in logarithmic scale against refractive index is drawn and is given in Fig. 4d which marks the maximum and minimum value of sensitivity obtained for each input wavelength. It illustrates that maximum sensitivity S_{max}=5678 nm/RIU is obtained for breast cancer cell line MCF 7 and minimum sensitivity S_{min}= 3398 nm/RIU is acquired for blood cancer cell line Jurkat with input wavelength λ_2. Their digital micrograph representing high density of cell content which causes augmentation of refractive index is given in panels a and b of Fig. 5 for breast and blood cancer cell lines, respectively. Enhanced field and strongly confined plasmon modes available for interaction sense the minute change and exhibit noteworthy shift arising due to change in analyte RI. Also, for the control experiment, which involves normal cells (marked "control" in Fig. 4b) in the sensing arm with refractive index 1.35, the PMZI is found to yield a wavelength shift of 41 nm as compared to the cancer cells yielding the wavelength shift of 65, 77, 91, 109, and 121 nm with increasing RI, with respect to the input wavelength λ_2=633 nm (Fig. 4b). So, we conclude this section by asserting that our proposed structure for PMZI efficiently senses the change in refractive index of the order of 10^{-3} and the maximum sensitivity achieved S_{max} is higher than the values reported in previous papers [7, 43, 47] in terms of detection via plasmonic MZI based on non-prism design technique making our SPPBG-enabled PMZI design superior than that of other designs for sensing applications.

Figure of Merit

Further the figure of merit (FOM) is calculated to determine the device performance using Eq. 2 mentioned below:

$$\text{FOM} = \frac{s}{\delta\lambda} \tag{2}$$

where S is the sensitivity and $\delta\lambda$ is the full width at half-maximum (FWHM) of the respective sensing peak. The FWHM values for each cell line are measured from their spectral response and are stated in Table 1 as $\delta\lambda_1$, $\delta\lambda_2$, and $\delta\lambda_3$ for input wavelengths λ_1, λ_2, and λ_3, respectively. These values are used to calculate FOM and have been added in Table 1. It is found that the highest value of FOM obtained in our device is 473 for operational wavelength λ_2 which surpasses the findings reported in previous literature hence making the proposed PMZI highly sensitive, compact, and profound device to be used for detection.

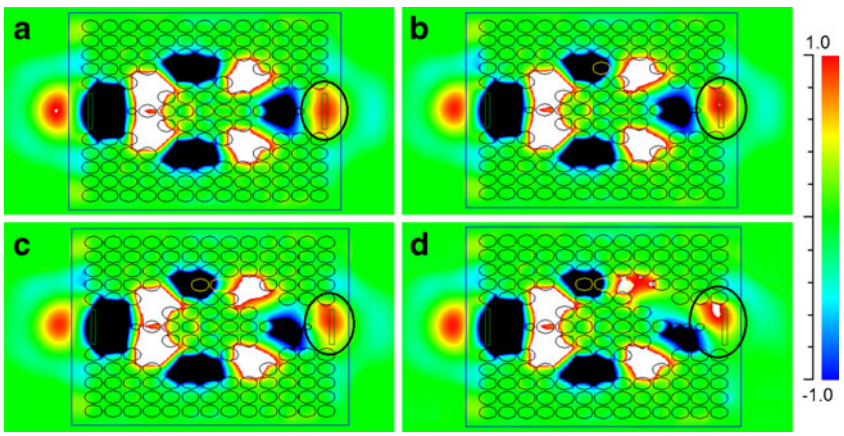

Fig. 6 **a** Electric field profile of propagating mode through the PMZI with no analyte in the sensing arm, i.e., similar environmental condition in the two arms of the PMZI showing the centrally located field profile at the output end. **b**–**d** Represent the effect of increasing analyte volume as V_1, V_2, and V_3, respectively, on the field profile at the output, showing plasmon–analyte interaction

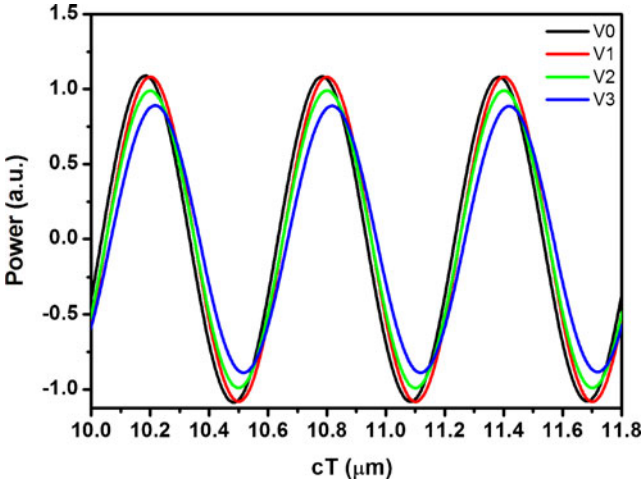

Fig. 7 Power variation with time obtained by varying analyte volume as V_1, V_2, and V_3 yielding path difference and hence the phase shifts for the PMZI

Volumetric Analysis

Volumetric analysis of the proposed PMZI was done to fix the analyte volume to examine the operation of the device with changing volume. Three different analyte volumes V_1, V_2, and V_3 are considered for MCF 7 as summarized in Table 2. Electric field Ey profiles of the propagating mode through the PMZI are obtained for different environmental conditions and displayed in Fig. 6. Figure 6a represents Ey field profile with no analyte volume (V_0) in the sensing arm validating that the similar environmental conditions in the two arms of the PMZI causes centrally located field profile at the output end. It is observed that as the presence of analyte volume increases from volumes V_1 (0.95×10^{-15} cc) to V_3 (2.86×10^{-15} cc) in the sensing arm, the output of the PMZI appears shifted and distorted (see Fig. 6b–d) with maximum distortion in case of V_3 owing to the maximum plasmon–analyte interaction in the sensing arm of PMZI resulting in path difference acquired between the two arms. Power at the output end is assessed for V_0, V_1, V_2, and V_3 and is graphically represented in Fig. 7 which reveals path difference arising due to presence of analyte in the sensing arm. Path difference for each volume is calculated and is tabulated in Table 2, which is further used to calculate the phase difference obtained in each case. From Table 2, we can conclude that volume V_1 is sufficient enough to give rise to significant phase shift.

Table 3 Path difference and phase difference obtained for different cancer cell lines

Cancer cell line	Refractive index n	Path difference (μm)	Phase shift (radian)
Jurkat	1.390	0.0337	0.3351
HeLa	1.392	0.0569	0.5655
PC 12	1.395	0.0739	0.7336
MDA MB 231	1.399	0.0970	0.9634
MCF 7	1.401	0.1244	1.2357

Phase Shift

Fixing analyte volume to V_1, we further investigate the phase shift obtained due to different cancer cell lines considered in our work. For this, power is obtained at the output and plotted against time scale converted into distance. Its graphical representation is given in Fig. 8a with the expanded scale in its inset. This curve demonstrating power is examined and path difference is measured to further calculate the phase shifts as the RI of the cell changes, this variation is exposed in Fig. 8b. Significant phase shift is observed providing a useful scale for RI detection and hence cancer cell differentiation can be easily done. These observations are summarized in Table 3 describing that maximum phase shift of 1.2357 in radian (~71°) is observed for MCF 7 cell line

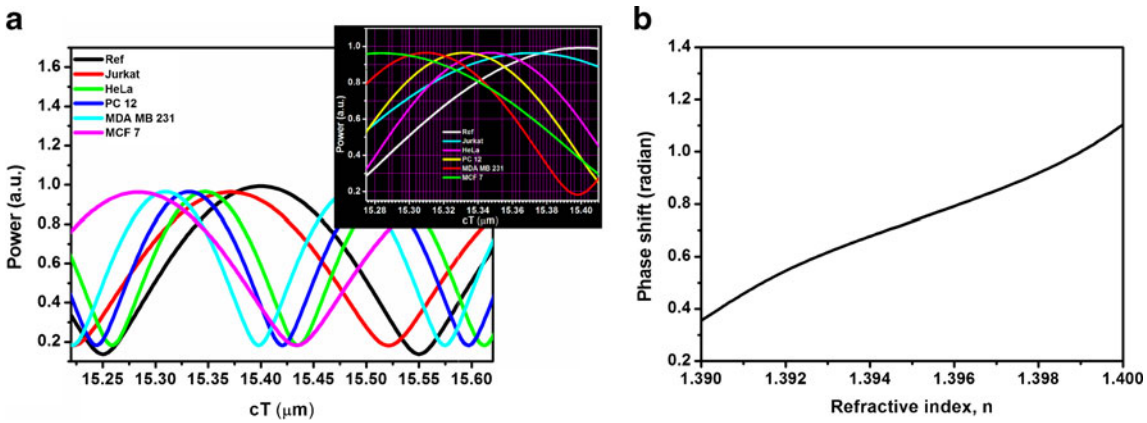

Fig. 8 **a** Variation of power at the output through the span of time. *Inset* shows expanded scale for measuring the shifts. **b** Plot of phase shift with refractive index showing significant change yielding easy detection of carcinoma cell lines

establishing it as a highly sensitive ultra-compact yet simple device for disease diagnosis.

All the observations pronounced above demonstrate enhanced sensing performance of the proposed PMZI and ensures wider application in biosensing. The device can be easily integrated and coupled with other on-chip devices as per demanded requirements. Further improvements can be expected by studying different physical and chemical parameters, quantum effects, etc., which govern device performance.

Conclusion

As the diffraction limit restricts miniaturization of conventional photonic devices, through our present work we have proposed a miniaturized plasmonic Mach–Zehnder interferometer to detect various types of cancer cell lines with high sensitivity using SPPBG effect for waveguidance. The peculiarity of the work is that it innovatively offers an ultra-compact highly sensitive novel device for sensing and overcomes the size limitations of the prism-based SPR sensors. Extensive analysis of the device is done for estimation of SPPBG using PWE method and FDTD method is used to evaluate propagating characteristics of the SPP through PMZI; the results are carefully examined for inferences. Periodic arrangement of metal nanorods offers plasmonic band gap assisting subwavelength confinement of the resultant mode through the defect. Outstanding figure of merit is achieved verifying the device performance. Volumetric analysis is carried out which express that low analyte volume is sufficient to yield noticeable phase shift indicating the proficiency of the proposed PMZI. Thus, the proposed PMZI sensor implemented for classification of cancer cells makes this miniaturized device a promising candidate for practical application in the general areas of sensors and actuators, greatly improving disease diagnosis by combining plasmonics with interferometry.

Acknowledgments The authors greatly acknowledge the initiative and support towards establishment of "TIFAC-Center of Relevance and Excellence in Fiber Optics and Optical Communication at Delhi College of Engineering now Delhi Technological University, Delhi, through Mission Reach Program of Technology Vision 2020, Government of India. Also, we would like to extend our acknowledgement to Dr Anurag Mehta and Mr Sujeet Nath Sinha of Rajiv Gandhi Cancer Institute and Research Center for allowing us to use their resources and carry out the research work in regard of cancer cell lines.

References

1. Bozhevolnyi SI, Boltasseva A, Sondergaard T, Nikolajsen T, Leosson K (2005) Opt Commun 250:328
2. Kim DS, Hohng SC, Malyarchuk V, Yoon YC, Ahn YH, Yee KJ, Park JW, Kim J, Park Q, Lienau C (2003) PRL 91:143901
3. Bozhevolnyi SI, Erland J, Leosson K, Skovgaard PMW, Hvam JM (2001) PRL 86:3008
4. Mekis A, Chen JC, Kurland I, Fan S, Villeneuve PR, Joannopoulos JD (1996) PRL 77:3787
5. Barnes WL, Dereux A, Ebbesen TW (2003) Nature 424:824
6. Wu SY, Ho HP, Law WC, Lin C (2004) Opt Lett 29:2378
7. Gao Y, Gan Q, Xin Z, Cheng X, Bartoli FJ (2011) ACS Nano 5:9836
8. Drezet A, Hohenau A, Stepanov AL, Ditlbacher H, Steinberger B, Aussenegg FR, Leitner A, Krenn JR (2006) Plasmonics 1:141
9. Thomas R, Ikonic Z, Kelsall RK (2012) PNFA 10:183
10. Bozhevolnyi SI, Volkov VS, Devaux E, Laluet JY, Ebbesen TW (2006) Nature 440:508
11. Wahsheh RA, Lu Z, Abushagur MAG (2009) Opt Commun 282: 4622
12. Pu M, Yao N, Hu C, Xin X, Zhao Z, Wang C, Luo X (2010) Opt Express 18:21030
13. Guo X, Qiu M, Bao J, Wiley BJ, Yang Q, Zhang X, Ma Y, Yu H, Tong L (2009) Nano Lett 9:4515
14. Xia Y, Halas NJ (2005) MRS Bull 30:338
15. Lal S, Link S, Halas NJ (2007) Nat Photonics 1:641
16. Choi WJ, Jeon DI, Ahn SG, Yoon JH, Kim S, Lee BH (2011) Opt Express 18:23285
17. Zysk AM, Chaney EJ, Boppart SA (2006) Phys Med Biol 51:2165
18. Liang XJ, Liu AQ, Lim CS, Ayi TC, Yap PH (2007) Sens Act A 133: 349
19. Kosmeier S, Kemper B, Langehanenberg P, Bredebusch I, Schnekenburger J, Bauwens A, Bally GV (2008) Proc SPIE 6991: 6999110
20. Loo C, Lin A, Hirsch L, Lee MH, Barton J, Halas NJ, West J, Drezek R (2004) Tech Cancer Res Treat 3:33
21. Hagness SC, Taflove A, Bridges JE (1999) IEEE Trans Ant Prop 47: 783
22. Zhang G, Long M, Wu ZZ, Yu WQ (2002) World J Gastroenterol 8: 243
23. Suresh S (2007) Acta Biomater 3:413
24. Lekka M, Laidler P, Gil D, Lekki J, Stachura Z, Hrynkiewicz AZ (1999) Eur Biophys J 28:312
25. Guck J, Schinkinger S, Lincoln B, Wottawah F, Ebert S, Romeyke M, Lenz D, Erickson HM, Ananthakrishnan R, Mitchell D, Kas J, Ulvick S, Bilby C (2005) Biophys J 88:3689
26. Katira P, Zaman MH, Bonnecaze RT (2012) Phys Rev Lett 108: 028103
27. Reticker-Flynn NE, Malta DFB, Winslow MM, Lamar JM, Xu MJ, Underhill GH, Hynes RO, Jacks TE, Bhatia SN (2012) Nat Commun 3:1122
28. Lin AWH, Lewinski LA, West JL, Halas NJ, Drezek RA (2005) J Biomed Opt 10:064035
29. El-Sayed IH, Huang X, El-Sayed MA (2005) Nano Lett 5:829
30. Agarwal A, Huang SW, O'Donnell M, Day KC, Day M, Kotov N, Ashkenazi S (2007) J Appl Phys 102:064701
31. Mallidi S, Larson T, Tam J, Joshi PP, Karpiouk A, Sokolov K, Emelianov S (2009) Nano Lett 9:2825
32. Skrabalak SE, Au L, Lu X, Li X, Xia Y (2007) Nanomedicine 2:657
33. Ladd J, Lu H, Taylor AD, Goodell V, Disis ML, Jiang S (2009) Colloids Surf B: Biointerfaces 70:1
34. Backman V, Wallace MB, Perelman LT, Arendt JT, Gurjar R, Müller MG, Zhang QZonios G, Kline E, McGillican T, Shapshay S, Valdez T, Badizadegan K, Krawford JM, Fitzmaurice M, Kabani S, Levin HS, Seiler M, Dasari RR, Itzkan I, Dam JV, Feld MS (2000) Nature 406:35
35. Barer R (1957) J Opt Soc Am 47:545
36. Song WZ, Zhang XM, Liu AQ, Lim CS, Yap PH, Hosseini HMM (2006) Appl Phys Lett 89:203901
37. Lue N, Popescu G, Ikeda T, Dasari RR, Badizadegan K, Feld MS (2006) Opt Lett 31:2759

38. Chin LK, Liu AQ, Lim CS, Zhang XM, Ng JH, Hao JZ, Takahashi S (2007) Appl Phys Lett 91:243901
39. Liang W, Huang Y, Xu Y, Lee RK, Yariv A (2005) Appl Phys Lett 86: 151122
40. Homola J (2003) Anal Bioanal Chem 377:528
41. Anker JN, Hall WP, Lyandres O, Shah NC, Zhao J, Duyne RPV (2008) Nat Mater 7:442
42. Dillu V, Sinha RK (2013) Indian Patent Application No. 1168/DEL/ 2013 CBR No. 3985
43. Gan Q, Gao Y, Bartoli FJ (2009) Opt Express 17:20747
44. Johnson PB, Christy RW (1972) Phys Rev B 6:4370
45. Dillu V, Shruti, Srivastava T, Sinha RK (2013) Physica E 48:75
46. Rajput M, Sinha RK (2010) Appl Phys B 98:99
47. Mayer KM, Hafner JH (2011) Chem Rev 111:3828

JOURNAL OF APPLIED PHYSICS **114**, 234305 (2013)

Enhanced Fano resonance in silver ellipsoidal plasmonic crystal cavity

Venus Dillu and R. K. Sinha[a)]
Department of Applied Physics, TIFAC—Centre of Relevance and Excellence in Fiber Optics and Optical Communication, Delhi Technological University (Formerly: Delhi College of Engineering), Bawana Road, Delhi 110042, India

(Received 2 August 2013; accepted 2 December 2013; published online 19 December 2013)

Enhancement in the asymmetric line shape of Fano resonance is observed and extensively examined for cavities in plasmonic crystals of ellipsoidal silver nanoparticles with hexagonal arrangement. Scattering models for ellipsoidal and cylindrical nanoparticles are compared and it is found that the spectral interference between the cavity mode and the background scattering mode results in a sharp asymmetric peak, which is the defining characteristic of Fano resonance. It is found that the cavity in ellipsoidal nanoparticles yields high transmission at a wavelength of 1600 nm compared with its cylindrical counterpart. Higher harmonic generation is also observed, which confirms the ultrahigh cavity response in ellipsoidal nanoparticles. The effect of power variation on the Fano resonance profile is described, and its application in the field of switching is explored. In addition, the influence of mutual interparticle coupling on Fano line shapes for transverse electric and transverse magnetic polarization is reported. The extraordinary rise in asymmetric line shapes of the Fano resonance promises profound applications in the field of sensing, switching, and lasing devices.
 [http://dx.doi.org/10.1063/1.4851775]

I. INTRODUCTION

Fano resonance, discovered by Ugo Fano, is a resonant scattering phenomenon that gives rise to asymmetric line shapes due to the interaction of discrete excited states with continuum excited states sharing same energy level.[1] The response of an oscillating system driven at an external frequency, ω, about its resonant frequency, ω_0, is symmetric and the intensity, I, for the system is approximated by the universally accepted Lorentzian function given below

$$I(\omega) \propto \frac{\left(\frac{\gamma}{2}\right)^2}{(\omega-\omega_0)^2+\left(\frac{\gamma}{2}\right)^2}, \tag{1}$$

where γ is the width of resonance about resonant frequency, ω_0.

In contrast to the Lorentzian function, the distinct asymmetric Fano resonance shape is given by the following function:

$$I \propto \frac{(F\gamma+\omega-\omega_0)^2}{(\omega-\omega_0)^2+\gamma^2}, \tag{2}$$

where F is the Fano parameter describing the degree of asymmetry.[2] Fano resonance is generally specific to quantum systems that involve auto-ionization of atoms due to interference of excited leaky modes with incoming continuum radiation. This interference (or auto-ionization) gives rise to asymmetric profile characteristics of the Fano resonance. By using the comprehensive approach developed by Fano, it is possible to predict the position as well as the width of the Fano resonance.[2,3] Fano resonance was first observed in 1902 as Wood's anomalies in gratings.[4] Subsequently, this phenomenon has been meticulously studied and had been observed in quantum dots, quantum wires,[5,6] dielectric and metallic photonic crystals,[7,8] prism-coupled micropillars,[9] plasmonic nanostructures,[2] metamaterials,[10] self-assembled nanoparticle clusters,[11] individual plasmonic nanocavities,[12] and symmetry breaking disk-ring nanostructures,[13] among others. Because this unique resonance arises from the interference between two or more oscillators, the system has intrinsic sensitivity towards local changes,[2] making it well suited for application in chemical and biological sensors. Large shifts in the resonance frequency of the system are the basis of its sensing capability. The characteristic Fano resonance profile also has promising applications in lasing, switching, slow-light devices, and plasmon-induced transparency. To realize these prospective applications, novel plasmonic designs with improved properties are required, for example, with respect to transmission, propagation, and loss characteristics.

Clusters of strongly interacting metallic nanoparticles support strong Fano resonance arising owing to the interference between the superradiant bright mode and the subradiant dark mode of the quantum system, which can be designed to achieve the desired optical response. The electromagnetic interactions within such a quantum system influence the line shape of the resultant plasmonic Fano profile. Plasmonic dimers, dolmen structures, metallic double gratings, quadrumers, and heptamers with different cross-sectional areas have been found to exhibit Fano resonance, which can be manipulated by tailoring the number and position of the monomeric units.[11,14–17] However, in simpler clusters like dimers and trimers, the electric dipole resonance subdues the Fano resonance.[11] This limitation is addressed

[a)]Author to whom correspondence should be addressed. Electronic mail: dr_rk_sinha@yahoo.com

by adding structural complexity or breaking the symmetry to induce bright and dark modes available for interaction to produce Fano resonance. Oligomers such as heptamers promote Fano resonance owing to electromagnetic coupling within the particles without breaking the symmetry of the system, because the dark and bright modes are not completely orthogonal in Oligomers.[11,14] Notwithstanding earlier work done in this field, different types of metal nanoparticles need to be studied to ascertain the factors that control and influence Fano resonance in these systems. Therefore, we explore herein the Fano behavior of the plasmonic crystal cavity formed in silver ellipsoidal nanoparticles and its cylindrical counterpart. We report an enhancement and shape dependence of the asymmetric Fano line shape and the observation of higher harmonic generation (HHG), which leads to ultrahigh transmission. Further, the power dependence of the Fano line shape was shown to be suitable for switching applications and the influence of transverse electric (TE) and transverse magnetic (TM) polarization on the Fano resonance profile was investigated. The study was conducted using a scattering model along with the finite difference time domain (FDTD) method.

II. SCATTERING MODEL FOR SILVER ELLIPSOIDAL AND CYLINDRICAL PLASMONIC CRYSTAL

We observed remarkable enhancement in asymmetric Fano resonance line shape, exhibited by the nanocavity introduced in hexagonally arranged ellipsoidal silver nanoparticles [see Figure 1 inset (iii)] as compared to cylindrical silver nanorods (CSNs). We have used the following scattering model to validate this observation.

Particles having ellipsoidal shape are smooth with no edges or corners which result into in-phase scattering of incident light unlike that of their cylindrical counterparts. The surface of an ellipsoid is defined by the following standard equation:

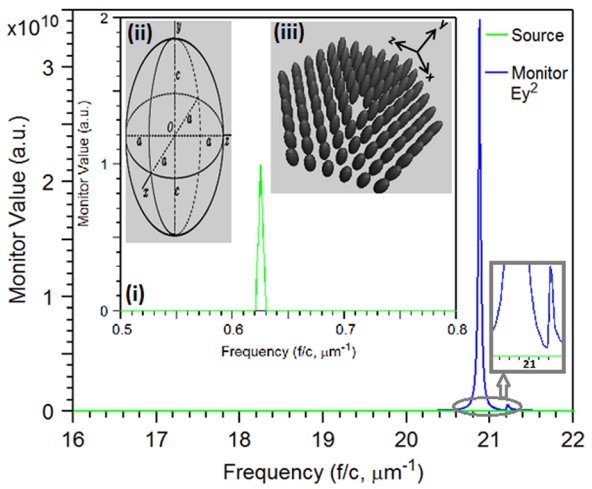

FIG. 1. Cavity response of hexagonally arranged ESN, the zoomed out illustration shows the asymmetry in the output response. Inset (i) displays the symmetric input source profile; inset (ii) presents the semi-axes "a," "b," and "c" of the ellipsoid and inset (iii) presents cavity in the hexagonal arrangement of the silver ellipsoids.

$$\frac{x^2}{a^2}+\frac{y^2}{b^2}+\frac{z^2}{c^2}=1, \tag{3}$$

where a, b, and c are the semi-principle axes of the ellipsoid in Cartesian coordinates (x, y, z) system.[15] However, ellipsoidal coordinates (ξ, η, ζ) are preferred to determine the dipole moment and potential of an ellipsoidal particle in a uniform electric field. Therefore the surface of an ellipsoid in ellipsoidal coordinates (ξ, η, ζ) is defined as

$$\frac{x^2}{a^2+\xi}+\frac{y^2}{b^2+\xi}+\frac{z^2}{c^2+\xi}=1, \quad -c^2<\xi<\infty \tag{4a}$$

$$\frac{x^2}{a^2+\eta}+\frac{y^2}{b^2+\eta}+\frac{z^2}{c^2+\eta}=1, \quad -b^2<\eta<-c^2 \tag{4b}$$

$$\frac{x^2}{a^2+\zeta}+\frac{y^2}{b^2+\zeta}+\frac{z^2}{c^2+\zeta}=1, \quad -a^2<\zeta<-b^2. \tag{4c}$$

Also to any point (x, y, z) in Cartesian coordinates, there corresponds one set of ellipsoidal coordinates (ξ, η, ζ) which determine eight points, symmetrically located in each of the octants as given below[15]

$$x^2=\frac{(a^2+\xi)(a^2+\eta)(a^2+\zeta)}{(b^2-a^2)(c^2-a^2)}, \tag{4d}$$

$$y^2=\frac{(b^2+\xi)(b^2+\eta)(b^2+\zeta)}{(a^2-b^2)(c^2-b^2)}, \tag{4e}$$

$$z^2=\frac{(c^2+\xi)(c^2+\eta)(c^2+\zeta)}{(a^2-c^2)(b^2-c^2)}. \tag{4f}$$

Now, for a homogeneous ellipsoid placed in a uniform electric field aligned along z-axis, the potential Φ has symmetric properties as shown below

$$\Phi(x,y,z)=\Phi(-x,y,z)=\Phi(x,-y,z)=\Phi(-x,-y,z)$$

and

$$\Phi(x,y,-z)=\Phi(-x,y,-z)=\Phi(x,-y,-z)=\Phi(-x,-y,-z). \tag{5a}$$

Therefore, potential in only two octants having positive and negative z values is to be considered with the required condition that potential and its derivative are continuous on the plane $z=0$. So, we choose the octant in which the value of x, y, z is positive. Let Φ_0 denote the potential due to the external field E_0, whereas Φ_1 and Φ_2 denote the potential inside and outside the ellipsoid, respectively. Further, let Φ_p be the perturbing potential caused by the ellipsoid. Then, Φ_2 can be expressed as the superposition of Φ_0 and Φ_p, with Φ_0 given as

$$\Phi_0=-E_0\left[\frac{(c^2+\xi)(c^2+\eta)(c^2+\zeta)}{(a^2-c^2)(b^2-c^2)}\right]^{1/2}. \tag{5b}$$

At sufficiently large distance from the ellipsoid the perturbing potential Φ_p is negligible and we observe that when $\xi \gg a^2$ the limit,

$$\lim_{\xi\to\infty} \Phi_p = 0. \tag{5c}$$

Also, it is required that at the boundary of the ellipsoid, the potential should be continuous

$$\Phi_1(0, \eta, \zeta) = \Phi_0(0, \eta, \zeta) + \Phi_p(0, \eta, \zeta). \tag{5d}$$

Hence, the Laplace's equation to accurately describe the electric potential Φ in ellipsoidal coordinates is obtained and given as follows:

$$\begin{aligned}\nabla^2\Phi = {} & (\eta-\zeta)f(\xi)\frac{\partial}{\partial\xi}\left\{f(\xi)\frac{\partial\Phi}{\partial\xi}\right\} \\ & + (\zeta-\xi)f(\eta)\frac{\partial}{\partial\eta}\left\{f(\eta)\frac{\partial\Phi}{\partial\eta}\right\} \\ & + (\xi-\eta)f(\zeta)\frac{\partial}{\partial\zeta}\left\{f(\zeta)\frac{\partial\Phi}{\partial\zeta}\right\} = 0,\end{aligned} \tag{5e}$$

where Φ is the scalar potential and expression f is defined for a variable q as

$$f(q) = \left\{\left(q+a^2\right)\left(q+b^2\right)\left(q+c^2\right)\right\}^{1/2}. \tag{5f}$$

Now in order to solve the Laplace's equation (5e), using Eq. (5b) we assumed that the potentials Φ_I and Φ_p are of the form

$$\Phi(\xi, \eta, \zeta) = F(\xi)\left\{\left(c^2+\eta\right)\left(c^2+\zeta\right)\right\}^{1/2} \tag{5g}$$

and it follows from Eq. (5e) that the function F(ξ) satisfies the ordinary differential equation,

$$f(\xi)\frac{d}{d\xi}\left\{f(\xi)\frac{dF}{d\xi}\right\} - \left(\frac{a^2+b^2}{4}+\frac{\xi}{2}\right)F(\xi) = 0, \tag{5h}$$

yielding a solution of the form

$$F_1(\xi) = \left(c^2+\xi\right)^{1/2}, \tag{5i}$$

which is verified by substituting it in Eq. (5h) and follows from the fact that Eq. (5b) satisfies the Laplace's equation (5e).

A second linear independent solution to Eq. (5h) is obtained by integrating Eq. (5i),

$$F_2(\xi) = F_1(\xi)\int_{\xi}^{\infty}\frac{dq}{F_1^2(q)f(q)}, \tag{5j}$$

with the property $\lim_{\xi\to\infty} F_2(\xi) = 0$.

The function F_1 is not compatible with the required condition given in Eq. (5c); therefore, the perturbing potential of the ellipsoidal particle is given as

$$\boldsymbol{\Phi_p}(\boldsymbol{\xi}, \boldsymbol{\eta}, \boldsymbol{\zeta}) = \boldsymbol{C_2 F_2}(\boldsymbol{\xi})\left\{\left(\boldsymbol{c}^2+\boldsymbol{\eta}\right)\left(\boldsymbol{c}^2+\boldsymbol{\zeta}\right)\right\}^{1/2} \tag{5k}$$

and for the potential inside the particle to be finite at the origin, we must have

$$\boldsymbol{\Phi}_1(\boldsymbol{\xi}, \boldsymbol{\eta}, \boldsymbol{\zeta}) = \boldsymbol{C}_1\boldsymbol{F}_1(\boldsymbol{\xi})\left\{\left(\boldsymbol{c}^2+\boldsymbol{\eta}\right)\left(\boldsymbol{c}^2+\boldsymbol{\zeta}\right)\right\}^{1/2}, \tag{5l}$$

where C_1 and C_2 are constants. Therefore, we get the field inside the particle to be uniform and aligned parallel to the applied field.

The boundary condition given in (5d) yields an equation in constants C_1 and C_2 as mentioned below

$$C_2\int_0^{\infty}\frac{dq}{(c^2+q)f(q)} - C_1 = \frac{E_0}{\left\{(a^2-c^2)(b^2-c^2)\right\}^{1/2}}. \tag{5m}$$

And the requirement that the normal component of the displacement vector be continuous at the boundary of the particle and the medium yields the second equation,

$$\begin{aligned}&\varepsilon_m C_2\left[\int_0^{\infty}\frac{dq}{(c^2+q)f(q)} - \frac{2}{abc}\right] - \varepsilon_1 C_1 \\ &\quad = \frac{\varepsilon_m E_0}{\left\{(a^2-c^2)(b^2-c^2)\right\}^{1/2}}.\end{aligned} \tag{5n}$$

This gives us the required potential inside and outside the particle as follows:

$$\Phi_1 = \frac{\Phi_0}{1+\dfrac{L_3(\varepsilon_1-\varepsilon_m)}{\varepsilon_m}}, \tag{5o}$$

$$\Phi_p = \Phi_0\frac{\dfrac{abc}{2}\dfrac{(\varepsilon_m-\varepsilon_1)}{\varepsilon_m}\displaystyle\int_{\xi}^{\infty}\frac{dq}{(c^2+q)f(q)}}{1+\dfrac{L_3(\varepsilon_1-\varepsilon_m)}{\varepsilon_m}}, \tag{5p}$$

where

$$L_3 = \frac{abc}{2}\int_0^{\infty}\frac{dq}{(c^2+q)f(q)}. \tag{5q}$$

Equations (5o) and (5p) give the potential at all points in space and is a consequence of the particle symmetry.

In a similar way, the solution for potential inside and outside the cylindrical particles can be obtained at all points in space. The details have been exhaustively given in Bohren and Huffman[15] which also describes the polarizability tensor and the scattering matrix. It is inferred from the scattering matrix that scattering is attributed to the particles which are not spherically symmetric and an ellipsoid can be easily approximated to sphere for a = b = c, unlike cylinders.[15] Therefore, ellipsoidal particles are more likely to result into in-phase scattering as compared to cylindrical particles.

The inference of the scattering model discussed above is that the shapes of the particles have noteworthy influence on the scattered waves. The resultant wave scattered in a given direction by a particle is due to the interference of the scattered waves from the entire volume. Thus we conclude that the maximum scattered intensity is obtained when angle between the scattering surface and the incident field is small.

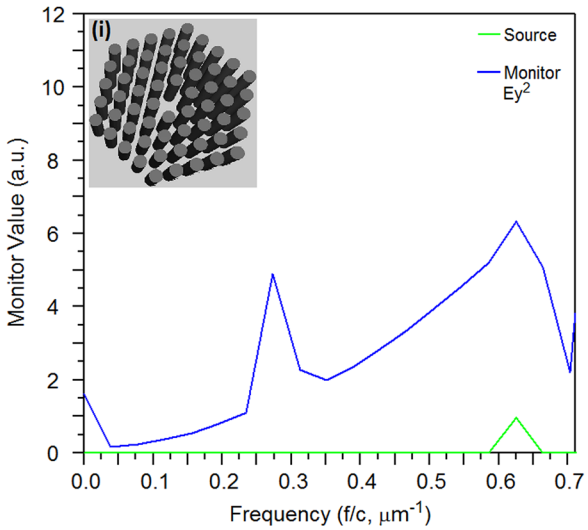

FIG. 2. Cavity response of hexagonally arranged CSN with inset (i) presenting the arrangement of the cylindrical nanorods.

With this qualifier, we compare and study the in-phase scattering in ellipsoidal geometry vis-à-vis cylindrical geometry.

III. FDTD METHOD

Maxwell's equations are solved to obtain resultant electromagnetic field for a plasmonic system, as usually followed for the photonic structures. Mie scattering theory is often used for providing rigorous solution for the Maxwell's equation for spherical nanoparticles, but to model non-spherical geometries and nanostructures of different shapes, FDTD method is employed. This method helps in evaluating the electromagnetic fields within a given structure as a function of time, in a finite domain, on a spatial grid. As our structure comprises of nanorod geometry, we have applied three-dimensional FDTD computational method to numerically assess the temporal evolution of electromagnetic field. The FDTD simulations were performed using perfectly matched layer (PML) boundary conditions with PML width of 200, 500, and 175 nm and average grid size of 25.0, 62.5, and 20.0 nm along the x, y, and z axes, respectively.

IV. STRUCTURE

We considered hexagonally-arranged prolate ellipsoids with axes $a = b = 130$ nm, and $c = 500$ nm (with a dielectric constant $\varepsilon = \varepsilon_i + i\varepsilon_r = -110.143 + 8.807i$, corresponding to the input wavelength of 1600 nm). The background index (n) was 1 and ε varies with the wavelength. The ellipsoids were arranged to have a semi-axis c oriented along the vertical plane of the cavity located at the center of the plasmonic crystal [see Figure 1, inset (ii)]. This arrangement increases the coherent electromagnetic coupling within the particles that interferes destructively with the cavity mode resulting in Fano resonance. We used the technique of adding identical ellipsoidal silver nanoparticles with periodicity of 400 nm. This leads to the formation of large clusters, which creates dark modes that intensify the Fano resonance.[16] The extinction properties and transmission characteristics of the cavity were then explored. The dependence of the Fano line shape on the shape of the nanoparticles is discussed and compared for ellipsoidal silver nanorods (ESN) and CSNs. We assess the important observation of distinct wavelength bands sustaining Fano resonance in the ESN cavity and report the application of switching in the proposed geometry. We further examine the effect of light polarization on the line shape of Fano resonance, taking into account TE and TM polarized light.

V. RESULTS AND DISCUSSION

A. Ultrahigh transmission in the ellipsoidal silver nanorod cavity

The asymmetry observed in the response of the cluster results from the introduction of the nanocavity and the characteristic ellipsoid shape. The output can be tuned from the visible to the IR regime of the electromagnetic spectrum. The asymmetric line shape of the observed plasmonic Fano resonance can be described by a general formula based on Maxwell's equation derived by Gallinet and Martin,[18] which includes the contribution of electromagnetic interactions

$$\sigma_a(\omega) = \frac{\left(\frac{\omega^2 - \omega_a^2}{2W_a\omega_a} + q\right)^2 + b}{\left(\frac{\omega^2 - \omega_a^2}{2W_a\omega_a}\right)^2 + 1}, \tag{6}$$

where ω_a is the resonance frequency, W_a is the spectral width in frequency units, q is the asymmetry parameter, and b is the damping parameter. This equation describes Fano resonance for lossy materials in defined plasmonic nanostructures.

We first examined the response of a cavity introduced in CSNs with a hexagonal arrangement [Figure 2 inset (i)] using the FDTD method for scattered waves, which was successfully employed by Powell *et al.* for controlling the scattering of plasmonic nanoparticles.[19] We now compare these results with those obtained from the cavity in the ESNs [Figure 1 inset (iii)] using the 3D FDTD computational

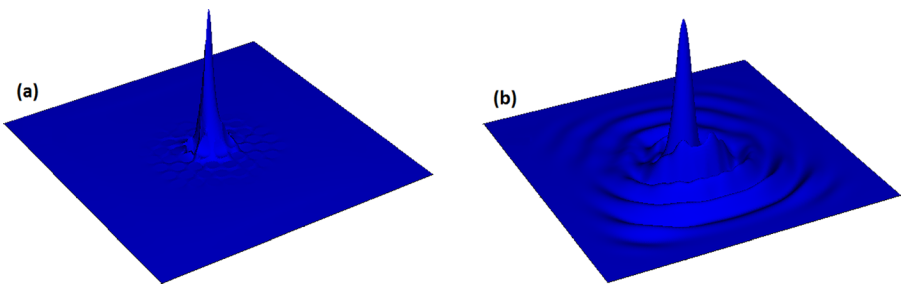

FIG. 3. 3D contour plot of the field distribution in the cavity formed in (a) ESN and (b) CSN.

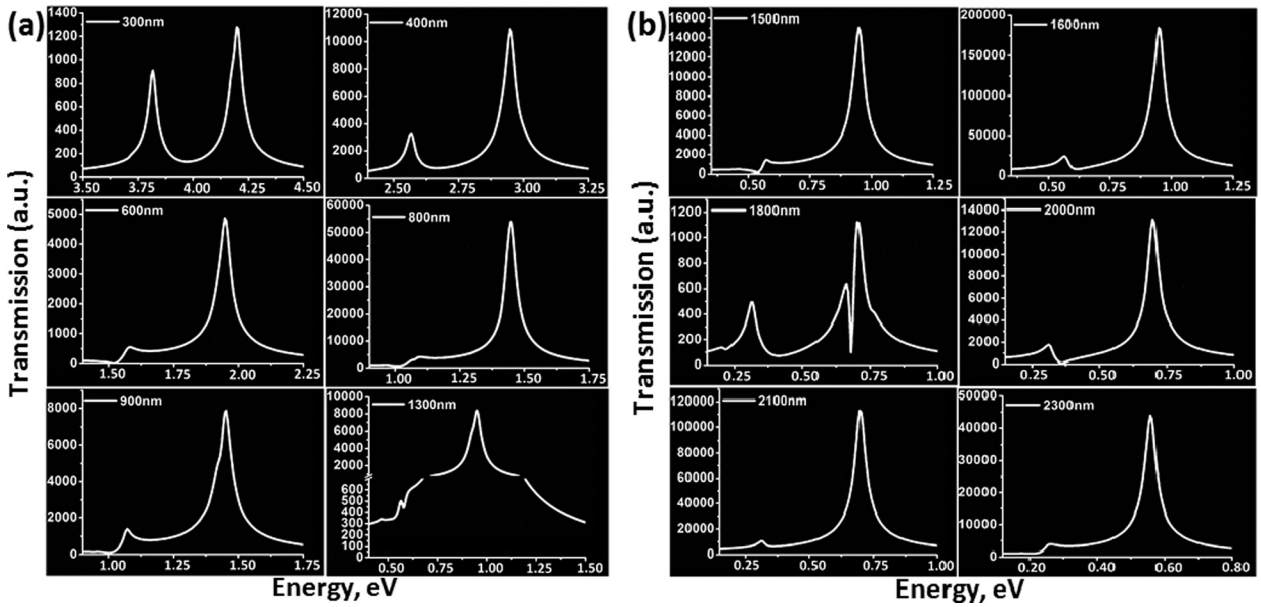

FIG. 4. (a) and (b) Transmission characteristics (1-Extinction; for normalized output) of the ESN cavity for different input wavelength presenting the variation in Fano lineshapes.

method. In both cases, asymmetric output curves are observed (blue curves in Figures 1 and 2), in contrast to the symmetric source profile shown as the green curves in Figure 1 (inset (i)) and Figure 2. These output asymmetric curves represent the unique characteristic of Fano resonance.

Now, we define the transmission $T = 1 - E$, where T is the transmission and E is the extinction, which includes losses due to absorption A and scattering S of the cavity. It is observed that the transmission in the case of ESNs is extraordinarily high (Figure 1) in comparison to CSN (Figure 2). This ultrahigh transmission can be attributed to the geometry of ESNs, the cross-sectional area ($\sigma_{\text{prolate ESN}} = \pi a^2$) of which varies smoothly as semi-axis $a = b$ decreases gradually from $a = a_{\max}$ to $a = 0$ and semi-axis c varies from $c = 0$ to $c = c_{\max}$. This is in contrast to the sudden boundary change in the case of CSNs at $c = c_{\max}$, which causes extreme scattering losses. The absorption losses are negligible in both cases, thereby making scattering the main factor that contributes to the extinction. Therefore, these observations validate the distinct shape enhancement of the asymmetric line shape of Fano resonance in ESNs, in contrast to CSNs, due to the interference of the superradiant bright cavity mode and the subradiant dark mode. This is also evident in the 3D contour plots of the field distribution in the cavities formed in ESNs and CSNs [see Figures 3(a) and 3(b)]. We studied the transmission characteristics of the ESN nanocavity extensively for input wavelengths ranging from the ultraviolet to infrared domains of the electromagnetic spectrum, to

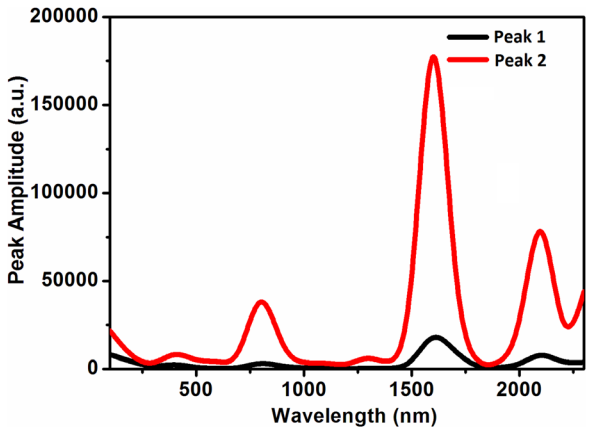

FIG. 5. Spectral variation of peak amplitude for the ESN cavity highlighting switching application.

TABLE I. Peak amplitude values obtained for peaks 1 and 2.

Wavelength (nm)	Peak 1 (a.u.)	Peak 2 (a.u.)
100	8195.91	21637.04
200	4150.61	6232.61
300	910.58	1277.39
400	3284.35	10887.45
500	534.00	4001.24
600	551.93	4861.58
700	231.15	1519.85
800	4238.18	54694.67
900	1382.95	7869.13
1000	716.09	2776.31
1100	414.84	3917.64
1200	332.44	1322.46
1300	502.39	8409.09
1400	332.27	1248.81
1500	1412.12	15042.29
1600	23699.73	184840.60
1700	9740.62	29054.09
1800	631.10	1120.83
1900	758.33	2368.74
2000	1758.96	13138.58
2100	10367.99	113064.20
2200	3028.58	3360.73
2300	3861.49	43866.16

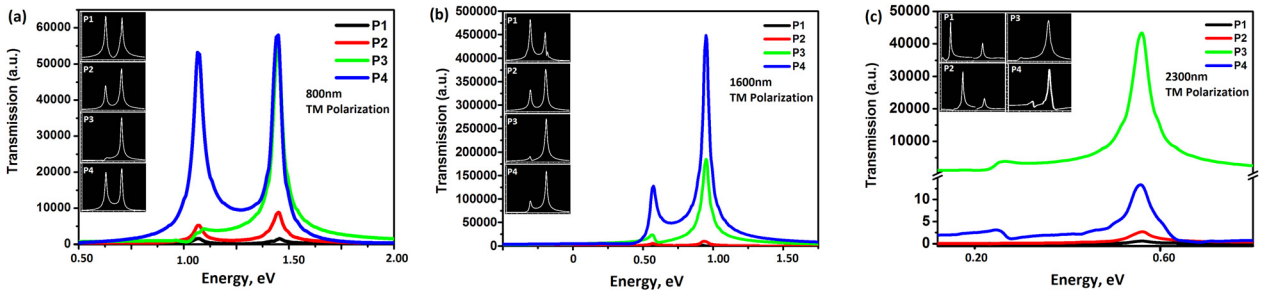

FIG. 6. (a), (b), and (c) Power dependence of Fano lineshapes showing the adaptation of resonance profile with varying input power. TM polarization establish strong mutual coupling resulting in distinct Fano profile.

determine the decisive and controlling parameters in this system. Characteristic Fano curves are obtained for different input wavelengths, as shown in Figures 4(a) and 4(b). These curves reveal interesting behavior of the ESN cavity: as the input wavelength increases, the transmission through the cavity also increases until 800 nm, after which it decreases until 1300 nm. Between 1300 and 1600 nm, there is a steep rise in transmission, which is followed by a fall at 1800 nm and again a rise at 2100 nm. This behavior is discussed in further detail with respect to Figure 5 later in Sec. V B. All the curves are characterized by a short peak (Peak 1) followed by a central peak (Peak 2); these peaks represent the asymmetric Fano profile. The maximum transmittance is obtained at 1600 nm with peak values of 23699.73 and 184840.60 (arbitrary units) for Peak 1 and Peak 2, respectively [see Table I and Figure 4(b)]. This indicates that the considered ESN is suitable for applications in lasing and for plasmon-induced transparency. The peak values obtained in each case are tabulated in Table I and the variation of peak amplitude with wavelength is presented in Figure 5.

B. HHG

The ESN cavity response demonstrated in Figure 5 reveals bands which reflect significant Fano resonance centered at $\lambda_1 = 800$ nm, $\lambda_2 = 1600$ nm, and $\lambda_3 = 2100$ nm. Upon closer inspection, these central wavelengths reveal an important result. The peak wavelengths of the second and third bands (λ_2 and λ_3) are exactly twice and approximately three times that of the first band (λ_1). The formation of bands at regular intervals appears to be related to geometry-dependent nonlinear optical phenomena such as sum/difference frequency generation, that is, frequency mixing processes,[20,21] which lead to significant Fano resonance. Moreover, when we closely analyze the response of the ESN cavity shown in Figure 1, we find that for an input frequency of $1.875 \times 10^8\ s^{-1}$ (corresponding to $0.625\ \mu m^{-1}$; green curve in the inset (i) of Figure 1), the cavity transmits a frequency of $62.7 \times 10^8\ s^{-1}$ (corresponding to $20.9\ \mu m^{-1}$; blue curve in Figure 1). Thus, the output frequency is approximately 33 times the input frequency, confirming the occurrence of HHG[22,23] and the storing of energy at higher frequencies. Therefore, we infer that HHG also contributes to ultrahigh amplification of the input signal in ESNs but not for CSNs (see Figure 2) resulting in the shape-enhanced Fano resonance in ESN cavity.

C. Power dependence and switching application in the ESN cavity

Now we turn our attention to an important application of the power-dependent behavior of the ESN cavity. The difference in the amplitudes of Peak 1 and Peak 2 can be exploited for switching applications. From the curves in Figure 5, we identify three peaks (i.e., 800, 1600, and 2300 nm) suitable for switching applications because of their different peak amplitudes. We varied the input power of the ESN cavity because increasing the power leads to remarkable nonlinear transitions. By varying the power, the line shape of the Fano resonance can also be controlled by enhancing the continuum transition rate to match the saturated discrete level transition.[24] Four different input powers viz. 0.01, 0.1, 1.0, and 10 mW termed P_1, P_2, P_3, and P_4, respectively, were applied in the ESN cavity. The effect of the input power on the transmission spectrum at the wavelengths $\lambda = 800$, 1600, and 2300 nm is shown in Figures 6(a)–6(c), respectively. The ratios of the peak amplitudes, i.e., Γ = Peak 2/Peak 1, are summarized in Table II. At 800 nm for power P_1, Peak 1 is larger than Peak 2 (i.e., $\Gamma < 1$) but as the input power is increased to P_2 and above, the amplitude of Peak 1 decreases and the amplitude of Peak 2 increases, such that $\Gamma > 1$. The maximum value of Γ (12.91) is obtained for input power P_3, thereby making this the optimum operating power to achieve maximum switching efficiency in the proposed ESN. The lower switching efficiency for power P_4 may have been due to the power applied to the cavity being exceeding the tolerance limit of the structure. At power P_3, the values of Γ obtained at 1600 and 2300 nm were 7.79 and 11.36, respectively. From these observations we conclude that the best switching capability of the ESN cavity is obtained for a wavelength of 800 nm at a power of 1.0 mW.

TABLE II. Ratio of peak amplitudes Γ = Peak 2/Peak 1 for different input power P_1, P_2, P_3, and P_4.

Wavelength (nm)	P_1	P_2	P_3	P_4
800	0.95	1.71	12.91	1.05
1600	0.68	1.80	7.79	3.52
2300	0.43	0.22	11.36	3.85

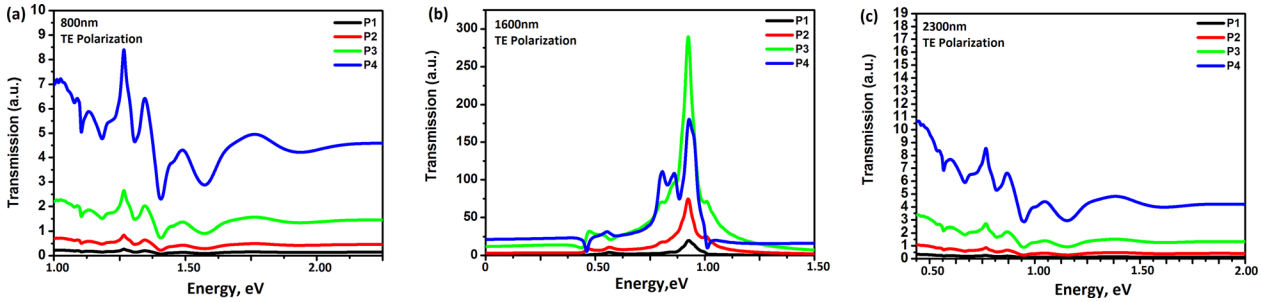

FIG. 7. Effect of TE polarization on the Fano lineshapes validating weak mutual coupling.

D. Effect of polarization

Finally, we discuss the dependence of polarization of the incident light on the line shape of Fano resonance. Plots for TM and TE polarized light at different input powers for $\lambda = 800$, 1600, and 2300 nm are given in Figures 6 and 7, respectively. For TM polarization, the electric field component is parallel to the longitudinal semi-axis "c" of the ellipsoids resulting in the alignment of the charges along the y axis. This, in turn, results in strong mutual coupling of the electrical field components between the ellipsoids and, hence, coherent coupling to the radiation continuum. Accordingly, for TM polarization, well-defined, distinct Fano resonance line shapes are obtained, as illustrated in Figures 6(a)–6(c). However, for TE polarization, the electric field is parallel to the shorter semi-axis "a," which is transverse to the longitudinal direction. This results in weak mutual coupling and multiple random peaks in the transmission response of the cavity, as presented in Figures 7(a)–7(c). These results have therefore demonstrated that the Fano line shape is polarization dependent.

VI. CONCLUSION

We have extensively investigated the Fano resonance in an ellipsoidal nanoparticle cavity. A scattering model was used to gain an understanding of how the structural symmetry controls the in-phase scattering. The FDTD method was used to model and analyze the results. The influence of the ellipsoidal shape on the Fano profile was discussed by means of comparison with its cylindrical counterpart with respect to the spectral interference of superradiant bright and subradiant dark modes. The ESN cavity, which exhibits ultrahigh transmission at 1600 nm because of HHG, can be used for applications in lasing and plasmon-induced transparency. The influence of input power and its application in switching was demonstrated with the maximum efficiency displayed in the visible region. The dependence of Fano line shapes on the light polarization was also assessed. The Fano response of the proposed system revealed that different wavelength regimes are suitable for different applications, thereby highlighting the potential of the ESN cavity in a broad range of applications including lasing, switching, sensing, and design of surface plasmon polariton-based filters.

ACKNOWLEDGMENTS

We greatly acknowledge the initiative and support towards establishment of TIFAC—Center of Relevance and Excellence in Fiber Optics and Optical Communication at Delhi College of Engineering now Delhi Technological University, Delhi through Mission Reach Program of Technology Vision 2020, Government of India.

[1]U. Fano, Phys. Rev. **124**, 1866 (1961).
[2]B. Lukyanchuk, N. I. Zheludev, S. A. Maier, N. J. Halas, P. Norlander, H. Geissen, and C. T. Chong, Nature Mater. **9**, 707 (2010).
[3]A. E. Miroshnichekno, S. Flach, and Y. S. Kivshar, Rev. Mod. Phys. **82**, 2257 (2010).
[4]M. Sarrazin, J. P. Vigneron, and J. M. Vigoureux, Phys. Rev. B **67**, 085415 (2003).
[5]A. C. Johnson, C. M. Marcus, M. P. Hanson, and A. C. Gossard, Phys. Rev. Lett. **93**, 106803 (2004).
[6]K. Kobayashi, H. Aikawa, A. Sano, S. Katsumoto, and Y. Iye, Phys. Rev. B **70**, 035319 (2004).
[7]S. Fan and J. Joannopoulos, Phys. Rev. B **65**, 235112 (2002).
[8]A. Christ, S. Tikhodeev, N. Gippius, J. Kuhl, and H. Giessen, Phys. Rev. Lett. **91**, 183901 (2003).
[9]H. Lee and A. W. Poon, Opt. Lett. **29**, 5 (2004).
[10]A. Christ, O. J. F. Martin, Y. Ekinci, N. A. Gippius, and S. G. Tikhodeev, Nano Lett. **8**, 2171 (2008).
[11]J. A. Fan, C. Wu, K. Bao, J. Bao, R. Bardhan, N. J. Halas, V. N. Manoharan, P. Norlander, G. Shvets, and F. Capasso, Science **328**, 1135 (2010).
[12]N. Verellen, Y. Sonnefraud, H. Sobhani, F. Hao, V. V. Moshchalkov, P. Van. Dorpe, P. Norlander, and S. A. Maier, Nano Lett. **9**, 1663 (2009).
[13]F. Hao, Y. Sonnefraud, P. Van. Dorpe, S. A. Maier, N. J. Halas, and P. Norlander, Nano Lett. **8**, 3983(2008).
[14]B. Gallinet and O. J. F. Martin, ACS Nano **5**, 8999–9008 (2011).
[15]C. F. Bohren and D. R. Huffman, "Absorption and Scattering of Light by Small Particles" (Wiley-Interscience Publications, 1983).
[16]J. A. Fan, K. Bao, C. Wu, J. Bao, R. Bardhan, N. J Halas, V. N. Manoharan, G. Shvets, P. Norlander, and F. Capasso, Nano Lett. **10**, 4680 (2010).
[17]D. Wu, S. Jiang, and X. Liu, J. Phys. Chem. C **116**, 13745–13748 (2012).
[18]B. Gallinet and O. J. F. Martin, Phys. Rev. B **83**, 235427 (2011).
[19]A. W. Powell, M. B. Wincott, A. A. R. Watt, H. E. Assender, and J. M. Smith, J. Appl. Phys. **113**, 184311 (2013).
[20]S. Baldelli, A. S. Eppler, E. Anderson, Y. Shen, and G. A. Somorjai, J. Chem. Phys. **113**, 5432–5438 (2000).
[21]O. Levi, T. J. Pinguet, T. Skauli, L. A. Eyres, K. R. Parameswaran, J. S. Harris, M. M. Fejer, T. J. Kulp, S. E. Bisson, B. Gerard, E. Lallier, and L. Becouarn, Opt. Lett. **27**, 2091 (2002).
[22]S. Kim, J. Jin, Y. Kim, I. Park, Y. Kim, and S. Kim, Nature **453**, 757 (2008).
[23]A. Husakou and J. Herrmann, Phys. Rev. A **83**, 043839 (2011).
[24]M. Kroner, A. O. Govorov, S. Remi, B. Biedermann, S. Seidl, A. Badolato, P. M. Petroff, W. Zhang, R. Barbour, B. D. Gerardot, R. J. Warburton, and K. Karrai, Nature **451**, 311 (2008).

पेटेंट कार्यालय
शासकीय जर्नल

OFFICIAL JOURNAL
OF
THE PATENT OFFICE

निर्गमन सं. 25/2014	शुक्रवार	दिनांक: 20/06/2014
ISSUE NO. 25/2014	FRIDAY	DATE: 20/06/2014

पेटेंट कार्यालय का एक प्रकाशन
PUBLICATION OF THE PATENT OFFICE

INTRODUCTION

In view of the recent amendment made in the Patents Act, 1970 by the Patents (Amendment) Act, 2005 effective from 01st January 2005, the Official Journal of The Patent Office is required to be published under the Statute. This Journal is being published on weekly basis on every Friday covering the various proceedings on Patents as required according to the provision of Section 145 of the Patents Act 1970. All the enquiries on this Official Journal and other information as required by the public should be addressed to the Controller General of Patents, Designs & Trade Marks. Suggestions and comments are requested from all quarters so that the content can be enriched.

(**Chaitanya Prasad**)
CONTROLLER GENERAL OF PATENTS, DESIGNS & TRADE MARKS

20th JUNE, 2014

(12) PATENT APPLICATION PUBLICATION
(19) INDIA
(22) Date of filing of Application :22/04/2013

(21) Application No.1168/DEL/2013 A
(43) Publication Date : 20/06/2014

(54) Title of the invention : SYSTEM AND METHOD FOR DETECTING, INDENTIFYING AND CLSSIFYING CANCER CELLS

(51) International classification :G01B9/021
(31) Priority Document No :NA
(32) Priority Date :NA
(33) Name of priority country :NA
(86) International Application No :NA
Filing Date :NA
(87) International Publication No : NA
(61) Patent of Addition to Application Number :NA
Filing Date :NA
(62) Divisional to Application Number :NA
Filing Date :NA

(71)**Name of Applicant :**
1)DILLU, VENUS
Address of Applicant :SBTF-4, SCIENCE BLOCK, THIRD FLOOR, APPLIED PHYSICS DEPARTMENT DELHI TECHNOLOGICAL UNIVERSITY (FORMERLY: DELHI COLLEGE OF ENGINEERING) BNAWANA ROAD, DELHI-110042 India
2)SINHA, RAVINDRA KUMAR
(72)**Name of Inventor :**
1)DILLU, VENUS
2)SINHA, RAVINDRA KUMAR

(57) Abstract :
The present disclosure provides a sensing system, a sensing device and a method thereof. A waveguide based configuration comprising an array of metal rods arranged periodically in a lattice is provided. The array of metal rods is embedded in a substrate forming a fortified core in a predefined manner. The array of metal rods comprises one sensing arm to place biological material to be detected. The array of metal rods when exposed to the optical device produces plasmons due to interaction between nano particles associated with the array of metal rods and light received from the optical device and thus causes changes in wave parameters. The changes are sensed in order to sense the biological material. The wave parameters so sensed are used to classify the biological material in order to obtain a classified biological material, wherein the wave parameters are compared to predetermined wave parameters to classify the biological material.

No. of Pages : 34 No. of Claims : 10